Leibniz-Institut für Astrophysik Potsdam

Spot evolution on the red giant star XX Triangulum

Dissertation
zur Erlangung des akademischen Grades
“doctor rerum naturalium”
(Dr. rer. nat.)
in der Wissenschaftsdisziplin Astrophysik

eingereicht an der
Mathematisch-Naturwissenschaftlichen Fakultät
der Universität Potsdam

von
Andreas Künstler

Potsdam, den 23. Juni 2015

Published online at the
Institutional Repository of the University of Potsdam:
URN urn:nbn:de:kobv:517-opus4-84008
http://nbn-resolving.de/urn:nbn:de:kobv:517-opus4-84008

Zusammenfassung

Sternflecken gelten als stellare Analoga zu Sonnenflecken. Somit sind Sternflecken direkte Erscheinungsformen starker Magnetfelder. Ihre Zerfallsrate ist direkt mit der magnetischen Diffusivität verknüpft, welche selbst ein Maß für die Länge eines Aktivitätszyklus ist. Bislang konnte noch kein Zerfall eines einzelnen Sternflecks beobachtet werden und somit konnte noch kein stellarer Aktivitätszyklus mittels einer aus dem Fleckenzerfall abgeleiteten Diffusivität bestimmt werden.

Wir untersuchen die Entwicklung von Sternflecken auf dem schnell rotierenden K0 Riesenstern XX Triangulum. Über einen Zeitraum von sechs Jahren wurden durchgängig hochauflösende Spektren mit dem 1.2-m STELLA Teleskop auf Teneriffa aufgenommen. Mit unserem Inversionscode für Linienprofile (*iMap*) werden insgesamt 36 Dopplerkarten der Sternoberfläche rekonstruiert. Um sowohl den Zerfall als auch die Entstehung von Sternflecken zu bestimmen, werden die rekonstruierten Dopplerkarten mit vereinfachten Fleckenmodellen mittels einer Monte-Carlo-Methode abgebildet.

Es zeigt sich, dass die Oberfläche von XX Tri mit großen Flecken auf hohen und sogar polaren Breiten bedeckt ist sowie gelegentlichen kleineren Flecken nahe des Äquators. Gerade in der Zeitspanne von sechs Jahren sehen wir eine systematische Veränderung der Fleckenverteilung auf unterschiedlichen Zeitskalen und mit unterschiedlicher Morphologie, wie Fleckenaufspaltung und Fleckenvereinigung sowie Fleckenzerfall und Fleckenentstehung.

Zum ersten Mal wird die Zerfallsrate eines Sternflecks auf einem anderen Stern als der Sonne bestimmt. Von unserer Fleckenzerfallsanalyse bestimmen wir eine mittlere lineare Zerfallsrate von $D = -0.067 \pm 0.006$ Gm^2/d. Von dieser Zerfallsrate leiten wir eine turbulente Diffusivität von $\eta_T = (6.3 \pm 0.5) \times 10^{14}$ cm^2/s ab, und schließen daraus einen Aktivitätszyklus von 26 ± 6 Jahren. Diese Zykluslänge stimmt gut mit photometrischen Beobachtungen überein.

Unsere Dopplerkarten ermöglichen zusätzlich die Untersuchung der differentiellen Rotation auf XX Tri, wofür eine Kreuzkorrelationsmethode angewandt wird. Wir detektieren eine schwache sonnenähnliche differentielle Rotation mit einer Oberflächenscherung von $\alpha = 0.016 \pm 0.003$. Dieser Wert stimmt mit vergleichbaren Untersuchungen anderer RS CVn-Sterne überein.

Zudem haben wir Anzeichen für aktive Longituden und Flip-Flops gefunden. Während sich die aktivere Longitude in Phase zu dem (nicht sichtbaren) Begleitstern befindet, liegt die schwächere aktive Longitude auf der gegenüberliegenden Hemisphäre. Aus ihrem periodischen Auftreten schließen wir auf einen Flip-Flop-Zyklus von ungefähr zwei Jahren. Beide Aktivitätserscheinungen sind häufig auf Doppelsternen späten Spektraltyps zu finden.

Zu guter Letzt bestimmen wir die astrophysikalischen Eigenschaften von XX Tri neu, da seit der letzten Bestimmung im Jahre 1999 große neue Datensätze unterschiedlicher Beobachtungen vorhanden sind. Zusätzlich vergleichen wir die periodische Fleckenmodulation aus photometrischen und spektroskopischen Analysen.

Abstract

Spots on stellar surfaces are thought to be stellar analogues of sunspots. Thus, starspots are direct manifestations of strong magnetic fields. Their decay rate is directly related to the magnetic diffusivity, which itself is a key quantity for the deduction of an activity cycle length. So far, no single starspot decay has been observed, and thus no stellar activity cycle was inferred from its corresponding turbulent diffusivity.

We investigate the evolution of starspots on the rapidly-rotating K0 giant XX Trianagulum. Continuous high-resolution and phase-resolved spectroscopy was obtained with the robotic 1.2-m STELLA telescope on Tenerife over a timespan of six years. With our line-profile inversion code *iMap* we reconstruct a total of 36 consecutive Doppler maps. To quantify starspot area decay and growth, we match the observed images with simplified spot models based on a Monte-Carlo approach.

It is shown that the surface of XX Tri is covered with large high-latitude and even polar spots and with occasional small equatorial spots. Just over the course of six years, we see a systematically changing spot distribution with various time scales and morphology such as spot fragmentation and spot merging as well as spot decay and formation.

For the first time, a starspot decay rate on another star than the Sun is determined. From our spot-decay analysis we determine an average linear decay rate of $D = -0.067 \pm 0.006$ Gm^2/day. From this decay rate, we infer a turbulent diffusivity of $\eta_T = (6.3 \pm 0.5) \times 10^{14}$ cm^2/s and consequently predict an activity cycle of $\approx 26 \pm 6$ years. The obtained cycle length matches very well with photometric observations.

Our time-series of Doppler maps further enables to investigate the differential rotation of XX Tri. We therefore applied a cross-correlation analysis. We detect a weak solar-like differential rotation with a surface shear of $\alpha = 0.016 \pm 0.003$. This value agrees with similar studies of other RS CVn stars.

Furthermore, we found evidence for active longitudes and flip-flops. Whereas the more active longitude is located in phase towards the (unseen) companion star, the weaker active longitude is located at the opposite stellar hemisphere. From their periodic appearance, we infer a flip-flop cycle of ≈ 2 years. Both activity phenomena are common on late-type binary stars.

Last but not least we redetermine several astrophysical properties of XX Tri and its binary system, as large datasets of photometric and spectroscopic observations are available since its last determination in 1999. Additionally, we compare the rotational spot-modulation from photometric and spectroscopic studies.

Contents

List of Figures

List of Tables

1 Introduction

Since the discovery of strong magnetic fields on the Sun, magnetic fields play a key role in the understanding of *solar* and *stellar activity*. They influence the formation and evolution of stars and stellar remnants as well as interstellar media. Solar and stellar spots are one of the most prominent manifestations of strong magnetic fields on stars. Other activity phenomena of magnetic origin are flares, prominences and coronal mass ejections (CMEs).

Christoph Scheiner (1575-1650) and Galileo Galilei (1564-1642) carried out first detailed sunspot observations in 1611. They observed the movements of sunspots across the solar disk and studied their evolution. Figure 1.1 shows a drawing from Christoph Scheiner's first work "Tres epistolae de maculis solaribus" on sunspots. Up to now the solar surface was continuously observed over four centuries, enabling the discovery of maxima and minima in the solar activity, such as the 11-years sunspot cycle (Schwabe 1844), as well as the 70 years lasting Maunder-Minimum.

At the beginning of the 20th century, George Ellery Hale (1868-1938) found the presence of strong magnetic fields within sunspots and with that the first extra-terrestrial magnetic field (Hale 1908). His discovery marked the beginning of the study of solar magnetic activity. Since then, scientists observed temperature and magnetic field distributions on the surface of the Sun. Additionally, stars beyond the Sun came into view to study the influence of magnetic fields on star formation and evolution in general. Unfortunately, with a few exceptions nowadays (e.g. Gilliland & Dupree 1996; Kloppenborg et al. 2010), direct observations resolving a stellar surface are not possible on other stars than the Sun. Therefore, an indirect method was required.

The idea for mapping stellar surface structures was already formulated in 1958 by Armin Deutsch (1958), using rotationally broadened spectral line profiles of fast rotating active stars. This basic concept for what is known today as *Doppler imaging* (DI) was at first realized by Khokhlova & Riabchikova (1975) and Goncharskii et al. (1977) for mapping element abundances. Vogt & Penrod (1983) used the method for temperature mapping and introduced the name Doppler imaging.

As an extension of DI Semel (1989) established the Zeeman-Doppler imaging (ZDI) technique for inferring stellar magnetic fields. ZDI based on the analysis of spectral line polarization due to the Zeeman effect and allows for disentangling magnetic field distribution on the stellar surface. This method was further developed by, e.g., Brown et al. (1991), Piskunov & Rice (1993), and Donati et al. (1997).

From the theoretical point of view, various dynamo models were developed (e.g., Parker 1955; Babcock 1961) to understand the generation of stellar magnetic fields and explain the observed activity phenomena in general.

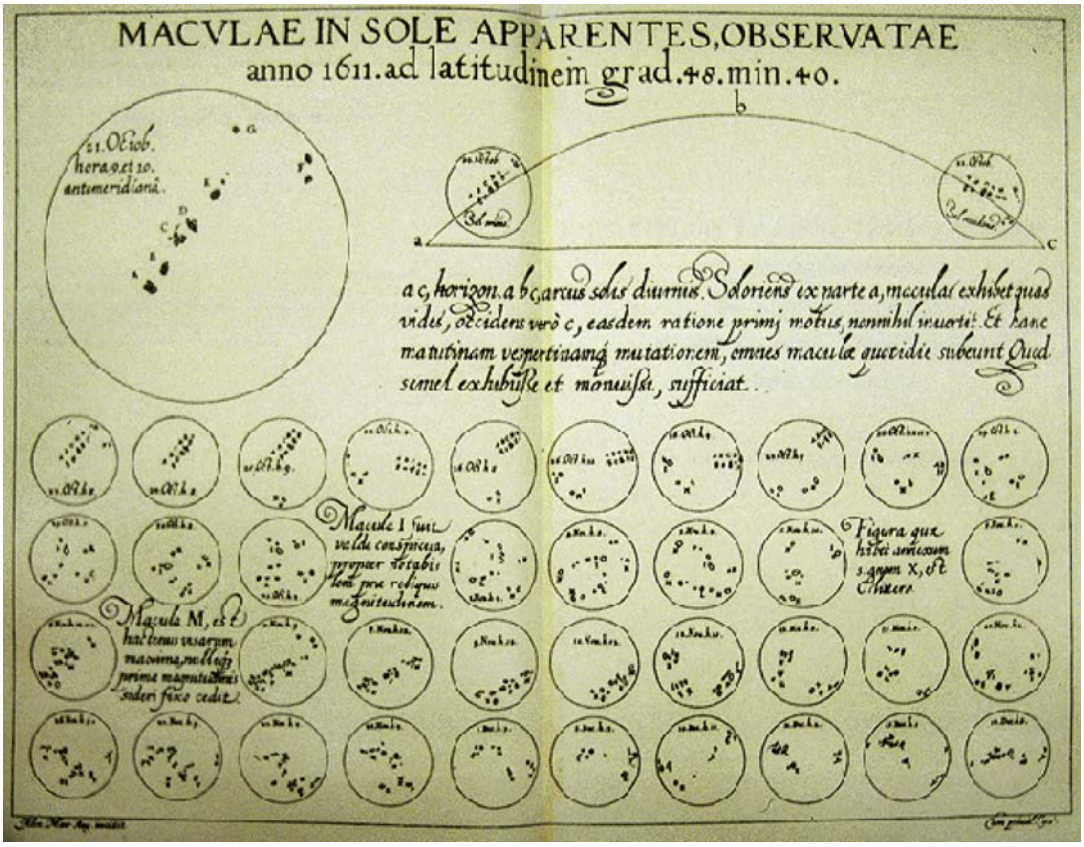

Figure 1.1: Sunspot drawings from Christoph Scheiner's (1575-1650) first work "Tres epistolae de maculis solaribus", published 1612. (Taken from http://galileo.rice.edu/sci/observations/sunspots.html.)

1.1 Solar and stellar activity

Various activity phenomena seen on the Sun are associated with magnetic fields and summarized as solar activity. Similar phenomena present on other stars are denoted as stellar activity. The interaction between solar and stellar studies is generally referred to as the *solar-stellar connection* (Dupree 2003; Strassmeier 2004).

Activity phenomena on the Sun are well studied, because of its angular diameter of 32'. Thus, we can observe solar surface structures and their dynamics in great detail. Spots play a key role in the study of solar and stellar activity. Beside being a direct manifestation of strong magnetic fields, their periodic appearance is directly linked to *activity cycles*. Therefore, their study may provide indirect information about the internal dynamo process, reminding us that this is still very controversial (e.g. Käpylä et al. 2011, 2012; Jabbari et al. 2015; Yadav et al. 2015).

Sunspots enable us to trace *differential rotation* and meridional circulation on the solar surface (Brajša et al. 2002; Wöhl 2002). Most stars investigated so far show solar-like differential rotation, i.e. the equator rotates faster than the pole. During the last decade several stars with anti-solar differential rotation were detected (Kővári et al. 2015). In close binaries, such as the RS CVn-systems, tidal effects are thought to play an important role, as they help in maintaining the fast rotation and magnetic activity on high levels (cf. Scharlemann 1981, 1982; Schrijver & Zwaan 1991; Holzwarth & Schüssler 2002).

Another characteristic of surface activity are so-called *active longitudes*, where magnetic activity concentrates and shows up over longer timescales, up to the length of a stellar cycle. Such a phenomenon was found at first on the rapidly rotating single late-type giant FK Comae by Jetsu et al. (1991). Berdyugina & Tuominen (1998) found a similar behavior on RS CVns, where mostly two dominant active regions were present and located at opposite hemispheres with a longitudinal shift of around 180°. A semi-periodic switching from one active longitude to the other is called a *flip-flop* phenomenon (Berdyugina 2005). There is some evidence for long-term active longitudes and a 7-year flip-flop period on the Sun (Berdyugina & Usoskin 2003).

Solar and stellar activity phenomena can be detected with various methods and telescopes, which concentrate on single line profiles or broad-bands of the electromagnetic (EM) spectrum. The most prominent activity phenomenon, spots, are mostly observed within the optical wavelength range in both photometry and spectroscopy.

Solar flares affect all layers of the solar atmosphere (photosphere, chromosphere, and corona), when the plasma medium is heated to millions of Kelvin, while the charged particles are accelerated to near the speed of light. They produce radiation across the EM spectrum at all wavelengths, from radio waves to gamma rays. Stellar flares are mostly detected in Balmer lines (e.g., Guenther & Ball 1999) and X-rays (e.g., Schmitt 1994), but also in radio emission (e.g., Bastian 1996).

Chromospheric activity is visible in Hα emission and Ca II H&K emission lines. Around 100 years ago, Eberhard & Schwarzschild (1913) discovered bright emission lines in the cores of the strong Ca II absorption features of α Boo, α Tau, and σ Gem. Since then several authors investigated the chromospheric behavior of single and/or binary stars, main-sequence and/or (sub-)giant stars (e.g., Strassmeier et al. 1990; Baliunas et al. 1995; Xuefu et al. 1996). Coronal activity is observable in X-ray and EUV (e.g., Drake et al. 2000), as well as in microwave emissions (e.g., Güdel 1996).

1.2 Origin and evolution of sunspots and starspots

Sunspots are thought to be tracers of a tube-like magnetic field structure, which arises from the bottom of the convection zone and permeates the photosphere. Their fields are strong enough to suppress the overturning convective motion and thus block or redirect the convective energy transport. As a consequence, these regions have a lower temperature than their surroundings and therefore appear as dark spots (Biermann 1938, 1948).

First assumptions about the existence of spots on other stars, so-called starspots, were made by Kron (1950), who observed eclipsing binaries and detected significant light variability outside eclipse that could not be explained. Finally, Hall (1972) explicitly postulated the starspot model to explain these periodic wave-like features in the light-curves of active stars.

As a generalized rule for stars, it can be stated that the occurrence of spots requires the existence of a convection zone and that the formation of stellar spots is similar to that of solar spots. However, considering their size and lifetime, as well as their occurrence on the stellar disk, stellar spots can differ widely from their solar analogues.

Sunspots

The magnetic field strength inside a sunspot can have a value of up to 3000 G and a temperature of around 4000 K, which is almost 2000 K lower than the temperature of the photosphere. A typical sunspot has an area of less than 0.2 % of the Solar Hemisphere (SH). Sunspots often appear as bipolar groups, where two involved spots harbor fields of opposite polarity, as seen in Figure 1.2. The Coriolis force causes rising toroidal flux tubes to twist in a clockwise direction in the northern hemisphere and in a counter-clockwise direction in the southern hemisphere. As a result, bipolar groups with a leader and a follower spot of opposite polarity have opposite signs between each hemisphere.

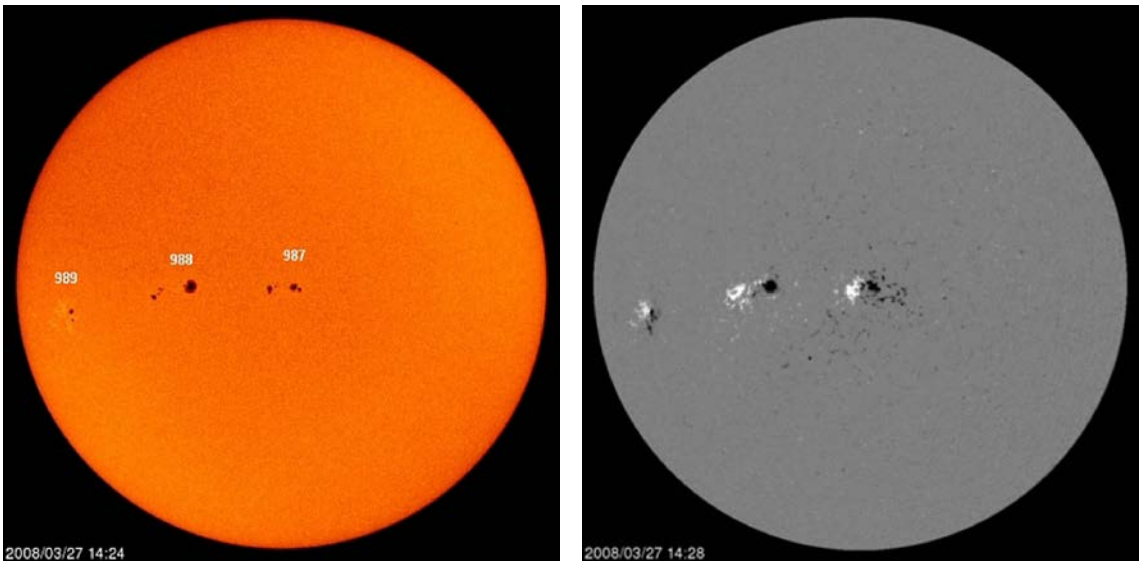

Figure 1.2: Sunspot pairs seen with a visible filter (*left*) and with a polarization filter (*right*). Spots are much cooler and therefore darker than their surroundings. The individual spots of a spot pair have typically opposite polarity. (Taken from http://sohowww.nascom.nasa.gov/sunspots/.)

The number and total area of sunspots varies largely in time as illustrated in Figure 1.3. During sunspot minima, mostly no spots are seen on the surface, whereas during sunspot maxima, up to 0.5 % of the solar hemisphere is covered with several spots. The upper panel of Fig. 1.3 is known as the famous *Butterfly-Diagram*. It shows the latitudinal occurrence of spots over time as well as the relative spottedness. The 11-year solar sunspot cycle is evident, whereas at the beginning of each cycle, spots appear first at high latitudes around 40°. As the cycle progresses, spots migrate towards lower latitudes. At the end of a cycle spots appear very close to the equator at latitudes around 10°.

Beside these relatively short-term variations there are also long-term variations. Between 1645 and 1715 a pronounced activity minimum happened (known as Maunder-Minimum), during which no or almost no spots were present on the solar surface. While the 11-year cycle could qualitatively be reproduced by magneto-hydrodynamic (MHD) simulations, the long-term variations are still not well enough understood to be modeled (Charbonneau 2010).

The lifetimes of sunspots vary from several days up to several months and strongly depend on the fact, whether the spot is a leader (in the sense of solar rotation) or

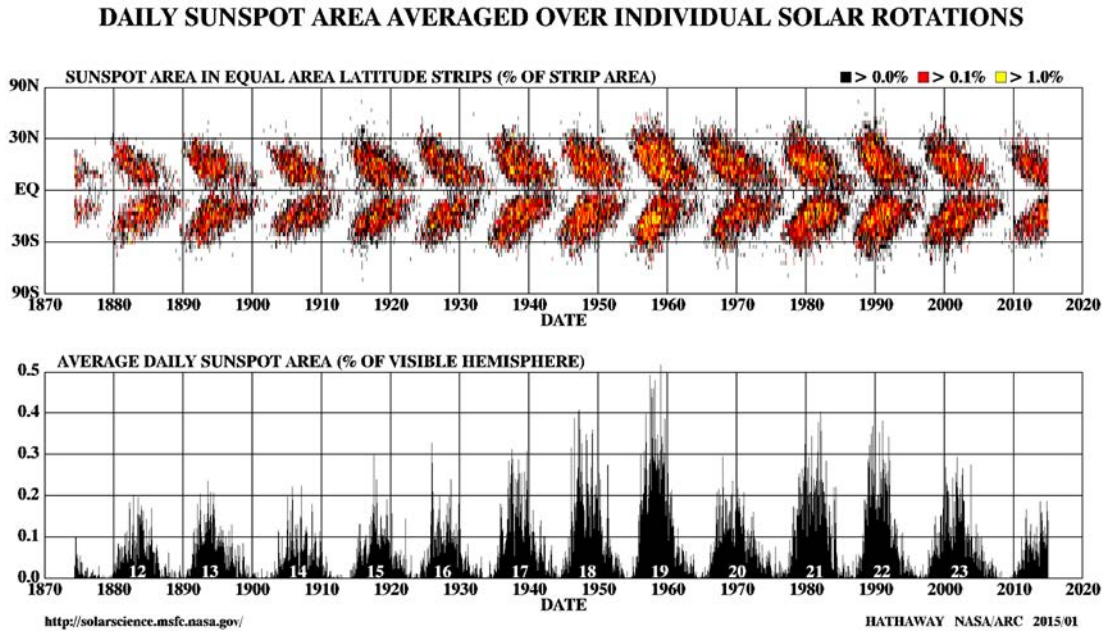

Figure 1.3: Butterfly-Diagram showing the latitudinal occurrence of spots over time together with the color-coded relative spot size (*upper* plot) and the daily average sunspot area over time (*lower* plot). Both plots show nicely the 11-year solar cycle. (Taken from http://solarscience.msfc.nasa.gov/SunspotCycle.shtml.)

a follower of a bipolar spot pair. Whereas follower spots decay within days, leader spots can live for up to four months (Bumba 1963). This difference between the two poles of the active region is not yet understood (Martínez Pillet 2002). Even the decay of sunspots, and thus the decay of the surface magnetic flux, is still not fully understood (Rüdiger & Kitchatinov 2000). Bumba (1963) proposed for a subset of recurrent sunspots from the Greenwich Photoheliographic Results (GPR) a linear area decay law of the type

$$dA/dt = D \ , \ A(t) = A_0 + D(t - t_0) \ , \tag{1.1}$$

with a mean value for D of -4.2 MSH/day[1]. Martinez Pillet et al. (1993) included in their study the whole GPR data to analyze the decay rates for recurrent spot groups and found a mean value of -12.1 MSH/day. They also pointed out that the quantity D has a log-normal distribution. Petrovay & van Driel-Gesztelyi (1997), using the more accurate Debrecen data, supported a parabolic decay law implying $dA/dt \propto \sqrt{A(t)}$. More recently, Martínez Pillet (2002) found area decay rates of -5.26 and -3.87 MSH/day for two leader spots observed in June 1992 with magnetic flux loss rates, $d\Phi/dt$, of -1.44×10^{20} and -0.6×10^{20} Mx/day, respectively. The importance of the magnetic flux loss rate $d\Phi/dt$ is that it determines the *magnetic diffusivity*, which itself is a driving parameter for cycle strength prediction. A linear area decay law has been studied from a theoretical point of view (Gokhale & Zwaan 1972; Meyer et al. 1974; Krause & Rüdiger 1975). Meyer et al. (1974) considered a process of diffusion of magnetic field across the entire area of the spot. This diffusion

[1]MSH = Millionth Solar Hemisphere, 1 MSH = 3.05 Mm^2

model predicts a constant area (and magnetic flux) decay, implying that dA/dt is proportional to the turbulent diffusivity η_T. Krause & Rüdiger (1975) proposed a similar model based on turbulence, where the turbulent diffusion was related to the flux decay by $d\Phi/dt \propto \eta_T$. Rüdiger & Kitchatinov (2000) used a mean-field formulation of the diffusivity quenching and produced quasi-linear decay curves for both the spot area as well as the magnetic flux. As the decay rate of spots is directly linked to the activity cycle, its understanding is of great interest.

Starspots

So far, around 500 spotted stars were analyzed with various methods, mostly using broad-band photometry (Strassmeier 2009). Only $\approx 15\,\%$ of them were Doppler imaged, of which approximately half are close binaries and half are single stars. Whereas most of these binaries are late-type giants, the mapped single stars cover nearly all stellar evolutionary stages.

From all these Doppler maps, we know that the spot sizes differ largely from star to star, and range between 0.1-11 % of the total stellar surface (Strassmeier 2009). The record holders are, our target star, the K0III component in the RS CVn binary XX Tri (Strassmeier 1999), and the ultra rapidly-rotating K3 dwarf BO Mic with spots of size as small as 0.15 % (Barnes 2005; Wolter et al. 2005). We note, that such small spots are only resolvable if the number of resolution elements across the stellar disk is sufficiently large, i.e. small spots are only detectable on very rapidly rotating stars. As starspots can be up to 10,000 times larger than the largest sunspot group ever observed, it is believed that large spots appearing in Doppler images are indeed clusters of spots.

Originally, a somewhat controversial feature, though found on many stars, were large polar spots (Strassmeier 1996). There have been simulations reproducing high latitude spots (Granzer et al. 2000; Schrijver & Title 2001; Schüssler 2002), but the mechanism, responsible for polar spots, is still not clearly understood. Recently, Yadav et al. (2015) demonstrate for the first time that a self-consistent distributed dynamo can generate high latitude spots. Their result supports the idea that the dynamos in the interiors of rapidly rotating stars might be fundamentally different from the solar one.

One observational problem is the correlation between spot temperature and spot size and the ambiguity to separate these two quantities during the modeling approach. This problem is most evident for photometric spot modeling and thus, any results are fully model dependent. In order to minimize this dependency, the common practice is to use at least two well-defined photometric bandpasses, where one bandpass is optimized for the unspotted photosphere and the other one for the spotted photosphere, e.g., Johnson V and I, respectively. The spot temperature is much better constrained in Doppler imaging, if the code does a full radiative-transfer analysis of the local line profile for the full range of surface temperatures, chemical abundances, and limb angles. However, comparing temperature maps from DI, it appears that the cooler the star the smaller is the temperature difference between the spot and the unspotted photosphere. Berdyugina (2005) lists an average of 200 K temperature difference for M-dwarfs and up to 2000 K for F-stars.

The most important time scales associated with starspots are their lifetimes and decay times. So far, no single starspot (or starspot group) has been observed and

followed from its formation to its death. Thus, starspot lifetimes are method-dependent estimates and range from less than a month to over a decade (Hussain 2002). Her main conclusions and caveats together with more up-to-date data are summarized in Strassmeier (2009) suggesting that: (i) starspots on tidally locked binary stars live longer (months) than spots on single main-sequence stars (weeks); (ii) polar spots may be formed differently and thus, their lifetime may be driven by another physical mechanism; (iii) spot lifetimes from time-series photometry suggest on average a year-long existence; (iv) flip-flops may terminate a spot's or a group of spots' imprint on a light-curve and thus mask the regular decay mechanism.

The determination of starspot decay rates would help us to improve and clarify our knowledge about spot lifetimes, their evolution, and its connection to stellar activity cycles. Applying photometric spot modeling, Fröhlich et al. (2009) determined a turbulent magnetic diffusivity η_T of 1.2×10^{13} cm^2/s from spot variations on CoRoT-2a. A more direct access to the decay of starspots, is given by time-series Doppler imaging, if the spatial and temporal surface resolution is good enough.

1.3 Solar and stellar dynamo models

Magnetic fields of stars are maintained by dynamo processes in which convection and differential rotation play key roles. The mean-field dynamo theories (Chapter 1.4) are able to explain the interaction of both phenomena. In general, three different types of dynamo models exist depending on the interplay between convection and differential rotation. The Sun is believed to be of one type, the so-called $\alpha\Omega$-dynamo. This dynamo model is able to explain the 11-year sunspot cycle and to reproduce other effects, such as the latitudinal drift seen in the Butterfly-Diagram (Fig. 1.3).

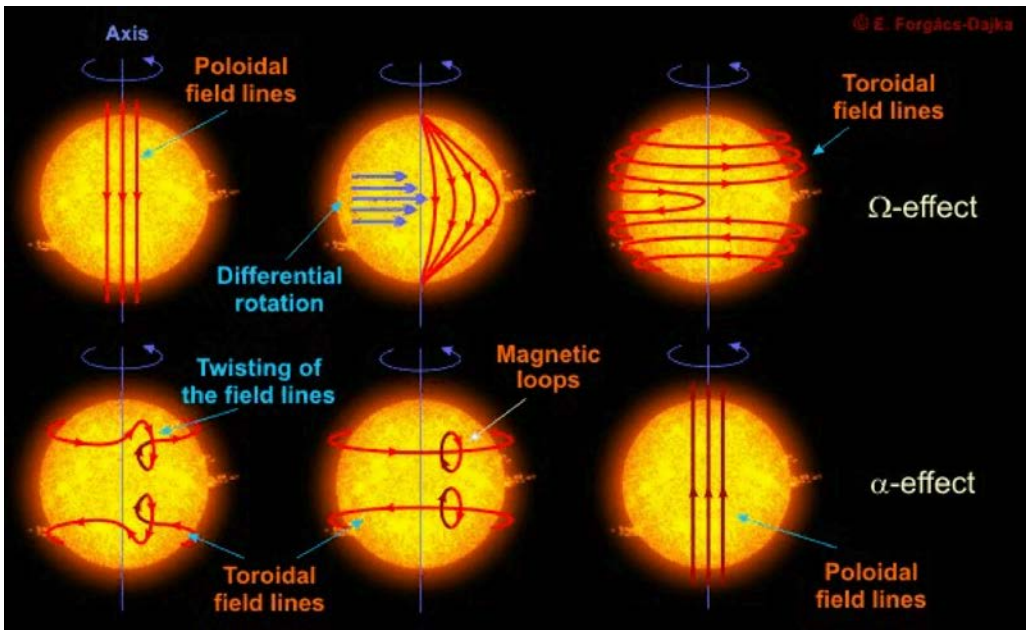

Figure 1.4: The $\alpha\Omega$-dynamo mechanism. The *upper* part illustrates the Ω-effect, due to differential rotation, whereas the *lower* part illustrates the α-effect, due to turbulence. (Taken from http://www.konkoly.hu/solstart/stellar_activity.html.)

The $\alpha\Omega$-dynamo consists of two effects, the α- and the Ω-effect as illustrated in Figure 1.4. The so-called Ω-effect describes the transformation of a poloidal magnetic field into a toroidal magnetic field due to differential rotation. The α-effect describes the regeneration of the poloidal field by the toroidal field due to turbulence. These two effects produce alternately poloidal and toroidal fields, thus maintaining a permanent field generation mechanism.

The $\alpha\Omega$-dynamo is the preferred model for the Sun and probably most other solar-like stars (Charbonneau 2010). However, there are two other mean-field dynamo models. In the α^2-dynamo, the α-effect alternately generates both poloidal and toroidal magnetic fields. Planetary dynamos are believed to be of this kind. In an $\alpha^2\Omega$-dynamo both, the α-effect and the Ω-effect, contribute to toroidal field generation. Some stellar dynamos could be of this kind, if differential rotation is weak, and/or if dynamo action takes place in a very thin layer (Charbonneau 2010).

1.4 Mean-field magnetohydrodynamic theory

All three different types of dynamo models can be described by a mean-field magnetohydrodynamic (MHD) approach, which presents one of the most powerful tools for exploring the nature of magnetic activity in stars (Moffatt 1978; Parker 1979; Krause & Rädler 1980). In the following we give a brief description of the mean-field dynamo theory, for further information see Charbonneau (2010) and Pipin (2013). The evolution of the magnetic field is govern by the induction equation:

$$\frac{\partial \boldsymbol{B}}{\partial t} = \nabla \times (\boldsymbol{U} \times \boldsymbol{B} - \eta \nabla \times \boldsymbol{B}) \ , \tag{1.2}$$

where $\boldsymbol{B}$ is the magnetic field, $\boldsymbol{U}$ is the velocity field and η is the molecular magnetic diffusivity.

In turbulent media, one can decompose the fields into mean and fluctuated parts, $\boldsymbol{B} = \overline{\boldsymbol{B}} + \boldsymbol{b}$, $\boldsymbol{U} = \overline{\boldsymbol{U}} + \boldsymbol{u}$, where $\overline{\boldsymbol{B}}$ and $\overline{\boldsymbol{U}}$ refer to the mean fields, and $\boldsymbol{b}$ and $\boldsymbol{u}$ to the fluctuating fields. The average of the fluctuating parts $\boldsymbol{b}$ and $\boldsymbol{u}$ vanishes, i.e., $\overline{\boldsymbol{b}} = 0$ and $\overline{\boldsymbol{u}} = 0$, whereas the cross product $\overline{\boldsymbol{u} \times \boldsymbol{b}}$ will not vanish upon averaging. To derive the mean-field dynamo equation, one has to assume, that in astrophysical systems like stars, the flows and magnetic fields are strongly turbulent, as well as the validation of the so-called Reynolds rules (Monin & I'Aglom 1971). Thus, by averaging the induction equation over the ensemble of the fluctuating fields one gets the mean-field dynamo equation:

$$\frac{\partial \overline{\boldsymbol{B}}}{\partial t} = \nabla \times (\overline{\boldsymbol{U}} \times \overline{\boldsymbol{B}} + \overline{\boldsymbol{u} \times \boldsymbol{b}} - \eta \nabla \times \overline{\boldsymbol{B}}) \ , \tag{1.3}$$

which is almost identical to Equation 1.2 except for the term $\overline{\boldsymbol{u} \times \boldsymbol{b}}$ corresponding to a mean electromotive force $\boldsymbol{\mathcal{E}}$ induced by the fluctuating field components. The first term $\nabla \times (\overline{\boldsymbol{U}} \times \overline{\boldsymbol{B}})$ can be interpreted as the advection of the mean magnetic field by mean flow.

Assuming the scale separation in turbulence (L, $T \gg l$, τ_c, where L, l are typical length scales and T, τ_c are typical time scales for the mean and the fluctuated parts of the fields) one can express $\boldsymbol{\mathcal{E}}$ in terms of the mean field $\overline{\boldsymbol{B}}$ (Rädler 1969; Krause & Rädler 1980; Brandenburg et al. 2012). This is usually carried out by expressing

$\boldsymbol{\mathcal{E}}$ as a truncated series expansion in $\overline{\boldsymbol{B}}$ and its derivatives. Retaining the first two terms yields:

$$\boldsymbol{\mathcal{E}} = \hat{\alpha} \circ \overline{\boldsymbol{B}} + \hat{\eta} \circ (\nabla \times \overline{\boldsymbol{B}}) \ , \tag{1.4}$$

where the coefficients $\hat{\alpha}$, $\hat{\eta}$ are tensors and the symbol $\circ$ marks the tensor product.

A simple case to calculate the components of the $\hat{\alpha}$ and $\hat{\eta}$ tensors is the assumption of a homogeneous, weakly anisotropic turbulence, which reduces both tensors to simple scalars, so that the mean electromotive force becomes:

$$\boldsymbol{\mathcal{E}} = \alpha \overline{\boldsymbol{B}} - \eta_T (\nabla \times \overline{\boldsymbol{B}}) \ . \tag{1.5}$$

Assuming the kinematic regime, α and η_T are independent of the magnetic field fluctuations, we obtain:

$$\alpha \approx -\frac{1}{3} \tau_c \langle \boldsymbol{u} \cdot \nabla \times \boldsymbol{u} \rangle \tag{1.6}$$

$$\eta_T \approx \frac{1}{3} \tau_c \langle |\boldsymbol{u^2}| \rangle \ , \tag{1.7}$$

where α describes the α-effect, while η_T is the scalar turbulent diffusivity and τ_c is the correlation time of the turbulent motions. As $\eta_T \gg \eta$ the last term of Equation 1.3 is negligible and we obtain:

$$\frac{\partial \overline{\boldsymbol{B}}}{\partial t} = \nabla \times (\overline{\boldsymbol{U}} \times \overline{\boldsymbol{B}} + \alpha \overline{\boldsymbol{B}} - \eta_T \nabla \times \overline{\boldsymbol{B}}) \ . \tag{1.8}$$

Using an axissymmetric solar model which takes only the differential rotation $\overline{\boldsymbol{U}} = \Omega(r, \theta)\, r \sin\theta \boldsymbol{e_\phi}$, a scalar α-effect α and a scalar turbulent diffusion η_T into account, one can decompose the magnetic field into poloidal and toroidal components ($\overline{\boldsymbol{B}} = \boldsymbol{B}_t\, \boldsymbol{e}_\phi + \nabla \times \boldsymbol{A}_p\, \boldsymbol{e}_\phi$). Consequently, the differential rotation converts $\boldsymbol{B}_p$ into $\boldsymbol{B}_t$, and the α-effect generates $\boldsymbol{B}_p$ from $\boldsymbol{B}_t$, and vice versa.

The enhanced decay and diffusive transport due to turbulent diffusion act on time scales of $\tau \equiv \frac{L^2}{\eta_T}$, where L is the length scale of the star. For the Sun, L is the width of the solar convection zone, $L \approx 0.3\ R_\odot \approx 200$ Mm. A widely accepted value for the diffusivity is $\approx 10^{12}$ cm^2/s, and so $\tau \approx 13$ years. This value is close to the observed solar activity cycle length of 11 years.

As already mentioned in Chapter 1.3, there exist two more dynamo concepts beside the $\alpha\Omega$-dynamo. One can define a dynamo number

$$D = D_\alpha D_\Omega \equiv \frac{\alpha_1 L}{\eta_T} \cdot \frac{\Delta\Omega L^2}{\eta_T} \ , \tag{1.9}$$

where $\Delta\Omega$ is the differential rotation rate, and the numbers D_α and D_Ω represent dynamo numbers. Dynamo action (exponential growth of $\overline{\boldsymbol{B}}$) occurs if $|D|$ exceeds a critical value. On the Sun, α is believed to be ≈ 0.1 ms^{-1}, and $\Delta\Omega \approx 2.5 \times 10^{-7}$ s^{-1}. Using these values, one finds $|D_\alpha| \ll |D_\Omega|$, justifying the $\alpha\Omega$-approximation, which ignores the α-effect in the generation of the toroidal mean magnetic field. However, if the two dynamo numbers are of the same order, the dynamo is of $\alpha^2\Omega$-type, and finally if $|D_\alpha| \gg |D_\Omega|$ the dynamo is of α^2-type.

1.5 Observations of stellar activity on late-type stars

Late-type stars denotes stars with an outer convection zone, where their spectral class ranges from about F7 to K2. They possess a dynamo that generates complex magnetic fields and thus show magnetic activity phenomena. Their temperature ranges from about 3500 to 7500 K and mass from about 0.8 to 1.7 $M_\odot$ (Kopf 2008). Therefore, our Sun of spectral type G2V, laying on the main sequence, is a rather ordinary late-type star among many others. We identify the following sub-types (Berdyugina 2005):

Solar-type stars

Solar-type stars are located on the lower main-sequence and show chromospheric activity similar to that on the Sun which is detected, e.g., in the Ca II H&K emission (Wilson 1978). Whereas the photometric variations due to spot modulation never exceed a few tenths of a percent on the Sun, the amplitude of the stellar variability can reach several percent on other solar-type stars. The link between the photometric variability of solar-type stars and the sunspot phenomenon is evident and provided by the fact that continuum variability seems to occur in anti-phase with variations in Hα and Ca II H&K emission variations (Dorren & Guinan 1982). This anti-correlation implies that, similar to active regions observed on the Sun, the surface activity of such stars is a localized phenomenon which include both emission plages and dark spots.

Whereas young stars exhibit high average levels of activity and rapid rotation, stars as old as the Sun and older have slower rotation rates and lower activity levels, i.e., the magnetic activity in solar-type stars declines with age which is closely related to a loss of angular momentum throughout the main-sequence lifetime (e.g., Skumanich 1972; Noyes et al. 1984; Baliunas et al. 1995).

T Tauri stars

T Tauri stars are pre-main sequence stars of about one solar mass at an age of a few million years. They were discovered and recognized as a new type of variables by Joy (1945). Strongly enhanced lithium absorption in their spectra indicates the young age of these stars. Typically, they are surrounded by an accretion disk, a relic from the star formation process, and show some strong emission lines. The surface activity of these stars comes along with a high magnetic activity (e.g., Gershberg 1982; Appenzeller & Dearborn 1984; Guenther & Ball 1999), accretion flows and stellar wind phenomena (e.g., Hartmann & Kenyon 1990; Hartmann 1990). The name that was given to that class of stars originates from the prototype star “T Tauri”.

RS CVn stars

RS CVn stars represent a class of close detached binaries with the more massive primary component being a G-K giant or subgiant and the secondary a subgiant or dwarf of spectral class G-M. Their strong photometric variability (outside eclipses) was interpreted as the rotationally modulated effect of cool spots on their surfaces (Eaton & Hall 1979). Many RS CVn systems appear as single-line binaries which

makes them attractive for spectral analysis and therefore a particularly interesting target for Doppler and Zeeman-Doppler imaging. In binaries, where both components can be observed, the primary appears more active than the secondary.

This class of variable stars, named after the prototype "RS Canum Venaticorum", was proposed by Hall (1976) who identified the following classification signatures: (i) photometric variability; (ii) Ca II H&K emission lines; (iii) subgiant component well within its Roche lobe; (iv) fast rotation, i.e. almost synchronized binaries with orbital periods of a few days; (v) orbital period variations. RS CVn-type variables are remarkable due to strong chromospheric plages, coronal X-ray, and microwave emissions, as well as strong flares in the optical, UV, radio, and X-ray.

Most of the present knowledge on starspots is based on studies of this type of stars. In the second edition of the "Catalog of chromospherically active binary stars", Strassmeier et al. (1993) listed 206 spotted stars and 124 candidates, most of them being RS CVns. XX Tri, the target star in this thesis belongs also to this class.

FK Com stars

In the early 1980's a new group of active stars were defined as FK Com stars, named after the prototype star "FK Comae" (Bopp & Rucinski 1981; Bopp & Stencel 1981). These stars are rapidly rotating single late-type giants of spectral class G-K with rotation periods of only a few days. Spectroscopic observations reveal a projected rotational velocity of 50-150 $\mathrm{km\,s^{-1}}$.

The magnetic activity of FK Com stars is revealed by rotationally modulated photometric variations caused by spots on the stellar surface. These stars show a very strong and variable chromospheric emission in the Ca II H&K lines and in the Balmer lines. The photometric and spectroscopic characteristics of FK Com stars are very similar to those of the very active RS CVn stars.

W UMa stars

W UMa stars are eclipsing binaries with short periods about several hours showing continuous light variations (Selam 2004). Both components are solar-type stars surrounded by a common envelope. With a projected rotational velocity of 100-200 $\mathrm{km\,s^{-1}}$, both components of such a contact binary rotate very rapidly in spite of their old ages. A study of the contact binaries with Doppler imaging reveals that both components can be covered by cool starspots, with a tendency for the primary to be more active than the secondary (Maceroni et al. 1994; Hendry & Mochnacki 2000; Barnes et al. 2004). This class of variable stars was named after the prototype "W Ursae Majoris".

1.6 Indirectly resolved disk observations and diagnostic tools

We present three commonly used methods allowing us to observe indirectly the surface on stars, in particular their temperature and/or magnetic field distribution (Kopf 2008). For further information see Berdyugina (2005).

Photometry and light-curve modeling

Photometry measures the total flux of a stellar object in a certain wavelength band. It was one of the first methods for the detection of starspots and its possibility was already discussed in 1950 by Kron (1950). Photometry allow the detection of stellar surface variations even for faint objects, as integral light is observed. Since about the 1970's spotted stars are observed regularly. In the early years, spot distributions from photometric observations were deduced from simple trial and error light-curve modeling. Later on, a two temperature light-curve inversion were applied in a more mathematical way. At present, ground-based automatic telescopes (APTs) provide nightly measurements of a large sample of stars reaching mmag precision (Strassmeier 2009). Thus, photometric data and light-curve inversion are often incorporated into Doppler imaging, putting further constraints on the inversion (e.g. Rice & Strassmeier 2000).

Spectroscopy and Doppler imaging

The Doppler imaging (DI) technique (e.g., Vogt & Penrod 1983; Rice et al. 1989; Strassmeier 1990; Piskunov & Rice 1993; Vogt et al. 1999; Rice & Strassmeier 2000) requires rotationally broadened absorption line profiles and purposes the reconstruction of a temperature or abundance surface distribution of a star. The use of intensity line profiles for the mapping of stellar surfaces was first formulated by Deutsch (1958) and first realized by Goncharskii et al. (1977) as an optimization process. Prerequisites are the rapid rotation of the considered star ($v \sin i \gtrsim 15$ km s^{-1}) and a high spectral resolution (R $\gtrsim$ 35,000). Thus, the rotational broadening dominates the natural line broadening and a meaningful Doppler imaging with reasonable stellar surface resolution is possible. Furthermore, a high signal-to-noise ratio (SNR) is important, so that distortions in the line profile caused by spots stand out from the noise. Instruments used for spectroscopy are, e.g., UVES at VLT and HIRES at KECK. Robotic telescopes, such as STELLA, have the ambition to do follow-ups and derive long-term activity variations and possibly obtain butterfly diagrams or flip-flop cycles. Further information about STELLA and its spectrograph are given in Chap. 2.3. The methods of Doppler imaging are explained in Chap. 3 in more details.

Spectropolarimetry and Zeeman-Doppler imaging

The most direct way to detect and study stellar magnetic fields is to use polarized light, which carries details about the magnetic field configuration at the point of origin due to the Zeeman effect. Zeeman-Doppler imaging (ZDI) was first proposed by Semel (1989) and is based on Doppler imaging and spectropolarimetry. In order to obtain polarization signals, so-called Stokes profiles, an elaborate polarization unit is connected ahead of the spectrograph. The disk integrated detection of small-scale stellar magnetic fields is a rather challenging task, due to mutual cancellation of local regions harboring mixed polarities. Thus, only large-scale magnetic fields can be reconstructed from disk-integrated polarimetric measurements.

1.7 Overview of the thesis

In this thesis, we present a so far unique time-series of Doppler images for the red giant star XX Triangulum. These temperature maps exhibit starspot distributions with different morphology, such as spot fragmentation and spot merging, covering 36 rotations over six years of observations. For the first time, we analyze starspot decay rates which allow us to determine a magnetic diffusivity and thus estimate a magnetic cycle timescale. Furthermore, we detect active longitudes and infer a flip-flop cycle. To investigate surface differential rotation, we apply a cross-correlation analysis. In addition, we redetermine astrophysical properties of XX Tri and its binary system. Last but not least, we compare our temperature imagery with photometric and spectroscopic measurements in terms of rotationally spot-modulation.

The thesis is structured as follows. Chapter 2 gives a scientific background of our target star XX Triangulum and redetermines its absolute astrophysical parameters. Furthermore, it describes the photometric observations with APT and the spectroscopic observations with STELLA. In addition, we analyze the photometric variability of XX Tri and compare them with spectroscopically obtained variations. Chapter 3 describes how Doppler imaging works in general and our inversion code *iMap* in particular. Within this chapter, we also present results for several tests with partially artificial, partially real data including inversion tests with phase gaps in single stellar rotations, and a phase-refilling scheme with data from the previous or the following stellar rotation. Furthermore, a method to analyze the spot distributions in a manageable way is presented. Last but not least, we present our time-series of Doppler images and their related spot-models. These images are analyzed in Chapter 4 and our results in terms of stellar activity phenomena are presented. Finally, the conclusions and discussion are presented in Chapter 5.

We note that several parts and results of this work are published in Künstler et al. (2015). Co-authors are T. A. Carroll [TAC] and K. G. Strassmeier [KGS]. [KGS] provided the spectroscopic and photometric data and gave many comments on the manuscript. [TAC] provided the Doppler imaging code *iMap* and supplied technical support with Doppler imaging.

2 XX Triangulum

Our target is the spotted red giant star XX Triangulum (HD 12545, HIP 9630) of spectral class K0III with an effective temperature of $\approx$ 4600 K. It is a member of the RS CVn class of magnetically active components of close binaries, in a synchronized SB1-type system with a period of $P_{\rm rot} \approx P_{\rm orb} \approx 24$ days. This star is famous for its detected superspot (Fig. 2.1) with a linear extension of 12×20 solar radii (Strassmeier 1999). By the use of the STELLA robotic telescopes (Strassmeier et al. 2010b), we have obtained almost 700 usable spectra between July 2006 and April 2012 which cover 36 rotational periods. Since 1993 photometric observations are taken with the APT (Strassmeier et al. 1997b).

In this chapter, we give an overview of scientific literature on XX Tri and redetermine its astrophysical properties. Furthermore, we present our photometric and spectroscopic observations. As rotational spot-modulation is detectable in photometric broad-band lightcurves as well as in spectroscopic line profile distortions, we analyze both datasets and compare their results.

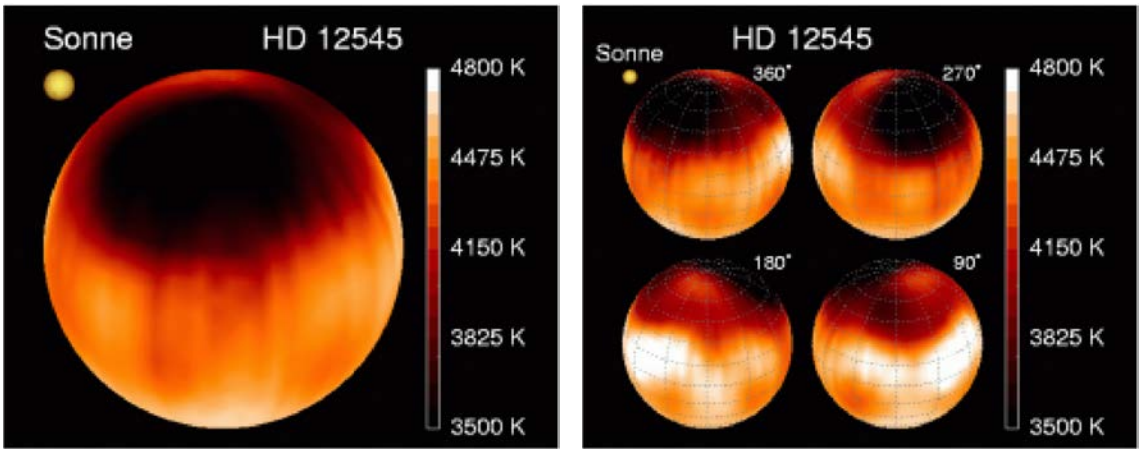

Figure 2.1: First Doppler image of XX Tri taken from Strassmeier (1999). A gigantic polar spot with a linear extension of 12×20 solar radii is seen. Furthermore, a smaller cool spot and a warm equatorial spot on the adjacent hemisphere were reconstructed.

2.1 Scientific background

In the mid-1980's XX Tri becomes one of the most attractive targets for photometrists due to its unusually large lightcurve variations. Bidelman (1985) observed strong Ca II H&K emission lines in the spectrum of XX Tri and suggested that it might also be a photometric variable. Photometric variability of RS CVn stars is generally attributed to the presence of large, cool starspots moving in and

Table 2.1: Astrophysical properties of XX Tri based on Strassmeier (1999).

Parameter	Value
Classification, MK	K0III
Distance, pc	197^{+54}_{-35}
$V_{\rm max}$, mag	7.875
Rotation period, d	24.0
Orbital period, d	23.96924 ± 0.00092
Inclination, deg	60 ± 10
$v \sin i$, km s^{-1}	20.8 ± 0.5
Temperature, K	4,750
Log gravity, cgs	2.5-3.0
Metallicity, $[{\rm Fe/H}]_\odot$	0.0 (solar, adopted)
Radius, $R_\odot$	$11.4^{+2.0}_{-0.8}$
Luminosity, $L_\odot$	35^{+22}_{-11}
Mass, $M_\odot$	$1.8^{+0.3}_{-0.2}$
Age, Gyr	1.8

out of view as the star rotates. The presence of an extremely active chromosphere on XX Tri was confirmed by Strassmeier et al. (1990) showing that the Ca II H&K emission intensity was 2-3 times that of the local continuum. Furthermore, a quite strong Hα emission was detected. Strassmeier et al. (1990) report the star to be of spectral class G5IV with an effective temperature of $\approx$ 4750 K in an SB1-type system with an orbital period of 23.9 ± 0.2 days. They also determined a projected rotational velocity of 17 ± 3 km s^{-1}.

The first published photometric observations were from 1986/87 and showed a fairly scattered lightcurve with a V amplitude of about $0\overset{\rm m}{.}16$ and a period of 25.1 ± 0.2 days (Hooten & Hall 1990). Assuming the photometric period to be equal the rotation period, which implies a minimum radius of 8.4 $R_\odot$, they suggest a giant classification. Three years later, a remarkable amplitude of $0\overset{\rm m}{.}6$ in V was observed by Nolthenius (1991). Multicolor photometry obtained in early 1991, showing a large amplitude of $0\overset{\rm m}{.}5$ in V, and $0\overset{\rm m}{.}12$ in $V-I$, allowed Strassmeier & Olah (1992) to derive a precise temperature difference between spot and photosphere of $\Delta T = 1100 \pm 35$ K, which suggests a spot coverage of approximately 20 % of the entire stellar surface. Furthermore, the $U-B$ and $B-V$ values suggest a K0III classification rather than the G5IV reported earlier.

Using spectroscopic data, Bopp et al. (1993) confirmed the K0III spectral type and determined an orbital period of $P_{\rm orb} = 23.97$ days and $v \sin i = 17 \pm 2$ km s^{-1}. The detection of Hα emission, strong emission features in UV and coronal X-rays, as well as He I absorption supports the RS CVn-type classification. Furthermore, a lithium abundance of $\log n({\rm Li}) \approx 1.7$ was detected, which is unusually high for a giant. Eker (1995) applied a multicolor lightcurve inversion on the same data used by Strassmeier & Olah (1992) and obtained similar results for the major modulating spot with a temperature difference of $\Delta T = 1280$ K, which covers ≈ 27 % of the total surface. Hampton et al. (1996) also reanalyzed these multicolor data and found $\Delta T = 650$-1200 K for inclinations of 70-30°.

Strassmeier et al. (1997a) presented new multicolor photometry obtained in the years 1991-1996 with three different automatic photoelectric telescopes (APTs): the 0.75-m Fairborn APT on Mount Hopkins in Arizona, U.S.A. equipped with $V(RI)_C$ filters matching the Johnson-Cousins system (Strassmeier et al. 1997b), the 0.25-m Phoenix APT also on Mount Hopkins but equipped with Johnson UBV, and the 0.8-m Catania APT on Mount Etna in Sicily, Italy with UBV filters for the Johnson system. They determined photometric periods for each observational season, varying between 23.87 and 25.32 days, and a long-term average of $<P_{phtm}> = 24.08$ d in the time range of 1985-1996. Furthermore, they suggest that the light-curve amplitude varies more or less systematically showing a small amplitude every 2.7 ± 0.2 years and a large amplitude shifted in time by about one half of that period.

A record lightcurve amplitude of $0\overset{\text{m}}{.}63$ in V and $0\overset{\text{m}}{.}17$ in $V-I$ in January 1998 was reported by Strassmeier (1999). At this state of high activity, spectroscopic observations were obtained at Kitt Peak National Observatory (KPNO) and allowed to obtain the first Doppler image of XX Tri (Strassmeier 1999), see Fig. 2.1. It shows a gigantic cool, high-latitude spot of elliptical shape with a temperature of around 3500 K. Beside this superspot, a smaller, cool spot with a temperature of around 4000 K and a warm equatorial spot on the adjacent hemisphere were reconstructed. Furthermore, the orbital elements of XX Tri were refined and its absolute astrophysical quantities were determined using the Hipparcos parallax (ESA 1997). The most important astrophysical properties of XX Tri are summarized in Table 2.1.

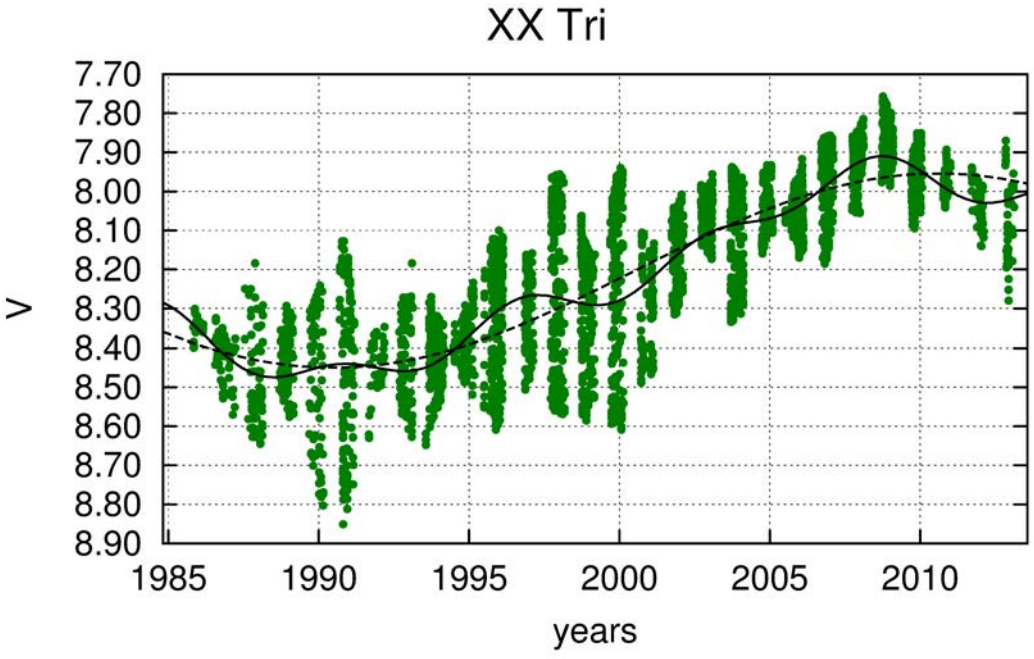

Figure 2.2: Cycle predictions for XX Tri based on photometry (Oláh et al. 2014). Shown are 28 years of V data and their fits with a long-term modulation (dashed line), and with co-added modulations of timescales of 6 and 12 years (solid line).

Due to their temperature sensitivity, TiO-bands are able to determine starspot properties. The relative strength of the bands constrains the starspot temperature (T_S), while their absolute strengths are functions of the total projected area of

starspots on the visible hemisphere (the filling factor f_S). O'Neal et al. (2004) observed XX Tri in December 2001 and found $f_S = 0.31 \pm 0.05$ and 0.35 ± 0.05 for the two nights of observation and $T_S = 3425 \pm 120$ K for both nights.

Since 1985 XX Tri has been observed photometrically with various telescopes, in which about 20 years of APT photometry is included. The large dataset in V is shown in Fig. 2.2, including long-term modulations. Oláh et al. (2014) found a trend in V of $1^{\mathrm{m}}.05$ from the deepest minimum to the overall maximum, with a length comparable to the length of the dataset (≈ 28 years), as well as an about 6 years long cycle and its double.

2.2 New photometric observations

Small automatic telescopes have been used over decades to obtain differential photometric observations of variable stars (see Strassmeier et al. 1997a, and references therein). Most of their time is devoted to monitoring rotationally modulated light variations due to cool starspots in a sample of selected late-type stars. A period analysis for each individual observing season gives a set of stellar rotation periods and their seasonal variations. Furthermore, the long-term lightcurve behavior is examined for stellar activity cycles.

Figure 2.3: APTs at Fairborn observatory. *Left:* Shown are the 0.75-m APTs Wolfgang (T6) and Amadeus (T7) with T8 in the back. *Right:* Shown is Amadeus (T7) in the parking position with T8 in the back.

In early 1996 the University of Vienna acquired two almost identical 0.75-m automatic photoelectric telescopes (APTs) from Fairborn Observatory, which were named Wolfgang and Amadeus. Until summer of 1996 they operated at the Smithsonian Fred L. Whipple Observatory on Mount Hopkins. By the fall of 1996 all

Mount Hopkins-based APTs were relocated to the new Fairborn site at Washington Camp in southern Arizona, see Fig. 2.3.

The twin telescope was designed and constructed at the Fairborn Observatory in 1992. The optical design consists of two 0.75-m Cassegrain systems with $f/2$ primary mirrors and $f/8$ overall focal ratios. While *Wolfgang* operates in the blue with UBV filter, *Amadeus* operates in the red with $V(RI)_C$ filter systems. Both telescopes as well as the observatory itself are fully automatic. Further details of the performance of the system were reported by Strassmeier et al. (1997b).

The bulk of photometry of XX Tri analyzed in this thesis was taken with *Amadeus* between 1996 and 2013. Photometric observations before 1996 were published by Strassmeier et al. (1997a). Oláh et al. (2014) investigated the long-term trend of XX Tri using 28 years of photometric observations including 20 years of observations with *Amadeus* (1993-2013). In this thesis we are focused on the seasonal variations and their periodicity.

2.3 New spectroscopic observations

Time-series high-resolution echelle spectroscopy of XX Tri was taken with the 1.2-m STELLA telescopes and the STELLA Echelle Spectrograph (SES) on a nightly basis between July 2006 and April 2012. The STELLA observatory is located at the Izana Observatory on Tenerife and operates fully robotic with two 1.2-m telescopes (Strassmeier et al. 2004, 2010b), see Fig. 2.4. The SES is a white-pupil spectrograph with an R2 grating with two off-axis collimators, a prism cross disperser and a folded Schmidt camera with an e2v 2k×2k CCD as the detector, the latter two items were replaced by a fully refractive camera and an e2v 4k×4k CCD in mid 2012. In 2010, the SES fiber was moved to the prime focus of the second STELLA telescope (STELLA-II) while STELLA-I now hosts the Wide-Field STELLA Imaging Photometer (WiFSIP). Further details of the performance of the system were reported by Granzer et al. (2010) and Weber et al. (2012).

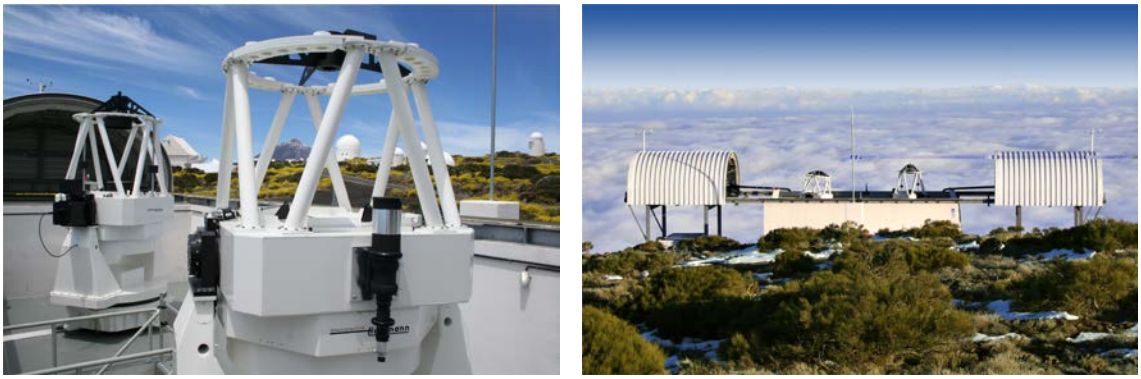

Figure 2.4: STELLA observatory with its two 1.2-m STELLA telescopes.

A total of 667 usable spectra from six observational seasons were obtained. All spectra cover the wavelength range from 388-882 nm with increasing inter-order gaps near the red end starting at 734 nm towards 882 nm before the camera and CCD exchange. The resolving power is R = 55,000 corresponding to a spectral resolution of 0.12 Å at 650 nm.

The integration time was set to 7200 s due to the relative faintness of the target for a 1m-class telescope. Depending on weather conditions, the averaged signal-to-noise (S/N) ratios are between 50-300:1 for each spectrum but typically 150:1. SES spectra are automatically reduced using the IRAF-based STELLA-SES data-reduction pipeline (Weber et al. 2008). The images were corrected for bad pixels and cosmic-ray impacts. Bias levels were removed by subtracting the average overscan from each image followed by the subtraction of the mean of the (already overscan subtracted) master bias frame. The target spectra were flattened by a nightly master flat which itself is constructed from around 50 individual flats observed during dust, dawn, and around midnight. After removal of scattered light, the one-dimensional spectra were extracted using an optimal-extraction algorithm. The blaze function was then removed from the target spectra, followed by a wavelength calibration using consecutively recorded Th-Ar spectra. Finally, the extracted spectral orders were continuum normalized by fitting a synthetic spectrum of the same spectral classification as XX Tri.

Fig. 2.5a shows an example spectrum (Echelle order #89) from HJD 2,454,146.37 while Fig. 2.5b gives an overview of the time and phase sampling of all 667 STELLA spectra.

2.4 Redetermination of astrophysical properties

Several astrophysical properties of XX Tri and its binary system were determined by Strassmeier (1999). Since then more than a decade of photometric observations were taken. Additionally, spectroscopy is continuously performed since 2006, using the STELLA-telescope on Tenerife. Furthermore, the revised reduction of the *Hipparcos* data increased the measured parallax of XX Tri by almost 25 %. Thus, within this section, we redetermine the properties of XX Tri and its binary system. The most important astrophysical properties of XX Tri are summarized in Table 2.2.

Magnitude and luminosity

The revised reduction of the *Hipparcos* data (van Leeuwen 2007) yielded a parallax of 6.24 ± 1.02 mas and fixed the distance of XX Tri (HIP 9630) to 160^{+32}_{-22} pc. With an apparent maximum visual magnitude of $7\overset{\mathrm{m}}{.}76$ (Oláh et al. 2014), the absolute visual magnitude of XX Tri is $M_V = 1\overset{\mathrm{m}}{.}58^{+0.32}_{-0.40}$. Interstellar absorption was taken into account with $0\overset{\mathrm{m}}{.}1$ per 100 pc (Strassmeier 1999). We note that Oláh et al. (2014) estimated the reddening of XX Tri from all-sky infrared imaging and found a color excess $E(B-V)$ of $\approx 0\overset{\mathrm{m}}{.}05$, which leads to the same value of extinction as above. With a bolometric correction of $-0\overset{\mathrm{m}}{.}517$ (Flower 1996), the bolometric magnitude of XX Tri is $1\overset{\mathrm{m}}{.}06$ and, with an absolute magnitude for the Sun of $M_{\mathrm{bol},\odot} = 4\overset{\mathrm{m}}{.}75$, the luminosity must be approximately 30^{+13}_{-8} $\mathrm{L}_\odot$.

Atmospheric surface stellar parameters

Atmospheric surface stellar parameters (effective temperature, gravity, metallicity, and $v \sin i$) were determined with the program PARSES (Allende Prieto 2004; Jovanovic et al. 2013), which is included in the SES data reduction pipeline. It fits

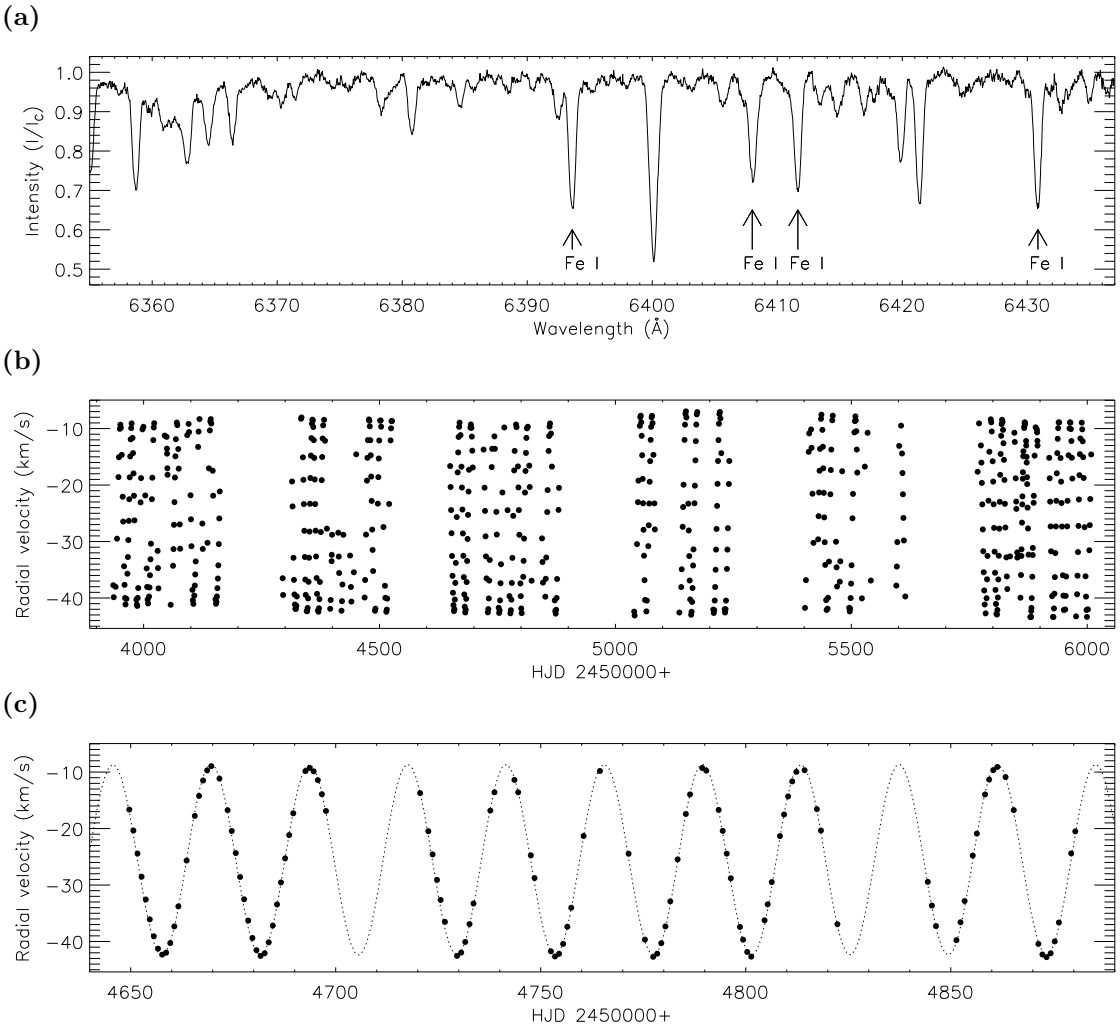

Figure 2.5: STELLA spectroscopy of XX Tri. a) A section of a representative single spectrum showing a subset of the spectral lines used for the Doppler-imaging inversions. b) The full time series radial velocities from a cross-correlation analysis. It shows the rotational phase sampling for the STELLA spectra. c) A section of b) referring to the observational season 2008/09. The dotted line represents a radial-velocity fit.

synthetic spectra to a defined spectral region, in our case most echelle orders between 480-750 nm, using MARCS model atmospheres (Gustafsson et al. 2008). We verified this approach by applying it to the ELODIE library (Prugniel & Soubiran 2001), and used linear regressions to the offsets with respect to the literature values to correct the zero point of our PARSES results. In Fig. 2.6 these corrected values are shown for all spectra (excluding 3-σ outliers). For more details of this procedure we refer to previous applications (e.g. Strassmeier et al. 2010a, 2012). The mean values are $T_{\rm eff}$ of 4620 ± 30 K, a gravity $\log g$ of 2.82 ± 0.04, a $v \sin i$ of 19.9 ± 0.7 km s^{-1} and a metallicity of -0.13 ± 0.04 dex relative to the Sun. Its errors are internal errors based on the root-mean-square (RMS) of the entire time-series. We note that the above effective temperature is close to what Oláh et al. (2014) obtained from VI photometry during maximum photometric brightness but that the metallicity differs by a factor of two.

Table 2.2: Astrophysical properties of XX Tri (HD 12545). Values not cited in the third column were obtained in this thesis. Note that the errors for spectrum-synthesis related parameters are internal errors.

Parameter	Value	Based on
Classification, MK	K0III	Strassmeier (1999)
Distance, pc	160^{+32}_{-22}	van Leeuwen (2007)
$V_{\max}$, mag	7.76	Oláh et al. (2014)
$V - I_C$, mag	1.18	Oláh et al. (2014)
Rotation period, d	≈ 24.0	Strassmeier (1999)
Orbital period, d	23.9674 ± 0.0005	radial velocities
Inclination, deg	60 ± 10	Strassmeier (1999)
$v \sin i$, km s^{-1}	19.9 ± 0.7	spectrum synthesis
Temperature, K	$4{,}620 \pm 30$	spectrum synthesis
Log gravity, cgs	2.82 ± 0.04	spectrum synthesis
Metallicity, $[\mathrm{Fe/H}]_\odot$	-0.13 ± 0.04	spectrum synthesis
Microturb., km s^{-1}	1.5	spectrum synthesis
Macroturb., km s^{-1}	3.0	spectrum synthesis
Radius, $\mathrm{R}_\odot$	10.9 ± 1.2	from $R \sin i$ and i
Luminosity, $\mathrm{L}_\odot$	30^{+13}_{-8}	from M_{bol}
Mass, $\mathrm{M}_\odot$	1.26 ± 0.15	evolutionary tracks
Age, Gyr	7.7 ± 3.1	evolutionary tracks

Fig. 2.6 also shows that the plotted values are systematically variable. In particular the effective temperature and the line broadening clearly vary with the rotational period of the star but also from season to season. This behavior is investigated in more detail in the following Sections 2.5 and 2.6, where we compare the spectrum-integrated values from PARSES with observed broad-band lightcurves.

Mass and age

To determine the mass and age of XX Tri, a trilinear interpolation between stellar evolutionary tracks (Bertelli et al. 2008) based on a Monte-Carlo (MC) method (Künstler 2008; Reffert et al. 2015) was used. The evolutionary tracks are available for different metallicities ($0.0001 \leq Z \leq 0.070$) and masses ($0.15\ \mathrm{M}_\odot \leq M \leq 2.5\ \mathrm{M}_\odot$) and cover the evolution of the stars from the zero age main sequence (ZAMS) up to the end of the thermal pulses along the asymptotic giant branch (TP-AGB). Within the three-dimensional space (L, T_{eff}, [Fe/H]) 10,000 random positions with Gaussian distribution were generated, taking the errors of L, T_{eff}, and [Fe/H] into account. For each generated position, we calculated the mass and age. The obtained mean values are a mass of $1.26 \pm 0.15\ \mathrm{M}_\odot$ and an age of 7.7 ± 3.1 Gyrs. Fig. 2.7 shows evolutionary tracks interpolated to the metallicity of XX Tri including the star's position.

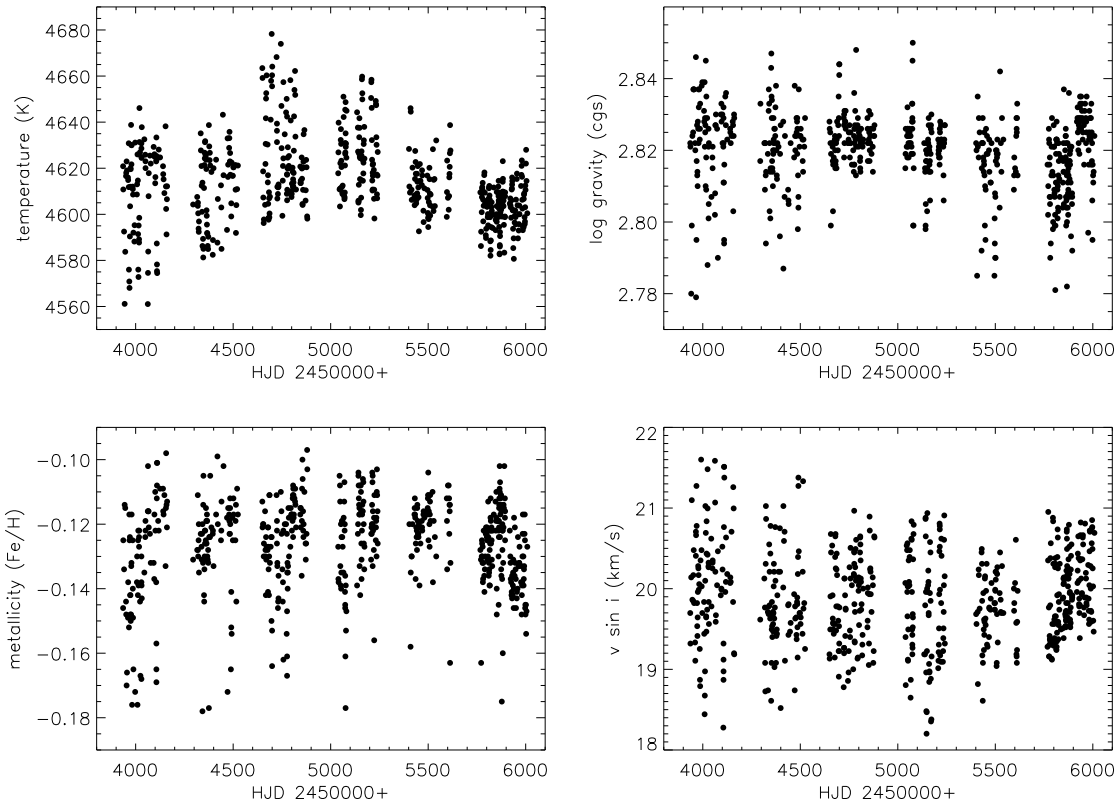

Figure 2.6: Stellar parameter determination with PARSES. Shown are the obtained values for effective temperature, log gravity, metallicity, and $v \sin i$ for all spectra excluding 3-σ outliers.

Radius

A rotation period of 24.0 days together with a $v \sin i$ of 19.9 ± 0.7 km s^{-1} yields a minimum radius of $R \sin i = 9.4 \pm 0.3$ R$_\odot$. With an inclination of $i \approx 60 \pm 10°$ (Strassmeier 1999), the stellar radius is $R = 10.9 \pm 1.2$ R$_\odot$. The unprojected equatorial rotational velocity would then be $v_{\rm eq} = 23.0$ km s^{-1}.

We note that the determination of radius for active giants is crucial and method-depending. With the values for temperature and luminosity we determine a radius of $R = 8.5 \pm 1.4$ R$_\odot$, suggesting XX Tri to be rather a subgiant, or III-IV, than a fully fledged K0 III giant. Using mass and gravity results in a radius of $R = 9.2 \pm 1.1$ R$_\odot$. However, both results are within two sigma and therefore reliable.

Orbital elements and companion star

In this thesis, we use revised orbital elements from our radial-velocity fit of the STELLA data, see Fig. 2.5c: $P_{\rm orb} = 23.9674 \pm 0.0005$ days, $\gamma = -25.389 \pm 0.031$ km s^{-1}, $e = 0$ (adopted), $K = 16.772 \pm 0.044$ km s^{-1}, $a \sin i = 5.528 \pm 0.014 \times 10^6$ km, and $f(M) = 0.0117 \pm 0.0001$. Throughout this thesis phase is always computed from a time of maximum positive radial velocity with the revised orbital period,

$$HJD = 2,453,926.6663 + E \times 23.9674 \; . \tag{2.1}$$

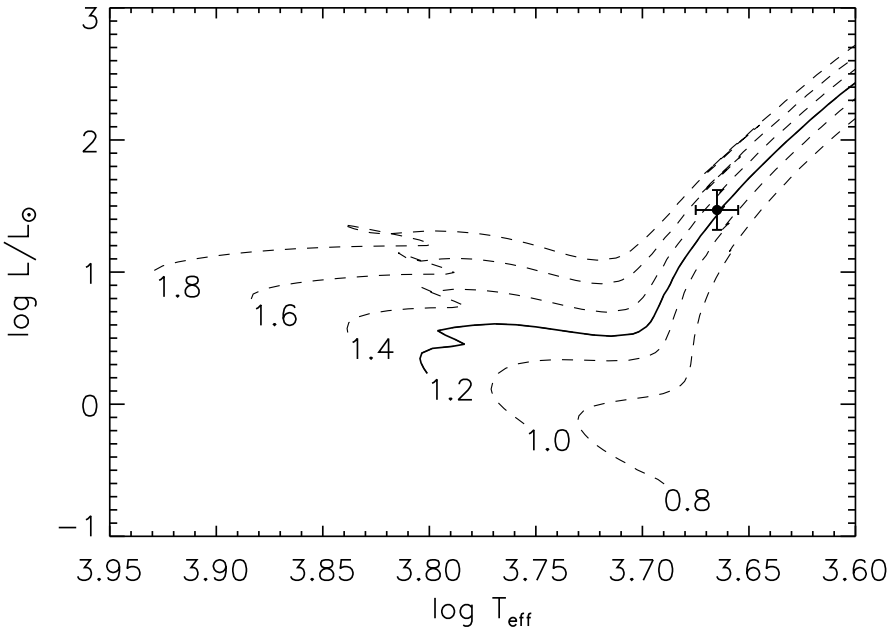

Figure 2.7: Shown are stellar evolutionary tracks (Bertelli et al. 2008) together with the position of XX Tri (*cross*). Each track is interpolated to a metallicity of −0.13 and covers the range from the ZAMS up to the RGB. The stellar mass (in $M_\odot$) is indicated at the initial point of evolution.

The revised mass function, together with the primary mass of 1.26 $M_\odot$ and an orbital inclination of $i \approx 60°$, suggests a low-mass secondary star with a mass of ≈ 0.36 $M_\odot$. Because the secondary is not seen in the spectrum, the most likely secondary star is then a red dwarf of spectral type M.

2.5 Spectroscopic analysis

As we have already seen in Fig. 2.6, the values of atmospheric surface parameters are systematically variable. In particular the effective temperature and the line broadening vary with the stellar rotation period, but also from season to season, as seen in Fig. 2.8 and Fig. 2.9, respectively. The seasonal variations are between 50 to 100 K in temperature and between 2 to 4 $km\,s^{-1}$ in line-broadening. Their overall variation is about 100 K and 4 $km\,s^{-1}$, respectively.

We assume that the rotational-modulated variations in temperature correlates with the presence of starspots. Thus, the temperature variation phased on the stellar rotation should give us information about the longitudinal appearance of starspots. Such spot signatures are clearly seen in Fig. 2.8 from season to season. During the observational season 2006/07 a large cool spot should be visible at a phase of ≈ 0.7, whereas during 2007/08 it should appear at a phase of ≈ 0.5. In 2008/09 two large spots very close to each other should be seen at phases of ≈ 0.4 and 0.7, respectively. Again, during 2009/10, two large spots should appear shifted by 180° at phases of ≈ 0.2 and 0.7, respectively. In the two following seasons, again two spots should be visible, with a larger and a smaller one, located at phases of ≈ 0.1 and 0.7 during 2010/11, and at phases of ≈ 0.4 and 0.9 during 2011/12.

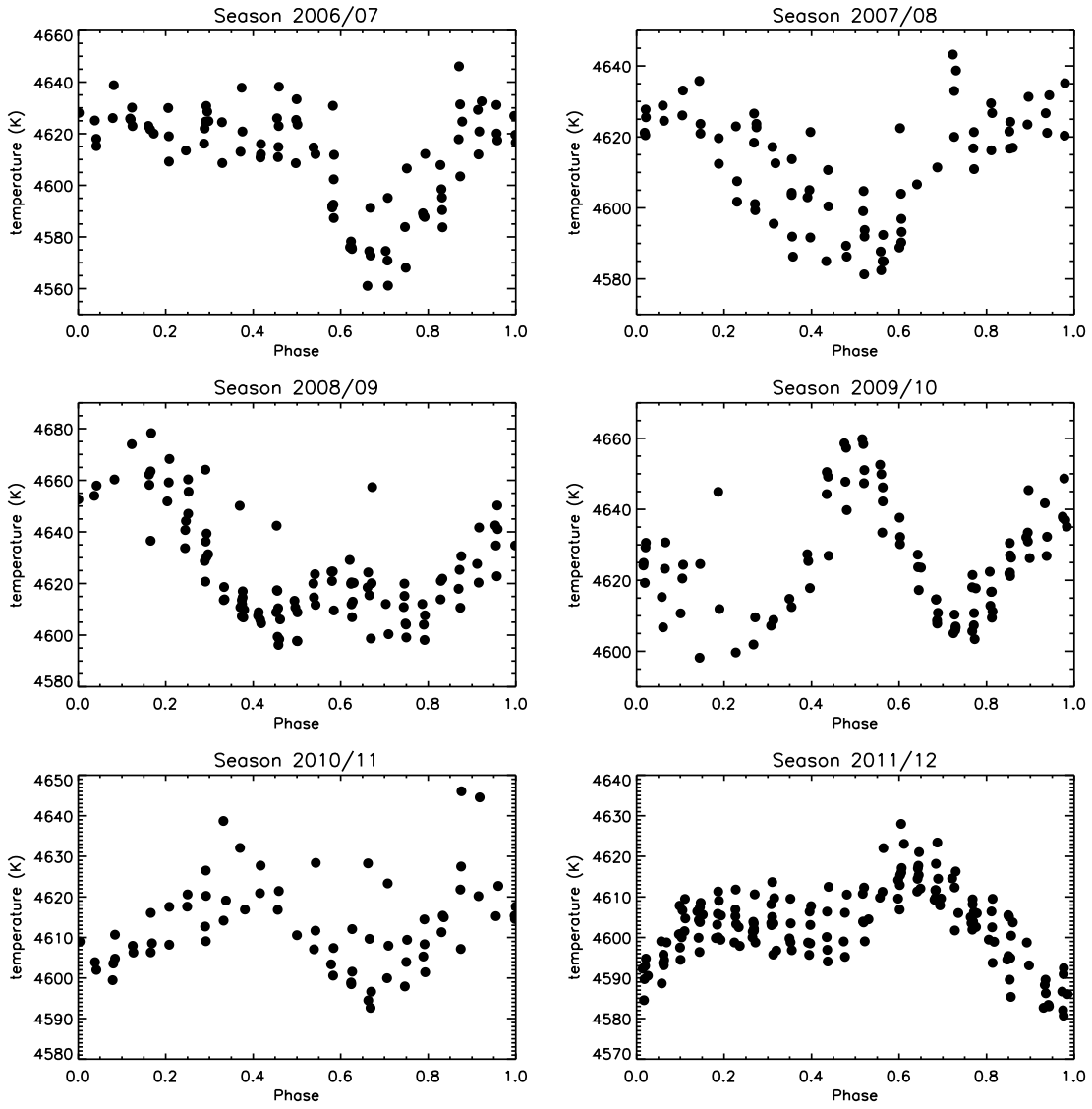

Figure 2.8: Temperature variations with PARSES. Shown are the obtained values in rotational-modulation for each observing season. Large spots could be responsible for the variations, disclosing their longitudinal appearance.

We note that only larger spots will show a significant temperature variation, as smaller spots (cool and/or hot) could be difficult to detect. If, e.g., a cool and a hot spot appear on the same longitude, their different temperature "signal" could be vanished. Furthermore, the signature of a small spot appearing close to a larger one could be hidden in the signal of the large spot. The latitudinal location of a spot also have a strong influence of its "detection". During a rotation, a large spot near the equator distort the rotational-modulated line profiles, and therefore its temperature fitting, much stronger than a small spot near the pole. In addition, a spot covering the polar cap do not show any rotational-modulated temperature variation.

Fig. 2.10 show the corresponding Lomb-Scargle periodograms (Scargle 1982). The main periods are around 24 days and/or its half, suggesting the presence of one or two large spots, respectively. The accumulation of peaks between $\approx$ 23-25 days could be signs for differential rotation and/or spot evolution.

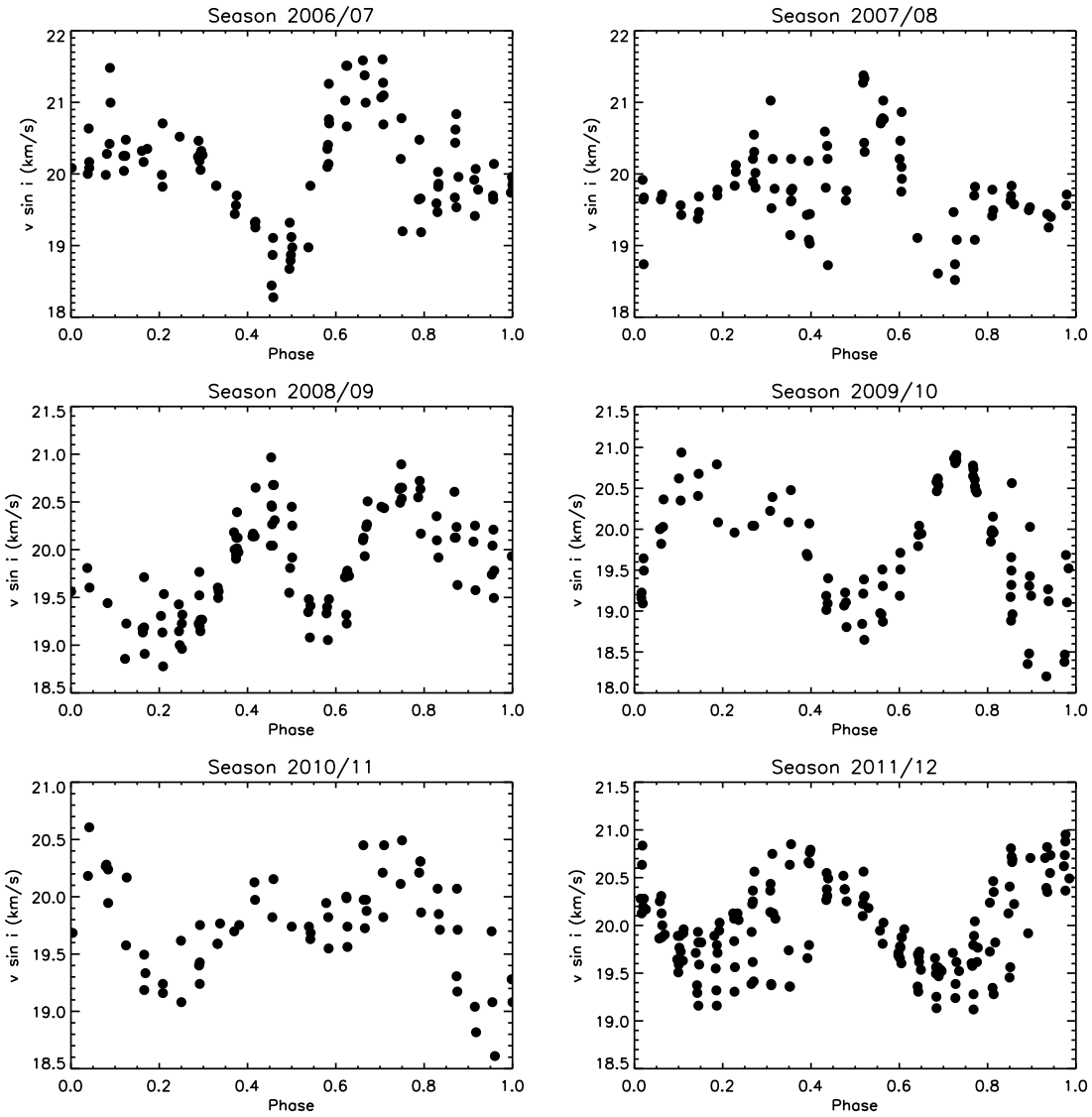

Figure 2.9: Line-broadening variations with PARSES. Shown are the obtained values in rotational-modulation for each observing season.

Line-broadening measurements are generally influenced by starspots, as they are causing distortions in the line profile, depending on their appearance on the surface of the star. If, e.g., a cool spot crosses the visible hemisphere, the line-broadening is at maximum when the spot appears in line-of-sight (LOS), and at minimum when the spot appears and disappears at an angle of $\approx \pm 60$-90° relative to LOS. When the spot rotates out of sight, the corresponding "bump" in the line profile disappears and thus the line-broadening slightly increases, and vice versa. We note that Fig 3.1 in Chapter 3 illustrates this behavior, reminding that our target star has a $v \sin i$ of just ≈ 20 km s^{-1}. Thus, the rotational-modulated variations in line-broadening should be inverse compared to the temperature variations and appear twice per rotation. The inverse correlation is clearly seen by comparing Fig. 2.8 and Fig. 2.9, as well as the duplicated periodicity. Thus, depending on the number and position of spots, the corresponding periodograms reveal shorter periods, seen in Fig. 2.11, where another period at ≈ 8 days beside the periods of 12 and/or 24 days is detected.

2.6 Photometric analysis

We analyze differential VI-photometry of XX Tri observed with *Amadeus* (Chapter 2.2) between 1996 and 2013. The comparison star is HD 12478 with $V = 7.77$ and $I = 6.37$. We are interested in particular in the rotation period of XX Tri and the rotational modulation during the observational seasons 2006-2012 in order to compare with our spectroscopic analysis.

The orbital period of XX Tri is determined with high precision, see Chapter 2.4. The photometric period determined so far, based on different observations which partly covered only a few rotations. We determine the photometric period for each observational season from 1996 to 2013 in V, I, and $V - I$.

Before analyzing, we applied a statistical procedure that eliminated all data with an internal photometric error greater than $\pm 0\overset{\text{m}}{.}02$, as well as data that deviated from the rest by at least $3\,\sigma$. We note, that due to the large long-term variations (Fig. 2.2) we applied this method for each individual season. Furthermore, we note that for the last three seasons (2010/11 - 2012/13) we doubled the internal photometric error to $\pm 0\overset{\text{m}}{.}04$ for elimination, due to tracking problems of the target star, which increased the photometric error roughly by a factor of two. Anyway, no clear signal with a false-alarm-probability (FAP) of less than 10^{-3} is detected for these seasons. Therefore, the determined mean values of periods are not influenced by these data, as only signals with FAP $\leq 10^{-5}$ are taken into account.

Table 2.3 summarizes our photometry log. The year indicates the observing season, then its Heliocentric Julian Date range, the time elapsed in days, the number of observations N, the minimum, maximum and mean magnitudes for V, I and $V - I$, respectively, and their associated periods.

Our determined mean values for photometric periods are in good agreement with previous measurements. In particular the mean period $<P_{V-I}> = 23.97 \pm 0.03$ d is in very good agreement with the orbital period of $P_{\text{orb}} = 23.9674 \pm 0.0005$ days. We note that the determined values vary from season to season between 23.8 and 24.5 days, which could be signs for differential rotation and/or spot evolution.

Fig. 2.12 - 2.17 show the VI-photometry for each observational season between 2006 and 2012, including their rotational-modulation, and their Lomb-Scargle periodograms. It is more than likely that the rotationally modulated variations are caused by starspots. Comparing them with the temperature variations from spectroscopic line profile analysis (Fig. 2.8), reveals an impressive agreement in position and even strength of signal.

Even the long-term trends between photometric and spectroscopic analysis fully agree. The V-magnitude decreases between the observational seasons 2006/07 - 2008/09, and increases between 2008/09 - 2011/12, see Fig. 2.18. We also have seen this behavior in temperature, determined with PARSES, see Fig. 2.6. The corresponding periodograms (Fig. 2.18 and Fig. 2.10) reveals the same accumulation of peaks between $\approx$ 23-25 days, as well as a peak around 12 days, caused by spots on opposite hemispheres.

Summarized, we get a quite clear picture about starspot distribution on XX Tri during 2006-2012, provided by photometry and spectroscopy. We note that, even if this agreement should be obvious from the theoretical point of view, two completely different datasets are investigated. In Chapter 4.1 we will compare these results with temperature lightcurves obtained from our Doppler maps.

Table 2.3: Photometry log, VI magnitudes and periods.

Season	HJD range	Δt	$N^{(a)}$	V magnitude			I magnitude			$(V-I)$ magnitude			Period[b]		
Year	(2450000+)	(d)		$V_{\min}$	$V_{\max}$	V_{mean}	$I_{\min}$	$I_{\max}$	I_{mean}	$(V-I)_{\min}$	$(V-I)_{\max}$	$(V-I)_{\text{mean}}$	P_V (d)	P_I (d)	P_{V-I} (d)
1996/1997	396-501	105	118 (147)	8.14	8.47	8.29	6.87	7.11	6.99	1.26	1.36	1.30	23.84 ± 0.10	23.81 ± 0.09	23.89 ± 0.13
1997/1998	714-881	167	199 (250)	7.95	8.55	8.23	6.73	7.18	6.94	1.21	1.38	1.29	24.02 ± 0.10	24.02 ± 0.08	24.00 ± 0.07
1998/1999	1077-1247	170	208 (229)	8.05	8.56	8.29	6.81	7.18	6.99	1.24	1.39	1.30	23.95 ± 0.08	23.89 ± 0.08	24.05 ± 0.08
1999/2000	1435-1591	156	209 (255)	7.94	8.58	8.24	6.72	7.22	6.96	1.20	1.37	1.28	23.93 ± 0.07	23.89 ± 0.06	24.01 ± 0.07
2000/2001	1806-1963	157	39 (137)	8.14	8.44	8.29	6.90	7.12	7.00	1.23	1.34	1.30	—	—	—
2001/2002	2182-2327	145	160 (249)	8.00	8.30	8.15	6.76	7.00	6.88	1.24	1.31	1.27	23.97 ± 0.11	24.01 ± 0.11	23.88 ± 0.16
2002/2003	2534-2693	159	201 (265)	7.96	8.16	8.07	6.73	6.89	6.81	1.20	1.29	1.26	23.80 ± 0.07	23.78 ± 0.09	23.82 ± 0.10
2003/2004	2895-3050	155	168 (270)	7.93	8.32	8.11	6.70	7.03	6.86	1.19	1.32	1.25	23.97 ± 0.11	23.96 ± 0.12	24.00 ± 0.16
2004/2005	3277-3416	139	184 (246)	7.92	8.14	8.04	6.69	6.85	6.78	1.21	1.30	1.26	23.91 ± 0.14	23.98 ± 0.15	23.79 ± 0.13
2005/2006	3561-3791	230	237 (335)	7.92	8.16	8.04	6.69	6.86	6.78	1.23	1.31	1.27	23.82 ± 0.22	23.81 ± 0.24	23.81 ± 0.16
2006/2007	3997-4141	144	210 (306)	7.85	8.17	7.96	6.63	6.87	6.71	1.21	1.31	1.25	23.92 ± 0.24	23.94 ± 0.18	23.88 ± 0.27
2007/2008	4371-4517	146	182 (230)	7.81	8.05	7.91	6.60	6.79	6.67	1.20	1.28	1.24	24.35 ± 0.15	24.33 ± 0.15	24.47 ± 0.22
2008/2009	4729-4885	156	190 (254)	7.76	7.98	7.88	6.55	6.74	6.66	1.18	1.26	1.22	24.20 ± 0.26	24.28 ± 0.22	23.98 ± 0.26
2009/2010	5093-5242	149	186 (241)	7.84	8.09	7.95	6.63	6.88	6.74	1.15	1.26	1.21	—	—	—
2010/2011	5479-5546	67	65 (105)	7.89	8.05	7.98	6.70	6.88	6.78	1.16	1.23	1.20	—	—	—
2011/2012	5824-5971	147	47 (124)	7.93	8.11	8.02	6.71	6.94	6.83	1.14	1.24	1.19	—	—	—
2012/2013	6234-6330	96	27 (61)	7.87	8.23	8.04	6.68	7.02	6.82	1.16	1.25	1.21	—	—	—
1996-2013													23.93 ± 0.03[c]	23.93 ± 0.03[c]	23.97 ± 0.03[c]

Notes. [a] In parentheses is the number of observations before filtering. [b] All given periods have a false-alarm-probability (FAP) of less than 10^{-5}. [c] Resulting mean periods.

(a)

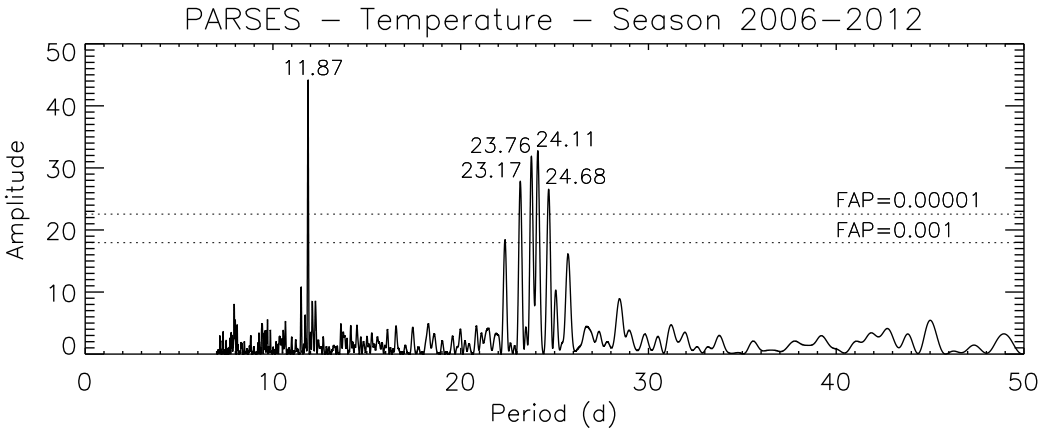

(b)

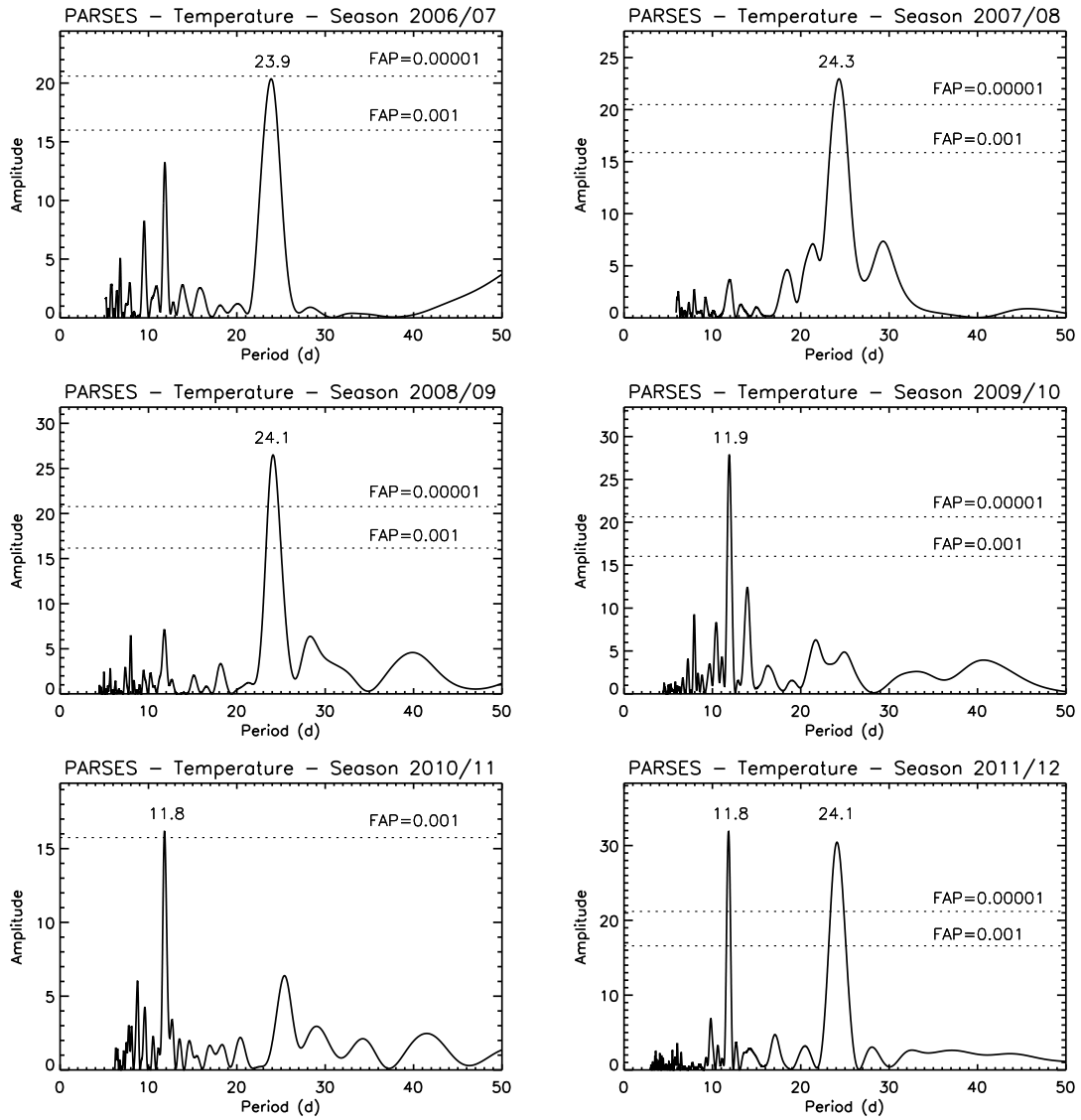

Figure 2.10: Periodograms for temperature variations from PARSES. a) Shown is the periodogram for 2006-2012. b) Shown are periodograms for each observing season.

(a)

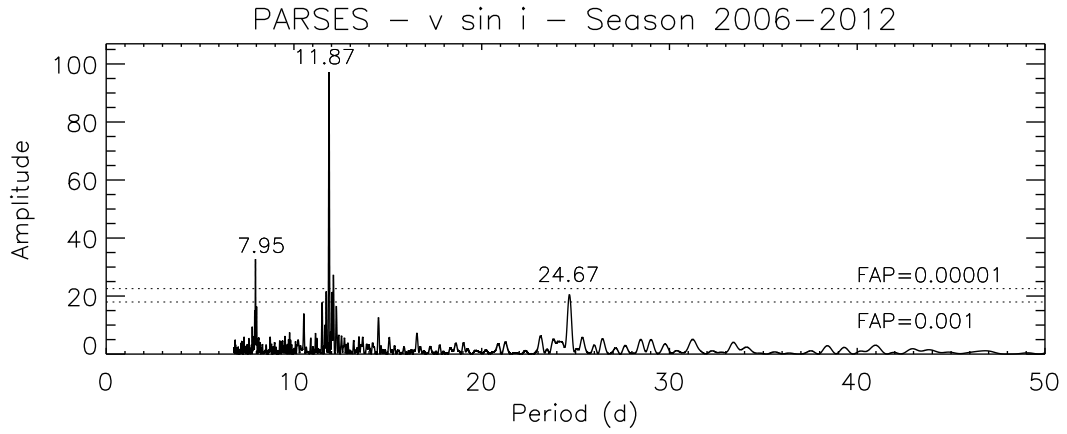

(b)

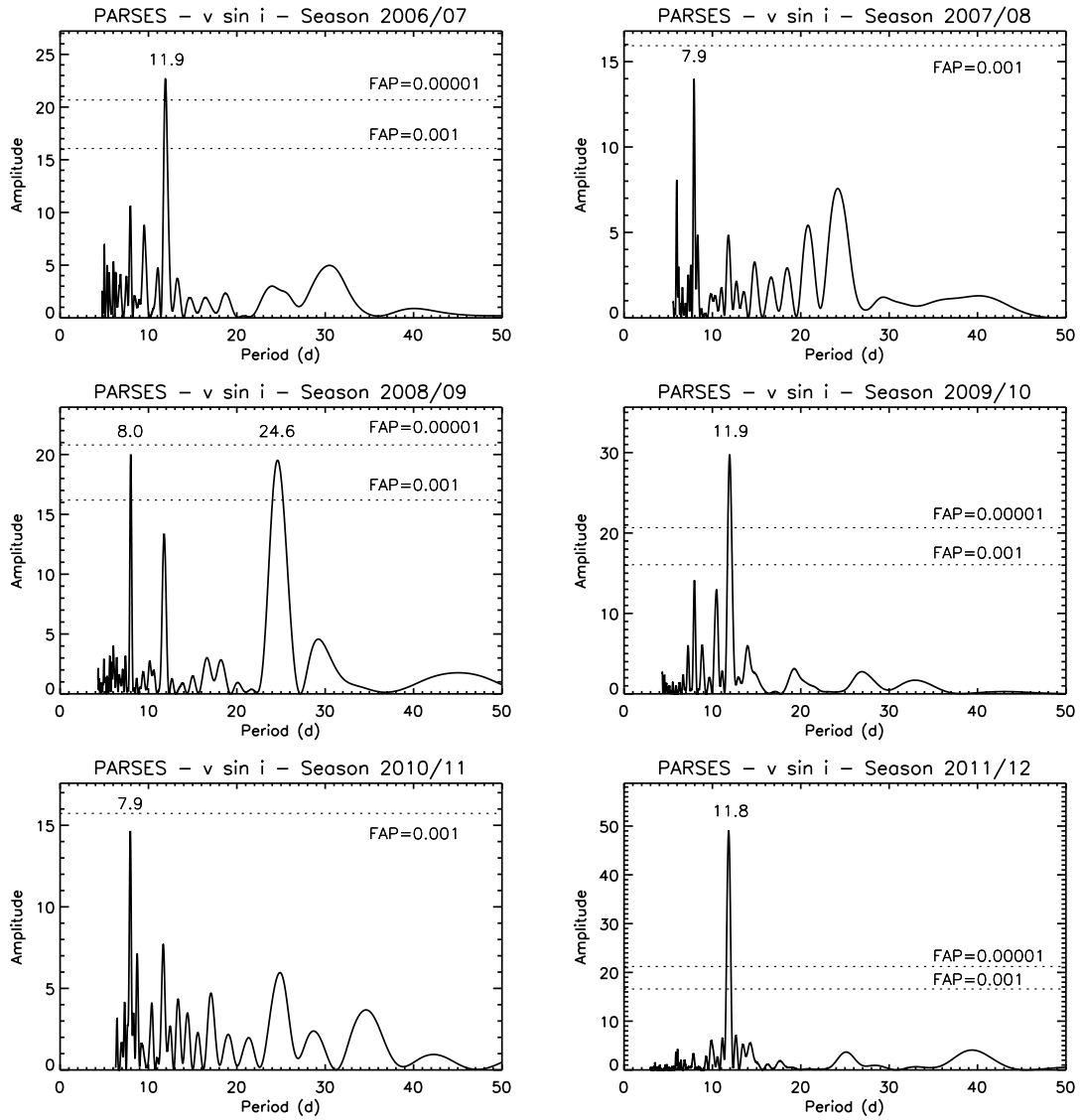

Figure 2.11: Periodograms for line-broadening variations from PARSES. a) Shown is the periodogram for 2006-2012. b) Shown are periodograms for each observing season.

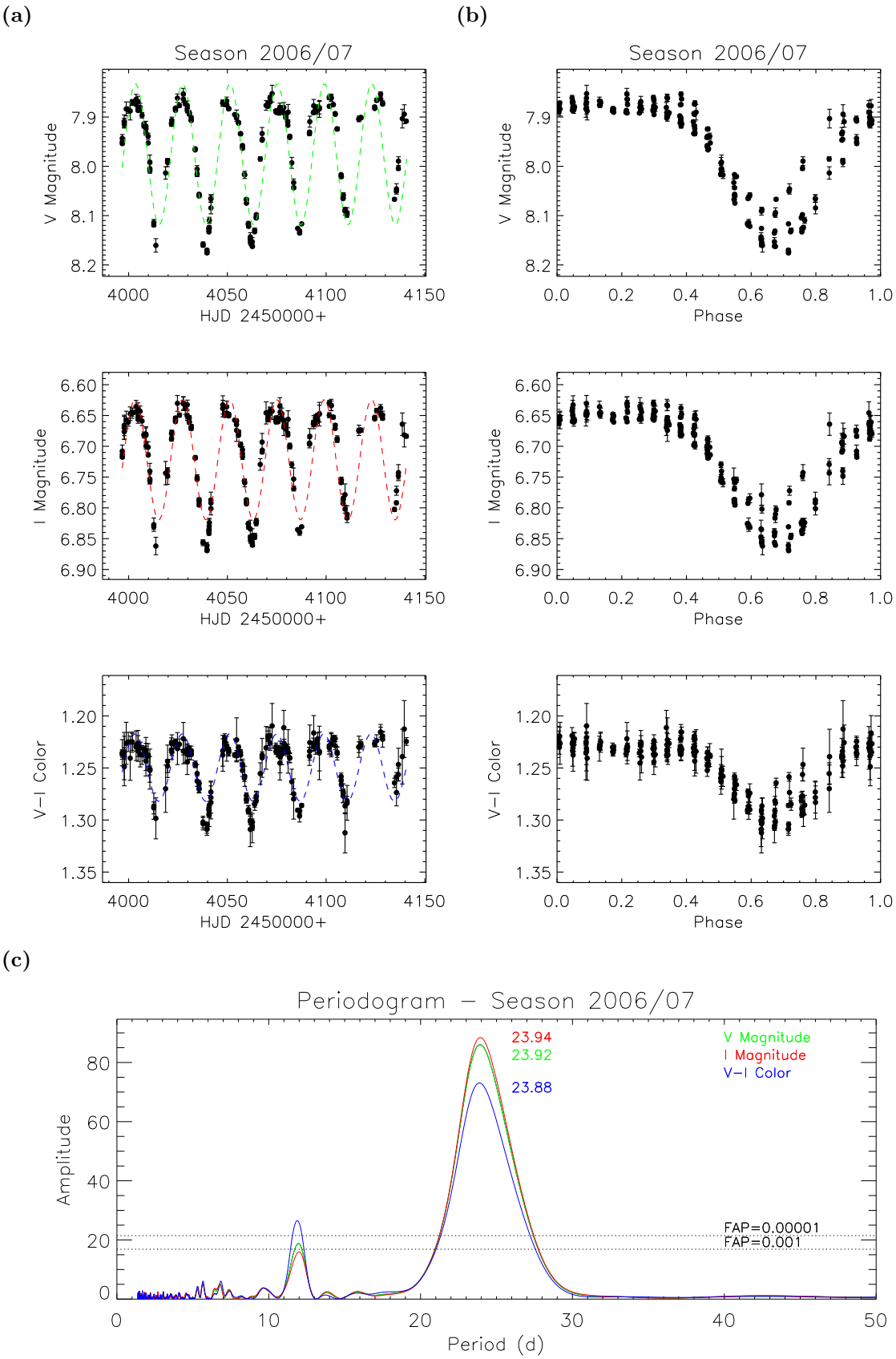

Figure 2.12: Photometry of XX Tri for the observing season 2006/07. a) Shown are V, I, and $V - I$ lightcurves. b) Rotational modulation in V, I, and $V - I$. c) Periodograms for each lightcurve.

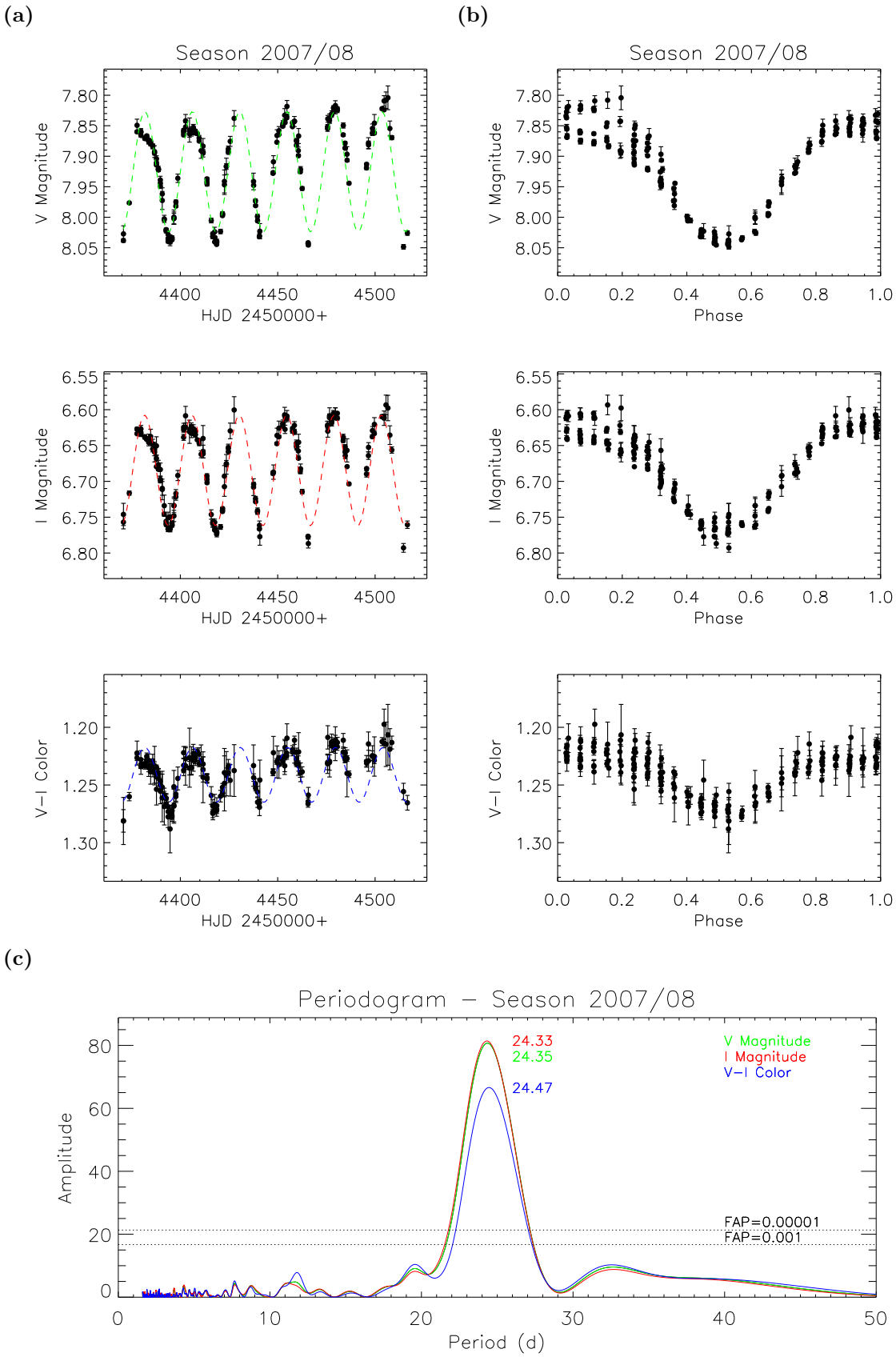

Figure 2.13: Photometry of XX Tri for the observing season 2007/08. a) Shown are V, I, and $V - I$ lightcurves. b) Rotational modulation in V, I, and $V - I$. c) Periodograms for each lightcurve.

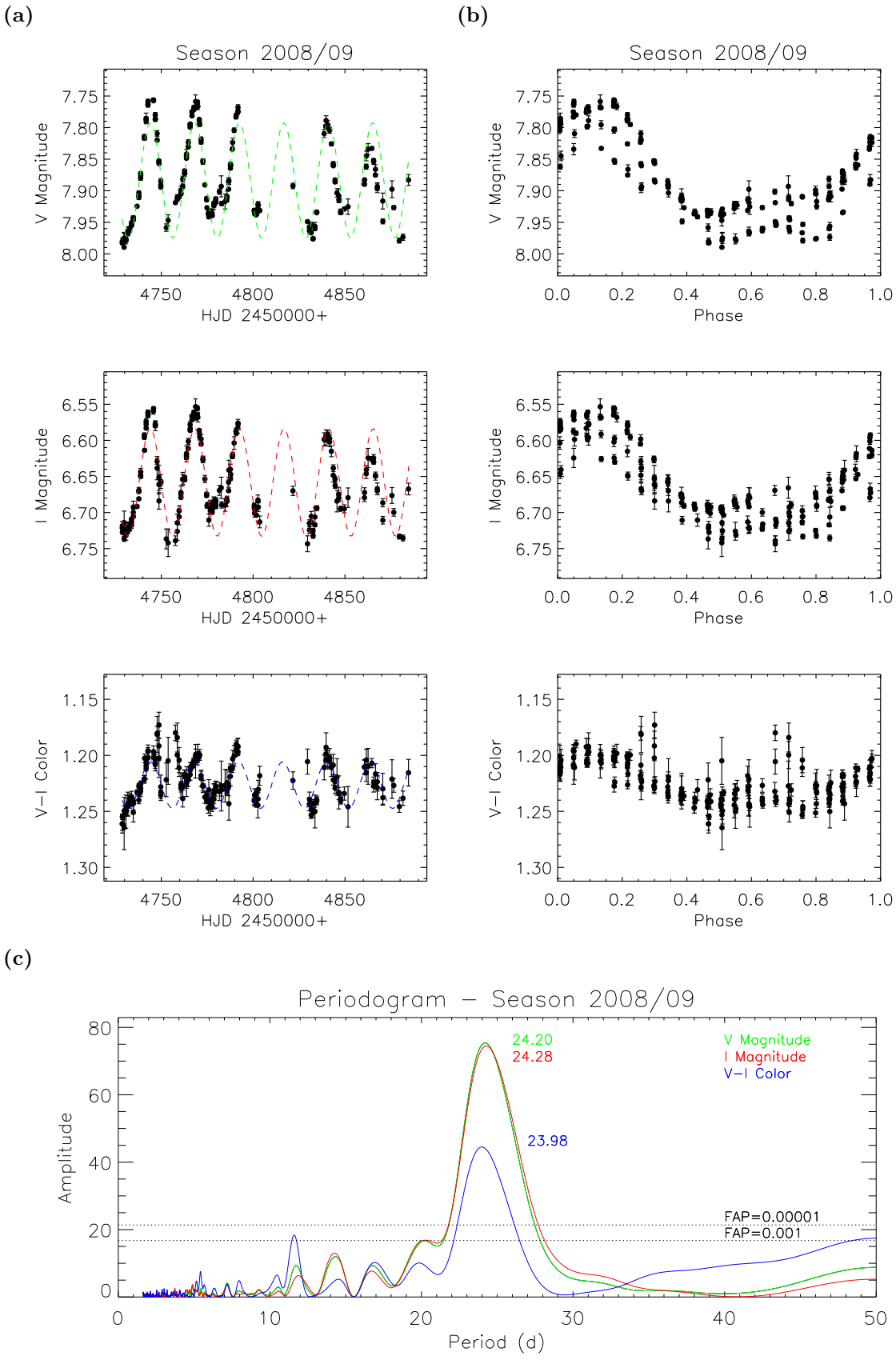

Figure 2.14: Photometry of XX Tri for the observing season 2008/09. a) Shown are V, I, and $V-I$ lightcurves. b) Rotational modulation in V, I, and $V-I$. c) Periodograms for each lightcurve.

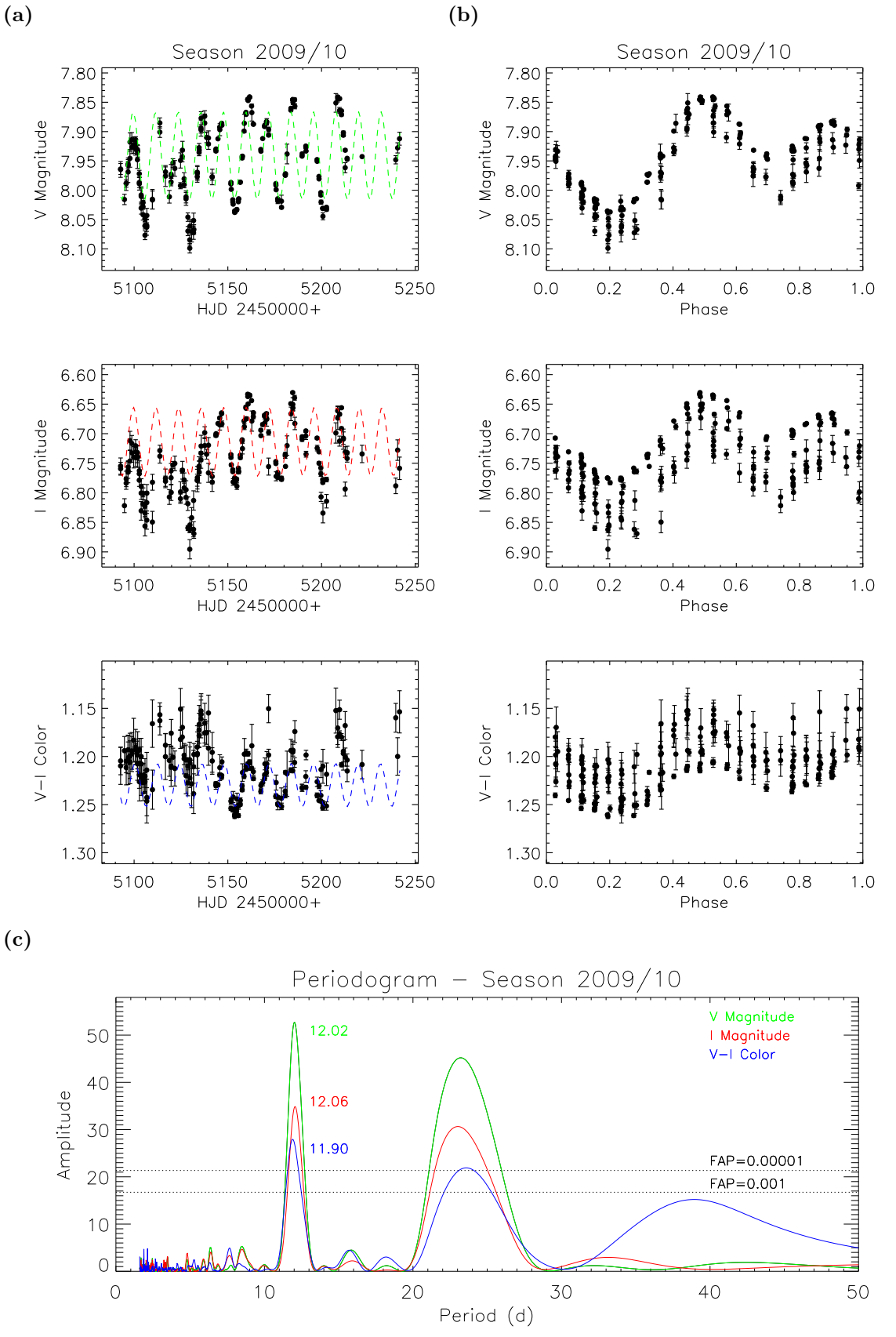

Figure 2.15: Photometry of XX Tri for the observing season 2009/10. a) Shown are V, I, and $V-I$ lightcurves. b) Rotational modulation in V, I, and $V-I$. c) Periodograms for each lightcurve.

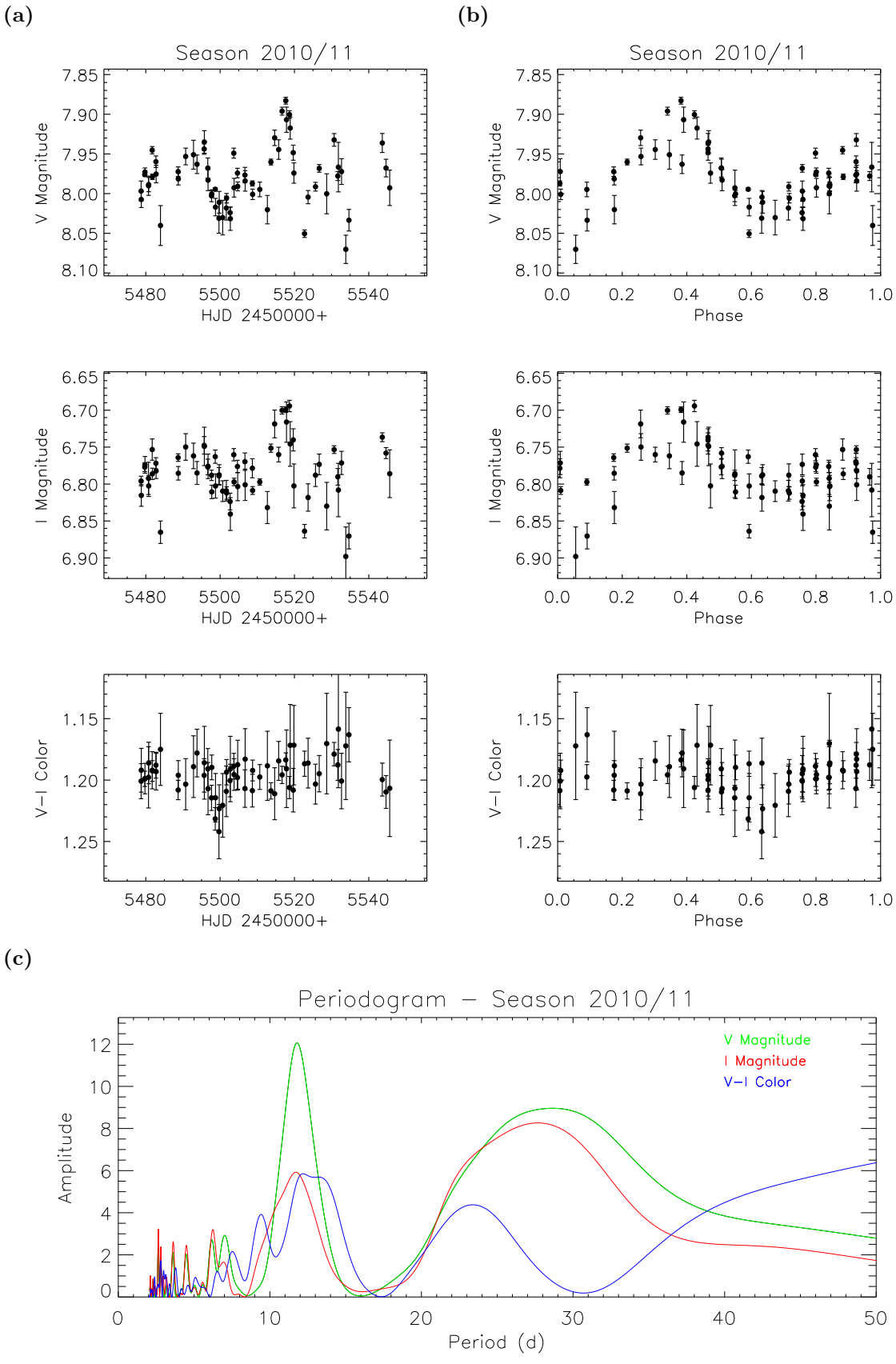

Figure 2.16: Photometry of XX Tri for the observing season 2010/11. a) Shown are V, I, and $V - I$ lightcurves. b) Rotational modulation in V, I, and $V - I$. c) Periodograms for each lightcurve.

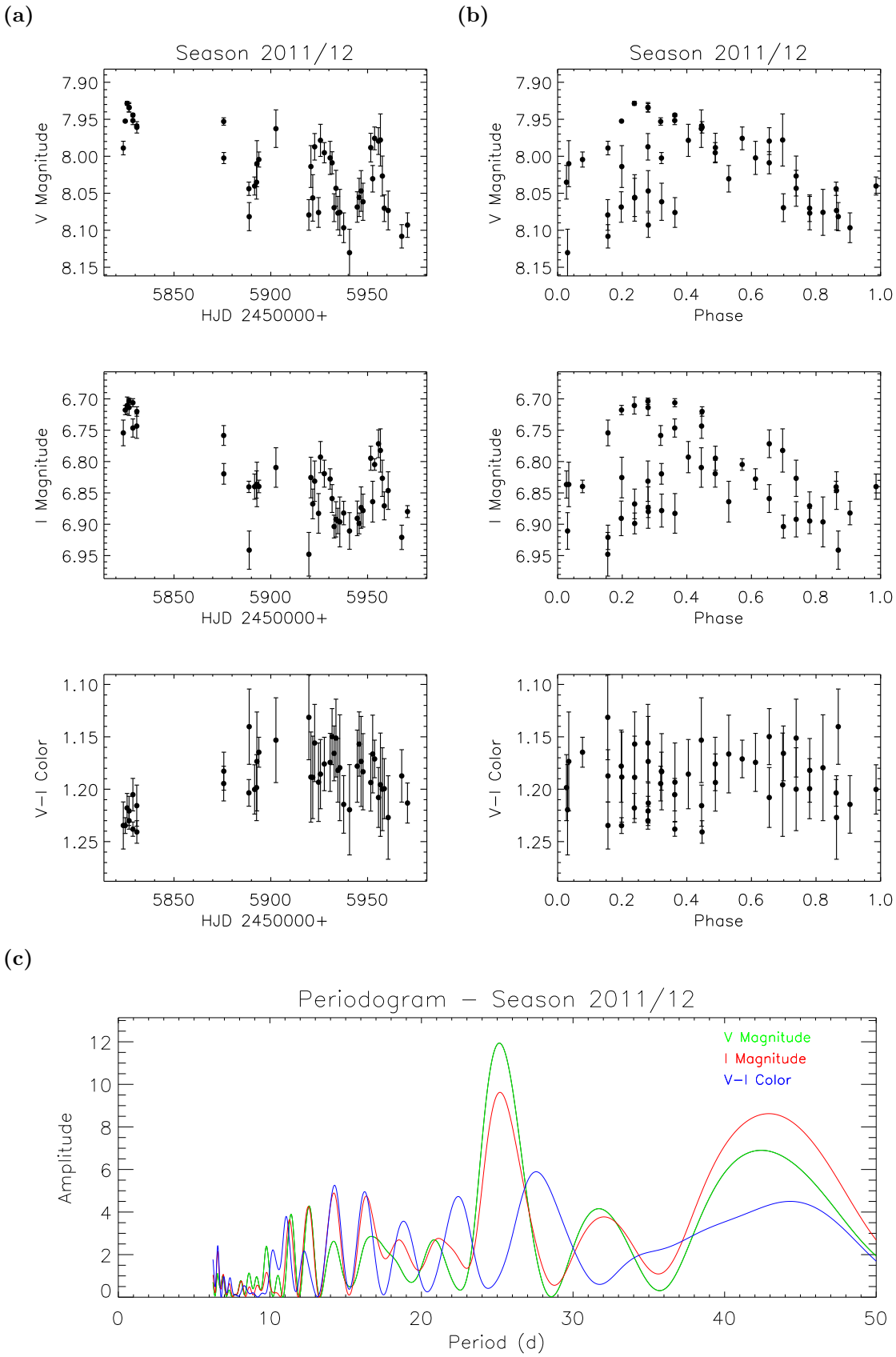

Figure 2.17: Photometry of XX Tri for the observing season 2011/12. a) Shown are V, I, and $V - I$ lightcurves. b) Rotational modulation in V, I, and $V - I$. c) Periodograms for each lightcurve.

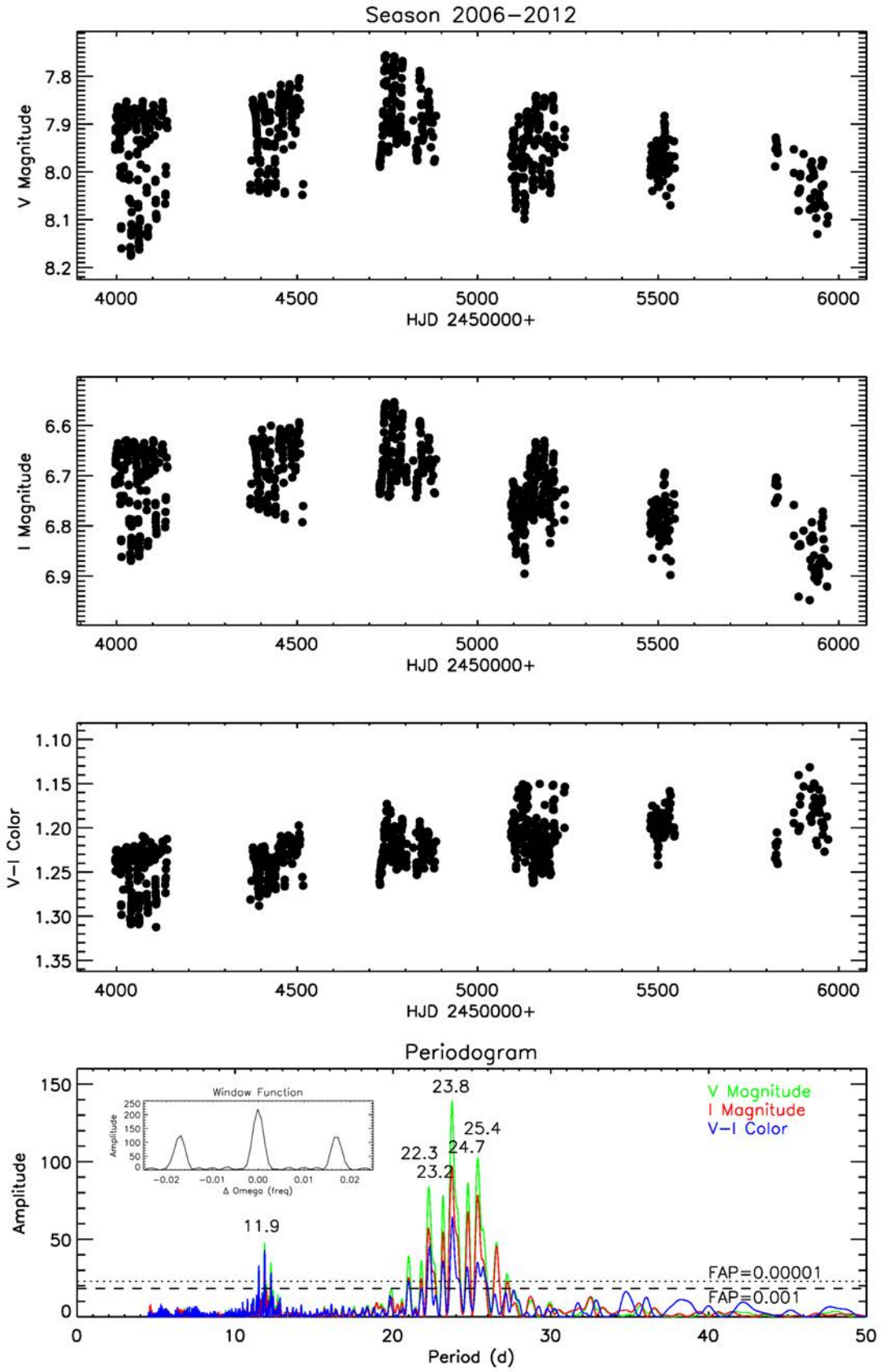

Figure 2.18: Photometry of XX Tri for the observing seasons 2006-2012. In the three upper panel the photometric lightcurves in V, I, and $V-I$ are shown. In the lower panel the periodograms for each photometric lightcurve including the window function are shown.

3 Doppler imaging

The spectral resolution of R = 55,000 combined with the $v \sin i$ of just ≈ 20 km s^{-1} and the relative faintness of the star for a 1.2-m telescope, places XX Tri close to the limit for Doppler imaging. Significant effort is thus put to denoise the line profiles and to prepare the data for the inversion.

In this chapter we give an overview of the basics and procedures of Doppler imaging in general (Kopf 2008), as well as a description of our code *iMap* in detail (Carroll et al. 2012). Furthermore, we describe the data reduction and denoising of the spectral line profiles used in the inversion process. We explain, which data is used for each Doppler map, and how we proceed with larger gaps in our time-series. In order to analyze all Doppler maps for spot evolution, we present a spot-modeling procedure based on a Monte-Carlo approach. Finally, we present all Doppler maps and their corresponding spot-models.

3.1 Methodology

Doppler imaging enables the reconstruction of a temperature or abundance surface distribution of a rotating star. The idea of stellar surface mapping was introduced by Deutsch (1958) and is based on rotationally broadened line profiles. The determination of the surface distribution was presented as an inverse problem when it was formulated as an integral equation by Khokhlova (1976). A method to solve this equation numerically was given by Goncharskii et al. (1977).

Principles

Inhomogeneities on a stellar surface, such as temperature or abundance variations, leave characteristic distortions in rotationally broadened line profiles. The line and continuum intensities originating from a spotted region are partly suppressed, relative to the non-spotted regions. Thus, in the normalized absorption profile, a "bump" appears at a Doppler shift which corresponds to the longitudinal position of the spot. Fig. 3.1 illustrates this correlation between the spot position on the stellar surface and the wavelength (or velocity) position in the corresponding line profile.

In the case of observing many spectra at different rotation phases during a full rotation period, one can derive a more precise position of the spot, as the behavior of the bump with time sets additional constrains to the latitudinal position of the spot. If a spot appears close to the visible pole, its impact on most of the profiles stays close to the line center. In contrary, a spot near the stellar equator is only visible in about half of the rotation period, moving all the way from the blue to the red wing. Thus, a complete two-dimensional surface map can be reconstructed by taking a time-series of line profiles during a full stellar rotation.

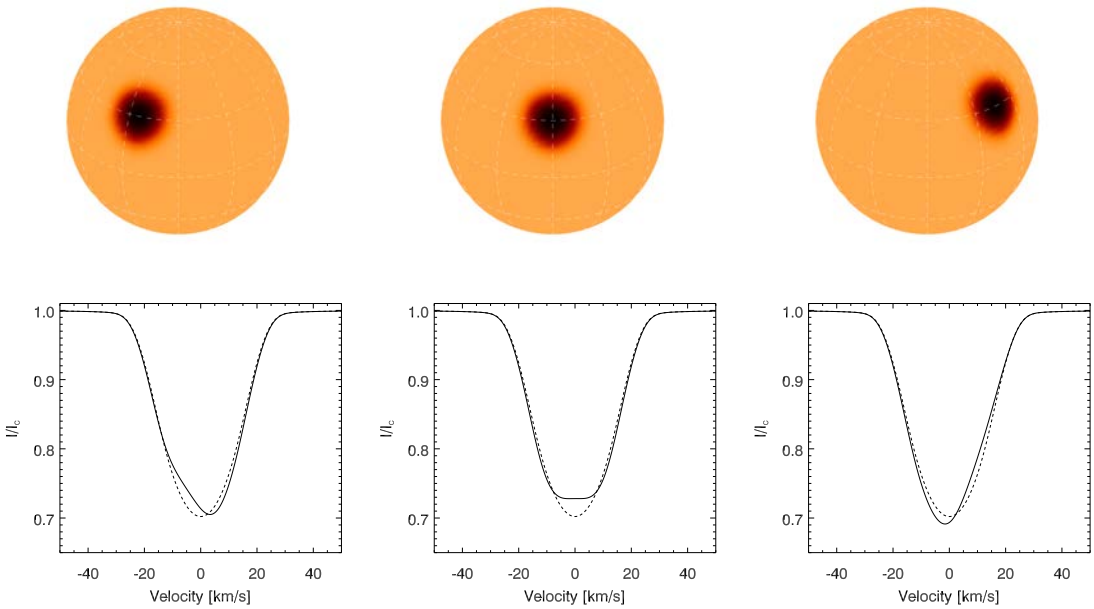

Figure 3.1: Illustration of the principle of Doppler imaging. The (fast) rotation of a star causes a significant broadening of spectral lines through the Doppler shift. The presence of a spot causes perturbations in the line shape (*solid curves*), in comparison to a featureless surface (*dashed curves*). Such perturbations move from the left to the right wing of the line as the spot moves across the visible hemisphere due to the rotation of the star. As the rotational velocities, and therefore Doppler shifts, are greatest in low-latitude regions of the star, a spot near the equator produces a perturbation that migrates from the extreme left wing to the extreme right wing. Spots at higher latitude exhibit smaller Doppler shifts and thus produce perturbations that begin and end closer to the line center. In this way, time-resolved spectra can be used to construct a map of the spot distributions on the surface of the star.

We note that, if the rotational axis coincides with the line-of-sight (LOS; $i = 0°$), there is no resulting LOS velocity and therefore no DI possible. On the other hand, if $i = 90°$, one can not distinguish between the northern and southern hemisphere. Thus, it is obvious that the inclination should be at some intermediate stage. Furthermore, we note that the considered star has to be a fast rotator to ensure that the rotational broadening dominates the natural line broadening. Therefore, the projected equatorial rotation velocity, $v \sin i$, should be at least 15 $\mathrm{km\,s^{-1}}$. On the other hand, with increasing rotational velocity the line profile becomes shallower because of the conservation of line equivalent width. Thus, above 100 $\mathrm{km\,s^{-1}}$ the spot detection out of the noise gets complicated.

Inversion

The Doppler imaging technique basically solves an inverse problem. In general, inverse problems aim to deduce model parameters from observed data. Thus, an inverse problem represents the counterpart of a forward problem, as illustrated in

Fig. 3.2. In our case the forward problem is the line profile synthesis involving the disk integration of local intensity profiles, computed by radiative transfer calculations (see Chap. 3.2).

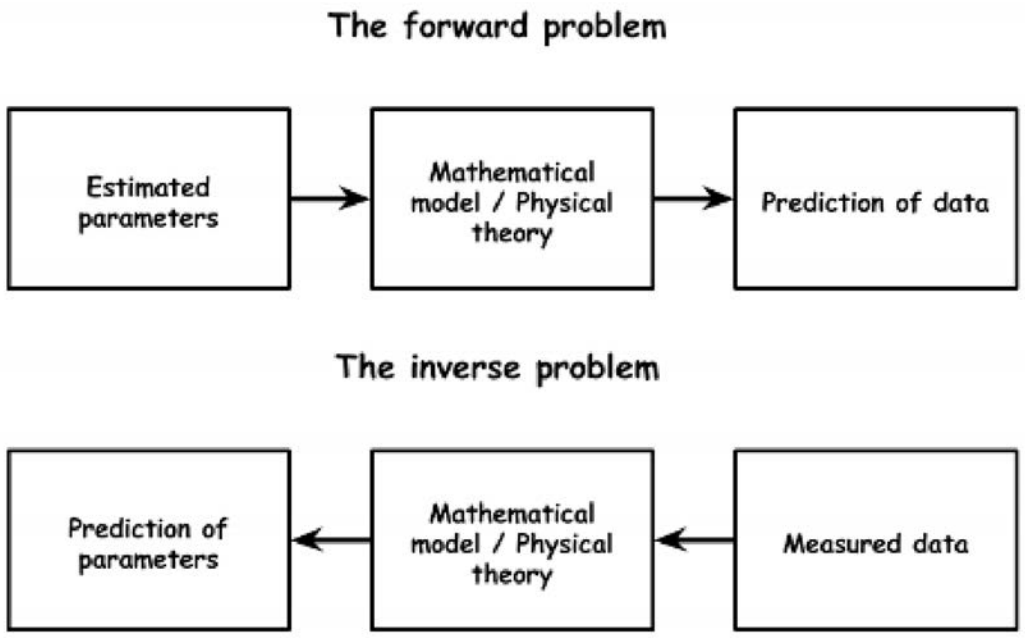

Figure 3.2: Illustration of an inverse problem. The forward problem is mainly concerned with the problem of prediction, in the sense that given all background knowledge of the problem (mathematical model and parameters) and initial conditions one can predict the solution over time or space. The inverse problem on the other hand is concerned with the problem of recovering information, in the sense that given only some background knowledge of the problem (mathematical model, but not all parameters) and some data observed, one wants to recover the missing information that carries the solution and with it important physical properties that cannot be directly observed. (Taken from https://cmontalto.wordpress.com/2013/03/08/what-are-inverse-problems/.)

Inverse problems are differentiated between linear and non-linear ones. A linear inverse problem is the inverse of a linear forward system, which can be written in a discretized form as $d = \mathsf{A}m$. The matrix A maps the model parameters m to the data d. In the non-linear case, the forward system is expressed by $d = A(m)$, where A is a non-linear functional depending on the model parameters m. Thus, it can not be considered as a simple linear matrix multiplication. As the radiative transfer calculation is a non-linear system, DI represents a non-linear inverse problem. Thus, the functional A can not be simply inverted to derive the model parameters m from the data d. Typically such inverse problems are solved numerically using an iterative method.

Concerning stellar surface mapping, the inverse problem is solved as follows: Starting from an initial surface distribution, disk-integrated intensity profiles are synthesized and compared with the observed line profiles in terms of a discrepancy

function. An optimization algorithm iteratively minimize the discrepancy function

$$E(\boldsymbol{x}) = \sum_{\phi} \sum_{\lambda} \frac{[R^{\mathrm{obs}}_{\lambda,\phi}(\boldsymbol{x}) - R^{\mathrm{syn}}_{\lambda,\phi}(\boldsymbol{x})]^2}{\sigma^2_{\lambda,\phi}} \ , \tag{3.1}$$

by adjusting the free parameters $\boldsymbol{x} = (x_1, \ldots, x_n)$ (temperature or abundance of each surface segment). The first sum runs over all rotation phases ϕ and the second sum runs over all wavelengths λ. $R^{\mathrm{obs}}_{\lambda,\phi}$ and $R^{\mathrm{syn}}_{\lambda,\phi}$ are observed and synthesized intensity profiles respectively and $\sigma^2_{\lambda,\phi}$ are variances, corresponding to the observations.

Regularization

According to Hadamard (1902), a problem is called well-posed, if: (i) a solution exists; (ii) the solution is unique; (iii) the solution depends continuously on the data. If one of these requirements is not fulfilled, it is called ill-posed, which typically is inherent to inverse problems. As small changes in the data can result in large changes in the solution, a well-posed problem can still be ill-conditioned. This implies that the continuous dependence of the solution on the data does not necessarily mean that the solution is robust against noise.

As DI is typically ill-posed and ill-conditioned an additional information in the form of a regularization term Λf is imposed. This term is added to the sum of squared error in the discrepancy function in Eq. (3.1), so the total error function becomes

$$E = \chi^2 + \Lambda f \ , \tag{3.2}$$

where the regularization parameter $\Lambda > 0$ weights the regularization function f. Because of the presence of noise in real observations, the role of regularization is to stabilize the inversion and prevent it from fitting noise. Tikhonov (1963) and Maximum Entropy (Frieden 1972) are the commonly used regularization functions in Doppler imaging.

Before we discuss the regularization functional, the commonly used optimization algorithm is presented. The conjugate gradient method assumes that the error function $E(\boldsymbol{x})$ with its free parameters $\boldsymbol{x}$ is quadratic close to the minimum. Therefore, the error function can be expressed as a Taylor series:

$$E(\boldsymbol{x}) \approx E_0 - \boldsymbol{b}^{\mathsf{T}}\boldsymbol{x} + \frac{1}{2}\boldsymbol{x}^{\mathsf{T}}\mathsf{H}\boldsymbol{x} \ , \tag{3.3}$$

where $\boldsymbol{b}$ is a constant vector and H is a matrix, assumed to be positive definite. The gradient of E is

$$\boldsymbol{g} = \nabla E = \mathsf{H}\boldsymbol{x} - \boldsymbol{b} \ , \tag{3.4}$$

so the error function finds its minimum at $\mathsf{H}\boldsymbol{x} = \boldsymbol{b}$. For further details of the derivation we refer to Press et al. (1992).

Again, the two major problems of stellar surface imaging are the ill-posedness of the non-linear inverse problem and the ill-conditioning due to noisy data. Thus, it is likely that several local minima in the multi-dimensional parameter space exist, in which the iterative minimization algorithm might end up. This problem is dedicated to a regularization functional, such as the Tikhonov and Maximum Entropy method.

A good introduction into the theory of Maximum Entropy can be found in Narayan & Nityananda (1986). The purpose of the Maximum Entropy method is to reconstruct the most probable non-negative image that is consistent with the data. The entropy functional typically used in DI on its basic form is given by:

$$f(x) = -x \ln x \ . \tag{3.5}$$

It becomes clear that, when maximizing Eq. (3.5) or minimizing its negative, the function finds its maximum or minimum at $x_0 = e^{-1}$, respectively.

The Tikhonov regularization implies a strong correlation between neighboring surface elements. Its functional has the form:

$$f = \sum_i \|\nabla x_i\|^2 \ , \tag{3.6}$$

where x_i are the surface parameters, with the index i running over all surface elements. It aims for the smoothest possible solution that is (within the error limits) in agreement with the data (Piskunov et al. 1990). In contrast to Maximum Entropy, the Tikhonov functional is also defined for negative parameter values. Thus, in the case of ZDI, no special care has to be taken for negative polarity, when the free parameters are constituted by magnetic field components.

3.2 Radiative transfer

The description of what happens to the specific intensity I_ν of light as it propagates through a media is given by the equation of radiative transfer. The radiative transfer equation (RTE) is a key equation for the study of stellar structure (e.g. Rutten 2003). By combining the effects of emission and absorption the RTE is given by:

$$\frac{dI_\nu}{ds} = -\kappa_\nu I_\nu + j_\nu \ , \tag{3.7}$$

where κ and j are the absorption and emission coefficient, respectively. Both coefficients include effects of photon scattering. Using the optical depth, defined as $d\tau_\nu \equiv \kappa_\nu ds$, one can rewrite the RTE (Eq. 3.7) as:

$$\frac{dI_\nu}{d\tau_\nu} = -I_\nu + S_\nu \ , \tag{3.8}$$

where $S_\nu \equiv j_\nu/\kappa_\nu$ is called the source function. Equation 3.8 tells us how specific intensity varies as light travels through a medium.

A formal solution for I_ν at the surface of a plane-parallel slab with optical depth τ_1 is given by:

$$I_\nu = I_\nu(\tau_1)e^{-\tau_1} + \int_0^{\tau_1} S_\nu(t)e^{-t}dt \ . \tag{3.9}$$

Assuming local thermodynamic equilibrium (LTE), the source function is identical with the Planck function:

$$S_\nu = B_\nu(T) = \frac{2h\nu^3}{c^2}(e^{h\nu/kT} - 1)^{-1} \ . \tag{3.10}$$

We note that within our line profile inversion, we solve the RTE through a model atmosphere under the assumption of LTE, see Chapter 3.3 for a description of our inversion code.

The light we observe from a star, appearing as a point-like source, can be represented as the integral of local intensity profiles emerging from each point $M(\eta, \rho)$ on the visible hemisphere, where η and ρ are the longitude and latitude, respectively. The individual local spectra are shifted in wavelength due to the Doppler effect $\Delta\lambda_D$, so the residual intensity can be written as:

$$R_{syn}(\lambda) = \frac{\iint I_l[M, \theta, \lambda + \Delta\lambda_D] \cos\theta \, dM}{\iint I_c[M, \theta] \cos\theta \, dM} \, , \tag{3.11}$$

where I_c is the continuum intensity and I_l is the local line intensity.

3.3 DI-code iMap

All surface temperature maps in this study were computed with our Doppler imaging (DI) and Zeeman-Doppler imaging (ZDI) code *iMap* (Carroll et al. 2007, 2008, 2009, 2012). The code performs a multi-line inversion of a large number of photospheric line profiles simultaneously. For the local line profile calculation, the code utilizes a full (polarized) radiative transfer solver (Carroll et al. 2008).

The atomic line parameters are taken from the VALD database (Kupka et al. 1999). We used Kurucz model atmospheres (Castelli & Kurucz 2004) which are interpolated for each desired temperature, gravity and metallicity during the course of the inversion. Additional input parameters are the projected rotational velocity $v \sin i$, as well as micro- and macroturbulence.

For all temperature maps, the surface segmentation is set to a $5° \times 5°$ equal-degree partition, resulting in 2592 segments. Due to the inclination of 60° a total of 432 segments are hidden and therefore only 2160 segments are included during the inversion process.

The code calculates the full radiative transfer of all involved line profiles for each surface segment depending on the current effective temperature and atmospheric model. The surface temperature of each segment is adjusted according to the local (temperature) gradient information and the line profile discrepancy is reduced until a minimum χ^2 is obtained.

In the following we give a brief description of the code, for further information see Carroll et al. (2012):

The *iMap* code is equipped with a new inversion module. While the former versions relied on a conjugate gradient method (Press et al. 1992) with a local entropy regularization (Carroll et al. 2007), the current version of *iMap* uses an iteratively regularized Landweber method (Engl et al. 1996). Iterative regularization for inverse problems has been the subject of various theoretical investigations over the recent years (Hanke 1997; Engl & Kügler 2005; Egger & Neubauer 2005; Kaltenbacher et al. 2008).

The Landweber iteration, which is used here, rests on the idea of a simple fixed-point iteration, derived from minimizing the sum of the squared errors. Our new inversion routine follows exactly this line and can be described as follows:

Written in a concise vector notation the problem setting is

$$\min_{\vec{x}} \frac{1}{2}\|\vec{I}(\vec{x}) - \vec{O}\|^2 \ , \tag{3.12}$$

where $\|\|$ is the L_2 norm and $\vec{I}$ is the synthetic model profile over all spectral lines, wavelengths or velocities, and rotational phases, $\vec{O}$ is the corresponding observation. The vector $\vec{x}$ contains all our free parameters of the model, i.e. the temperature for each surface element. The iteration now proceeds along the negative gradient direction and updates the current estimate of the solution vector, $\vec{x}_k$, in the following manner

$$\vec{x}_{k+1} \ = \ \vec{x}_k + w_k \vec{I}'(\vec{x}_k) \left(\vec{O} - \vec{I}(\vec{x}_k)\right) \ . \tag{3.13}$$

Here, $\vec{I}'$ is the gradient vector with respect to all surface element values and w_k is the weight factor that can adaptively accelerate the iteration process. In the conventional Landweber iteration process, w_k is set to unity. To accelerate the procedure we use a variant of the steepest descent (Kaltenbacher et al. 2008) and set w_k to

$$w_k \ = \ \frac{\|u_k\|^2}{\|\vec{I}'(\vec{x}_k)u_k\|^2} \ , \tag{3.14}$$

where $u_k = \vec{I}' * (\vec{O} - \vec{I}(\vec{x}_k))$.

The semi-convergence (Hanke et al. 1995) of the method requires a stopping rule before it enters into the noise level of the data to regularize the procedure and to avoid overfitting. One common, and well studied criterion for the stopping condition is the Morozov discrepancy principle which can be written for the iterative approach as

$$\|\vec{I}(\vec{x}_{k^*}) - \vec{O}\| \ \leq \ \tau\delta < \ \|\vec{I}(\vec{x}_k) - \vec{O}\| \ ; \ 0 \leq k < k^* \ , \tag{3.15}$$

where δ is an upper bound for the data error (i.e. noise), τ a positive number and k^* the maximum iteration number. In terms of stability and convergence it can be shown that τ has to satisfy $\tau \geq 1$ (Engl et al. 1996). Formally the noise estimate for the DI/ZDI can be derived from the observations. Given a noise contribution σ_i for each velocity i we can combine the individual errors to form a vector $\vec{\sigma}$ such as, $\vec{\sigma}^T = (\sigma_1, \sigma_2, ..., \sigma_n)$ with n the number of velocity points. The error can then be expressed as $\delta = \|\vec{\sigma}\|$. If the noise estimate is homogeneous (i.e. equal for all velocities) or does not vary much over the velocity domain and time we may use the maximum of $\vec{\sigma}$ to write for δ the relation

$$\delta = \max(\vec{\sigma})\sqrt{n} \ . \tag{3.16}$$

If we assume that Eq. (3.12) follows a χ^2 distribution we may use the number of degrees-of-freedom of the problem to determine the error resulting from the limited degree of freedom of the model to write

$$\delta = \max(\vec{\sigma})\sqrt{n - p} \ , \tag{3.17}$$

where p is the number of parameters in the model. If the inversion reduces the error function Eq. (3.12) down to the threshold δ we would ensure that the reduced χ^2 is close to one.

Table 3.1: Spectral lines used in the inversion process.

Ion	λ (Å)	Ion	λ (Å)	Ion	λ (Å)
Fe I	5049.820	Fe I	5434.524	Fe I	6219.281
Cu I	5105.537	Fe I	5445.042	Fe I	6254.258
Fe I	5198.711	Fe I	5497.516	Fe I	6265.132
Fe I	5232.940	Fe I	5501.465	Fe I	6322.685
Fe I	5302.300	Fe I	5506.779	Fe I	6393.600
Fe I	5307.361	Fe I	5569.618	Fe I	6408.018
Fe I	5324.179	Fe I	5576.089	Fe I	6411.648
Cr I	5345.796	Ca I	5581.965	Fe I	6421.350
Cr I	5348.315	Ca I	5601.277	Fe I	6430.845
Fe I	5367.466	Fe I	6020.169	Ca I	6439.075
Fe I	5383.369	Fe I	6024.058	Ca I	6717.681
Fe I	5393.167	Fe I	6065.482	Fe I	6750.152
Mn I	5394.677	Ca I	6122.217		
Mn I	5420.355	Fe I	6173.334		

3.4 Spectral line selection and denoising

We included 40 well-defined absorption lines simultaneously in our inversion, which are listed in Table 3.1. These lines were chosen individually by investigating the stellar spectra and VALD database and several other criteria such as having a minimum line depth of 0.75 I/I_C, being almost blend-free, and having a good continuum stratification above 0.9 I/I_C. Additionally, all blends within ± 1 Å of each extracted line profile and a minimum line depth of 0.1 are included in the inversion.

To estimate the reliability of the linelist as well as their sufficiency we simply tested two subgroups of the linelist and compare their reconstructed maps with the original map where all lines from Table 3.1 are included in the inversion process. Both linelists of the subgroups consist of 20 lines from Table 3.1, including line #1-20 and line #21-40, respectively. Their resulting maps and difference to the original map are shown in Fig. 3.3. We see, that both maps are almost identical with each other and with the original map. The reconstructed spot distribution, in terms of spot area, spot temperature, as well as spot position is consistent. Therefore, we suggest that our used linelist is whether to short nor to selective. We further verified this method on a few other Doppler images with the same result (not shown).

As we have to deal with relatively low S/N ratios, a wavelet analysis based on the *à trous*-algorithm (Starck et al. 1998, chapter 1.4.4 and references therein) is implemented for further denoising. Starck et al. (1997) showed that for noisy data the wavelet transform is a powerful signal processing technique for spectral analysis. Each line profile (in our case the mean profile out of the 40 individual lines) is split into so-called wavelet scales w_j and a smoothed array c_p, whereas their sum represents the original spectrum $c_0(\lambda) = c_p(\lambda) + \sum_{j=1}^{p} w_j(\lambda)$. For each wavelet scale the standard deviation is determined and only signals above $3\,\sigma$ are overtaken in the recomposition of the spectral line.

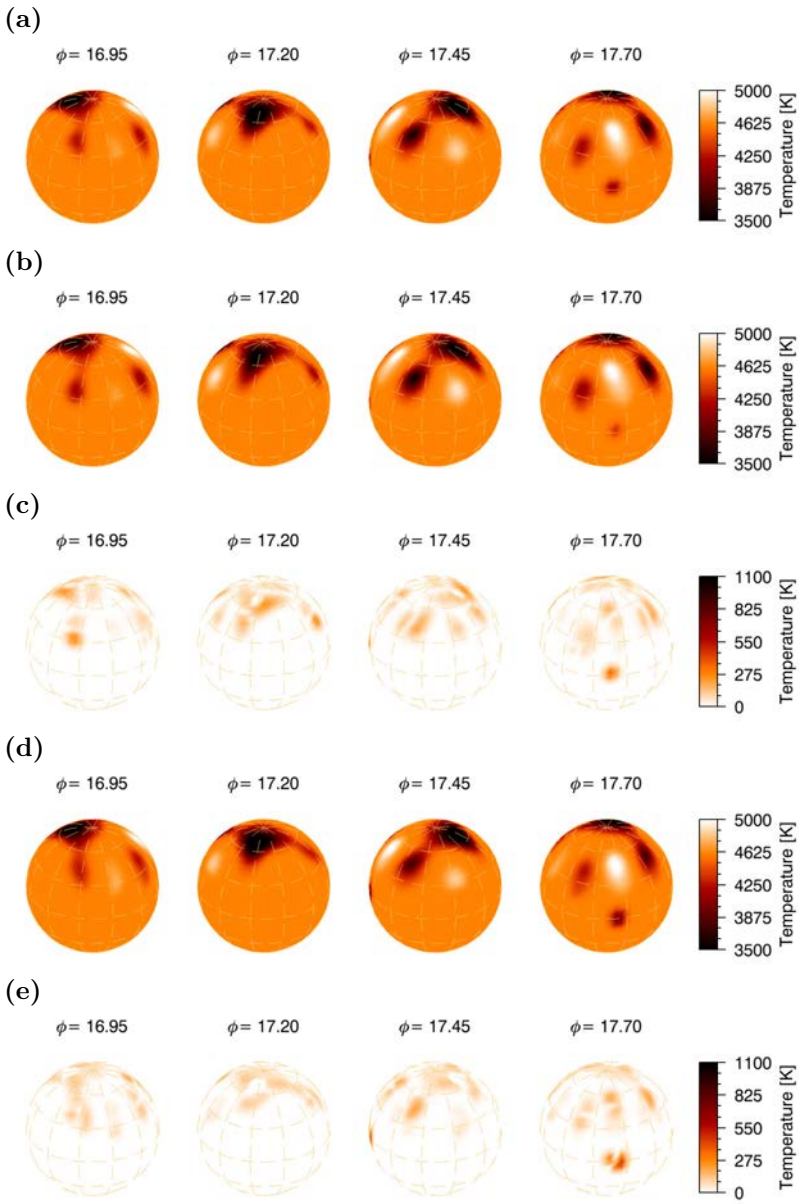

Figure 3.3: Test of the influence of line selection in terms of spot recovery. Each Doppler image is shown in four spherical projections 90° apart. a) Input map. This Doppler image is identical to the first reconstruction from season 2007/08 using a total of 40 lines. b) The reconstructed map when implementing only 20 lines (#1-20) from Table 3.1 in the inversion process. c) The (absolute) difference $a - b$. d) The reconstructed map when implementing only 20 lines (#21-40) from Table 3.1 in the inversion process. e) The (absolute) difference $a - d$.

3.5 Phase selection and gap filling

In order to later quantify the continuous evolution of spots based on consecutive Doppler maps, we first deal with the inherent limitations of our phase coverage. In certain circumstances it is difficult to compare consecutive maps that had different phase coverage and that even contained some larger observational gaps (several

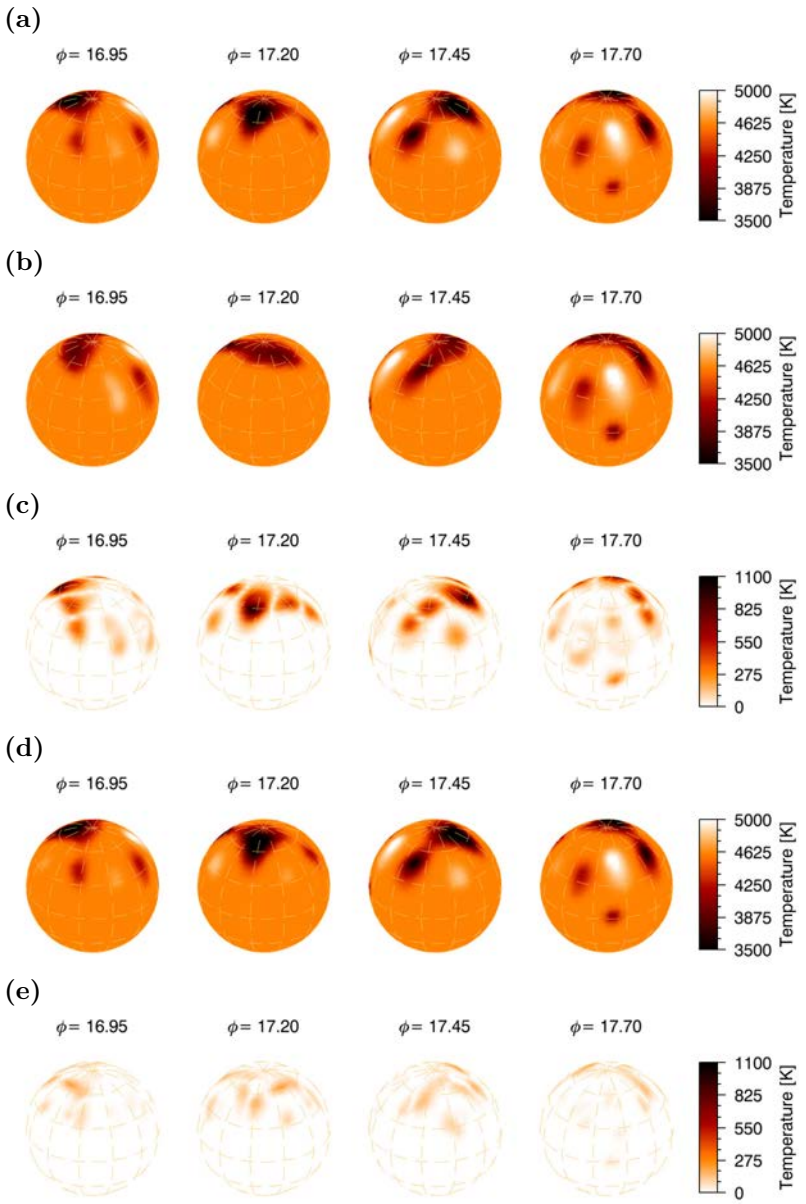

Figure 3.4: Test #1 of the influence of phase gaps and filled gaps in terms of spot recovery. Each Doppler image is shown in four spherical projections 90° apart. a) Input map. This Doppler image is identical to the first reconstruction from season 2007/08 with a total of 21 phases. b) The reconstructed map when ignoring phases no. 4-9 in the inversion process. c) The (absolute) difference $a - b$. d) The reconstructed map when the phase gap is filled with phases from the following stellar rotation. e) The (absolute) difference $a - d$.

tenths of a phase) at different rotational phases at different times. The effect of phase gaps on the recovery of individual spots had been simulated by many authors in the past (e.g. Rice & Strassmeier 2000, and references therein). Generally, Doppler imaging is very robust against small phase gaps but large phase gaps may introduce spurious spots at surface locations not covered by the data.

Fig. 3.4 and 3.5 show our simulations with *iMap* based on real data of XX Tri.

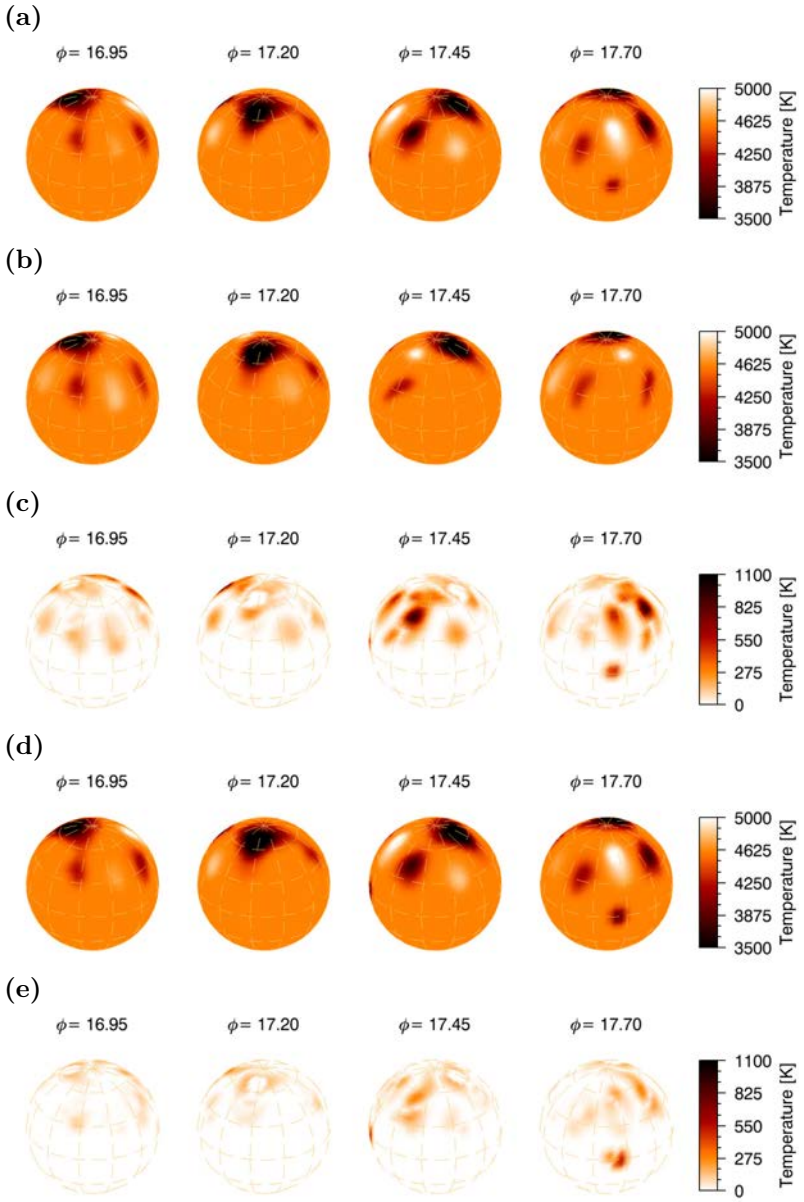

Figure 3.5: Test #2 of the influence of phase gaps and filled gaps in terms of spot recovery. Each Doppler image is shown in four spherical projections 90° apart. a) Input map. This Doppler image is identical to the first reconstruction from season 2007/08 with a total of 21 phases. b) The reconstructed map when ignoring phases no. 10-15 in the inversion process. c) The (absolute) difference $a - b$. d) The reconstructed map when the phase gap is filled with phases from the following stellar rotation. e) The (absolute) difference $a - d$.

During the season 2007/08, STELLA has covered two consecutive stellar rotations completely with one observation per night (DI #8 from 2007.67 and DI #9 from 2007.73 amounting to 21 phases from 23 nights per rotation). From DI #8, we removed six consecutive phases to create an artificial phase gap of 90° ($0^{\mathrm{p}}25$), and compared the resulting map with the original one (Fig. 3.4a-c). The two darkest and biggest spots at phases around $17^{\mathrm{p}}25$ and $17^{\mathrm{p}}55$ could not be separated anymore.

The larger spot looses a big part of its area, which is seen in the difference map in Fig. 3.4c with a temperature similar to the difference between photospheric and spot temperature. In the next step, we filled these gaps with observations from the following stellar rotation (DI #9) and again compared the resulting map with the original one (Fig. 3.4d-e). All individual spots are now reconstructed with no changes of their size or temperature exceeding the expected errors driven by the S/N of the data. Fig. 3.5a-c shows another simulation of the same data with an artificial phase gap of 90° but at a different rotational phase. Here, the smaller spot at phase around 17ᵖ55 has almost completely vanished, whereas it is recovered for the case with gap filling (Fig. 3.5d-e). We further verified this method on a few other Doppler images with the same result (not shown).

We conclude that large phase gaps of ≈ 90° have a strong impact on the recovery of the global stellar spot distribution. In addition, it affects not only their size and shape but also their location. For smaller spots located within or near the missing phases it even might affect their existence. However, when we compare the original map with the maps where the missing phases were filled by phases from one rotation earlier or later, we see a significantly better agreement. This is the case even if the spot distribution had evolved in the meantime. Based on these simulations, we have a simple method to minimize the systematics due to phase gaps. We note that this is only a first-order approximation because the spot evolution within the missing surface area remains unknown. Fig. 3.6 shows the phase coverage and gap filling (if useful and applicable) of each Doppler image for all seasons. Real phase gaps range between 1-13 d or 0ᵖ04-0ᵖ54 at the extremes, but with typical values close to ≈ 4 d or 0ᵖ17.

For two out of all 36 Doppler images, we had to use phases from two rotations earlier and/or later, as there were no observations closer in time available. In the first case (DI #5) we filled a gap of 5 d (0ᵖ21) with two phases. In order to minimize a possible smearing effect one phase was taken from two rotations earlier and one from two rotations later. In the case of DI #20, we had in addition to deal with a small number of existing phases. Because of this initial situation, we should not have taken this rotation into account. But then we would have only four maps for the observing season 2007/08, two consecutive maps at the beginning and two consecutive maps at the end of the season, which would have severely limited our coverage for this season. We explicitly rediscuss this in Sect. 4.2 in terms of spot-area evolution.

Table 3.2 summarizes our Doppler-image log. The year indicates the mid time of the Doppler image, followed by its Heliocentric Julian Date (HJD) range, the time Δt elapsed in days, the number of spectra N, the largest phase gap in number of consecutive days (the rotation period is 24 d), and the number of observations from following or preceding stellar rotations that were used to fill phase gaps. In total, 36 individual Doppler images were obtained, each with between 11 to 24 spectra.

3.6 Image analysis: definition of the spot area

One parameter to be extracted from each image is the surface area of a spot. Its measurement depends on the definition where a spot ends and where the undisturbed photosphere begins. Our inversion code is completely unconstrained in terms of spot

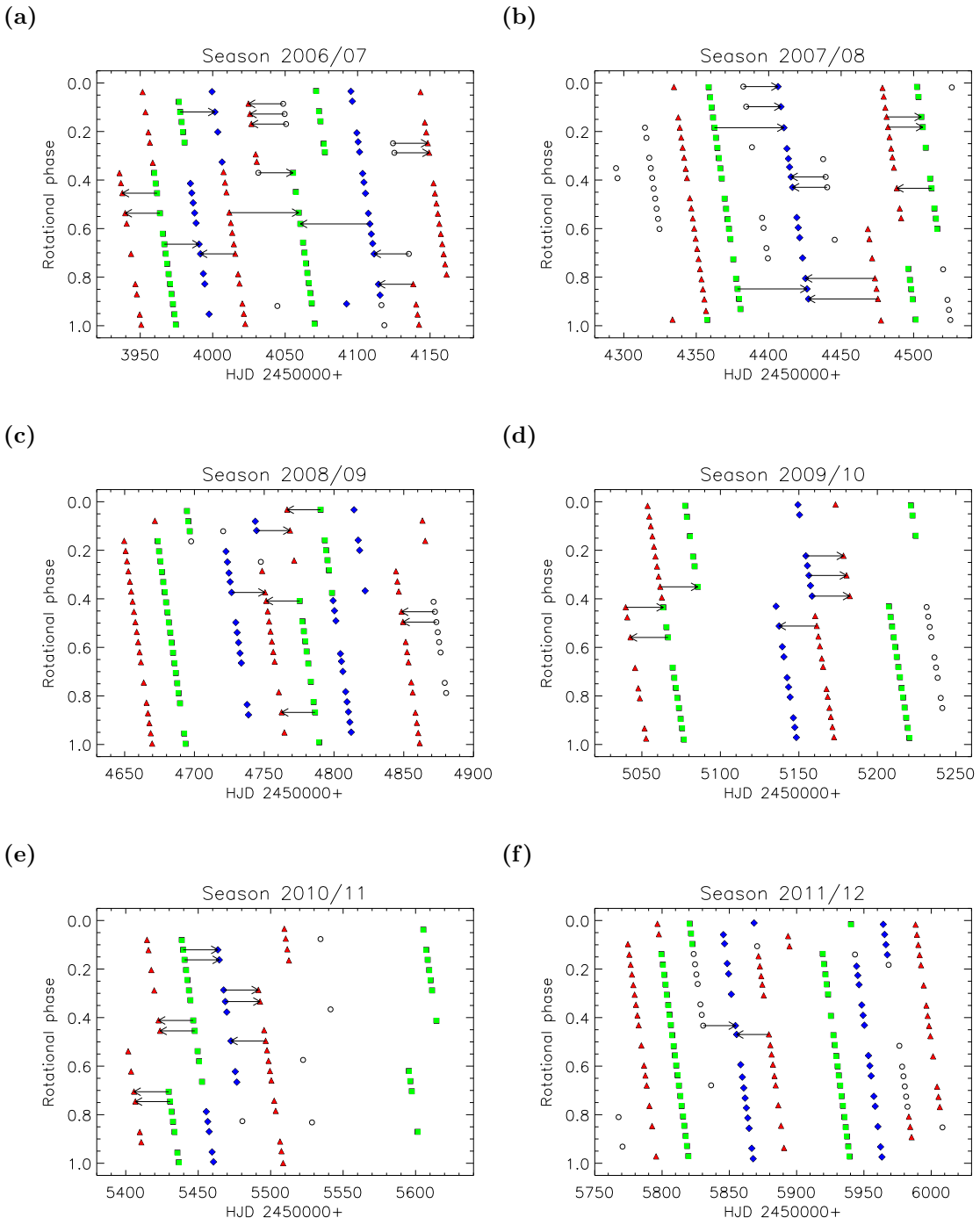

Figure 3.6: Phase coverage of Doppler images from 2006 to 2012. Different filled (colored) symbols represents the phases of each individual Doppler image, whereas not-filled circles represents non-used spectra (except for gap filling). The arrows indicate the spectra which were used to fill up large observational gaps. Detailed information is given in Table 3.2.

reconstruction and usually recovers an irregular spot morphology. Furthermore, several images contain small-scale structures which seem to appear or disappear from one rotation to another. These structures often show up as hot spots or as a pair of a hot and a cool spot (but not necessarily along the same isoradial line which

would indicate an artifact). The appearance of elongated appendages to the polar spot, or spots that seem to be connected to another spot, are further complications for determining a the area of a spot. Due to inherent limitations of the spatial surface resolution because of the low $v \sin i$, as well as to a lesser extent also because of the choice of regularization during the inversion, such spot configurations can not be easily separated from each other anymore. Thus, simple area integration of the disk within a certain temperature difference would have its limits.

So far, various methods of spot-area determination are practiced, depending on the stellar surface reconstruction method. In Doppler imaging a common method is to set an arbitrary threshold to the spot temperature (e.g., Hackman et al. 2012). This method is surely sufficient in order to estimate the spot occupancy in general, but it is definitely questionable in terms of determining spot decay/formation rates. A more profound method was used by Roettenbacher et al. (2013). At first, they visually identified each spot group in the surface map. Then, they determined the latitude and longitude for each spot group by finding the centroid of each spot, defined by drawing a circle on the reconstructed stellar surface enclosing the spot and finding the "center of mass" of the patches therein. The "mass" of a patch was defined as the difference between its intensity and the average surface intensity.

We define the area of a spot by fitting artificial spot-models to the maps. Our artificial spots have circular shapes of arbitrary size but a constant temperature of $T_{\mathrm{spot}} = 3500$ K. From photometric spot-modeling with spot temperature as free parameter the derived temperature difference $\Delta T = T_{\mathrm{phot}} - T_{\mathrm{spot}}$ were determined to 1100 K (Strassmeier & Olah 1992) and 1280 K (Eker 1995) as well as in the range of 650-1200 K (Hampton et al. 1996) for various epochs. Furthermore, the superspot on the first Doppler image had a temperature difference of $\Delta T = 1300$ K (Strassmeier 1999). These values are in agreement with the derived spot temperatures of ≈ 3500 K from our Doppler images for the long-lived spot structures, which result in $\Delta T = T_{\mathrm{phot}} - T_{\mathrm{spot}} \approx 1100$ K. As our focus lies in the evolution of starspots, i.e. their decay or growth, we investigate mainly the large-scale spot structures that are repeatedly reconstructed from one stellar rotation to the next.

Our method is based on the spot-modeling procedure used in light-curve analysis (e.g., Ribárik et al. 2003), where an appropriate number of spots with circular shape and a defined temperature is taken as input. An initial guess of the spot's location and radius was taken directly from the observed Doppler images. With these starting values, we calculated the best fit with an area- and temperature-weighted Monte-Carlo (MC) method and thus extracted a definition-dependent, best-effort, spot location and area. Within the three-parameter space (longitude, latitude, radius) 10,000 random positions were generated, using a range of 15° for each parameter, and then cross correlated with the original Doppler map. From the best 100 correlation maps (which corresponds to $\sqrt{N}$), the mean values and their standard deviations are determined.

The area of the individual spots from the spot-model fits is summarized in Table 3.2 in units of Solar Hemispheres (SH). To estimate the quality of the spot-model fit, we compared the total spotted area between the spot-model and the Doppler image. To determine the total spotted area of the Doppler image a temperature weighting by analogy to the MC method was used. We obtain the total spotted area such that each spotted segment i attributes a certain fraction of its area a_i to

the total spotted area dependent on its temperature given by

$$A_{\rm total} = \sum_i a_i \frac{(T_{\rm eff} - T_i)}{(\Delta T)_{\rm max}} \ , \tag{3.18}$$

where $(\Delta T)_{\rm max} = (T_{\rm phot} - T_{\rm spot})_{\rm max} = 1120$ K. We note that the small-scale surface structures, cool and hot spots, were not counted into the total spotted area. The quality of the spot-model fits is given in Table 3.2 in terms of the uncertainty of the spot-models, where all our spot-models lie within $1\,\sigma$. The absolute scale of the area units in m^2 is set by the stellar radius of 10.9 $R_\odot$. Formally, the stellar surface of XX Tri is 724 Gm^2 and thus 118.8 times the surface of the Sun or 1 SH $\approx 0.8\,\%$ of an hemisphere of XX Tri.

3.7 Resulting Doppler images and spot models

We obtained a total of 36 Doppler images between 2006-2012, including 5-7 almost consecutive maps for each observational season. The whole Doppler "movie" is presented in Fig. 3.7, where each map represents a single Doppler image.

We like to mention that there are several other attempts to monitor active stars by means of Doppler imaging. For example, for the rapidly rotating single late-type giant FK Comae, a series of snapshots consisting of 25 Doppler maps between 1993-2003 exists, see Korhonen et al. (2007). The RS CVn binary II Peg was monitored by Berdyugina et al. (1998, 1999) between 1992-1999 resulting in 15 Doppler maps. These maps were partially re-analyzed by Lindborg et al. (2011) including six new maps. Hackman et al. (2012) added 12 more Doppler maps, resulting in a total of 28 Doppler maps for II Peg between 1994-2010. IM Peg, another RS CVn binary, was monitored by Berdyugina et al. (2000) who obtained 8 Doppler maps between 1996-1999. Marsden et al. (2007) obtained a movie from 31 Doppler maps for IM Peg during a monitoring campaign between 2004-2007. Another starspot movie was published earlier for HR 1099 (V711 Tau) from 37 Doppler maps taken in 1996 (Strassmeier & Bartus 2000).

Comparing our new Doppler images with the first map of XX Tri (see Fig. 2.1), published by Strassmeier (1999), shows a very good agreement of spot locations and spot temperatures, despite the $\approx$ 10-year time difference. In both cases large cool spots together with small cool/hot spots are recovered. Whereas the larger spots appear near the pole with a temperature of around 3500 K, the smaller cool/hot spots appear on lower latitudes, again with comparable temperature differences. The super spot from 1998 with an area of approximately 11 % of the entire stellar surface is much larger than the largest recovered spots presented in our new imagery. This is expected because the star appeared to be in its brightest stage ever in 2009. In parallel, the rotationally-modulated photometric light curves show a small amplitude compared to that in 1998. During the season 1998/99 a record amplitude of $\approx 0\overset{\rm m}{.}6$ in V was observed in comparison to an amplitude of $< 0\overset{\rm m}{.}4$ during the seasons from 2006/07 to 2011/12, see Fig. 2.2.

In Table 3.2 the maximum and mean surface temperature of each individual Doppler image is given. Furthermore, Table 3.2 lists the fit quality between ob-

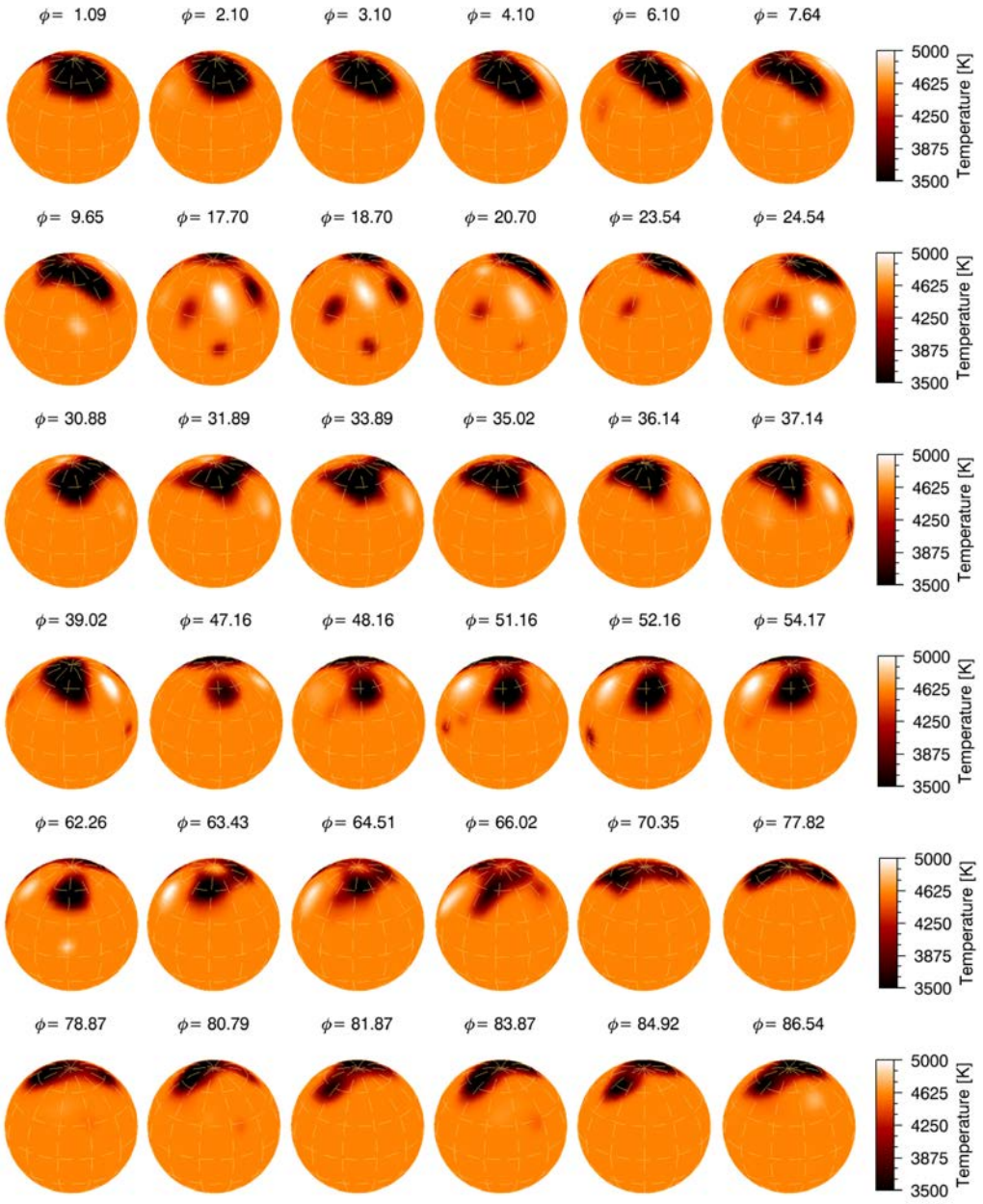

Figure 3.7: Doppler "movie" of XX Tri between 2006-2012. Each map represents a single Doppler image. All 36 maps are shown at the same rotational phase towards the companion star. The time-difference between each map is given in units of rotational phase ϕ.

served ($x_{i,O}$) and calculated ($x_{i,C}$) profiles,

$$RMS = \sqrt{\frac{1}{n}\sum_{i=1}^{n}(x_{i,O} - x_{i,C})^2} \ , \tag{3.19}$$

where n is the total number of points of all line profiles used during the inversion process. The observed and inverted line profiles of each Doppler image are shown in Fig. 3.8-3.13.

Table 3.2: Doppler image log, fit quality, surface temperature and spot areas.

DI	Year	HJD range	Δt	N	ϕ-gap	N-fill[a]	RMS[b]	Sigma[c]	Temperature (K)		Spot area (SH)[d]					
#		(2450000+)	(d)		(d)			($\sigma_{\rm spot}$)	$T_{\rm max}$	$T_{\rm mean}$	Spot A	Spot B	Spot C	Spot D	Spot E	Spot Total
1	2006.58	3935-3963	28	15	4	2	0.0048	0.6	4667	4470	9.2 ± 0.3	1.1 ± 0.6	1.3 ± 0.8	—	—	11.5 ± 1.0
2	2006.64	3959-3980	21	19	3	0	0.0046	0.6	4731	4477	8.5 ± 0.5	1.5 ± 0.5	1.2 ± 0.7	—	—	11.2 ± 0.9
3	2006.71	3966-4015	49	14	5	3	0.0047	0.7	4796	4489	8.1 ± 0.6	2.1 ± 0.6	1.6 ± 0.9	—	—	11.8 ± 1.0
4	2006.78	4007-4050	43	18	7	3	0.0047	0.7	4961	4476	7.2 ± 0.7	2.6 ± 0.5	2.4 ± 0.7	—	—	12.2 ± 0.8
5	2006.91	4011-4108	97[e]	17	5	3	0.0047	0.8	5059	4477	6.0 ± 0.5	3.3 ± 0.5	3.0 ± 1.1	—	—	12.3 ± 1.1
6	2007.01	4092-4138	46	16	5	2	0.0044	0.5	5052	4492	5.4 ± 0.6	3.7 ± 0.6	3.1 ± 1.2	—	—	12.2 ± 1.3
7	2007.14	4124-4161	37	19	5	2	0.0043	0.7	5125	4486	5.4 ± 0.7	3.9 ± 0.6	3.2 ± 1.1	—	—	12.5 ± 1.3
8	2007.67	4333-4356	23	21	3	0	0.0040	0.4	5129	4541	5.5 ± 0.5	1.6 ± 0.4	—	—	—	7.1 ± 0.8
9	2007.73	4357-4380	23	21	2	0	0.0035	0.4	5027	4537	5.2 ± 0.4	1.8 ± 0.7	—	—	—	7.0 ± 0.9
10	2007.87	4362-4475	113[e]	15	13	8	0.0033	0.7	4912	4538	4.1 ± 0.7	2.6 ± 0.3	—	—	—	6.7 ± 0.7
11	2008.05	4468-4512	44	19	4	1	0.0037	0.6	4685	4534	4.3 ± 0.7	2.5 ± 0.4	—	—	—	6.8 ± 0.7
12	2008.12	4481-4516	35	15	5	2	0.0038	0.6	5188	4524	4.1 ± 0.5	2.6 ± 0.5	—	—	—	6.6 ± 0.4
13	2008.53	4649-4671	22	20	2	0	0.0040	0.5	4903	4503	4.8 ± 0.2	3.2 ± 0.3	—	—	—	8.0 ± 0.4
14	2008.60	4673-4696	23	22	3	0	0.0037	0.5	4839	4501	5.5 ± 0.3	3.0 ± 0.4	—	—	—	8.5 ± 0.5
15	2008.73	4722-4744	22	14	5	0	0.0038	0.7	4845	4501	6.4 ± 0.4	2.0 ± 0.2	—	—	—	8.4 ± 0.4
16	2008.80	4726-4790	64	15	7	5	0.0034	0.5	4745	4497	7.5 ± 0.5	1.6 ± 0.4	—	—	—	9.1 ± 0.6
17	2008.88	4775-4798	23	16	3	0	0.0035	0.4	5057	4503	8.0 ± 0.7	0.7 ± 0.2	—	—	—	8.7 ± 0.8
18	2008.94	4799-4822	23	15	4	0	0.0032	0.3	5004	4508	8.1 ± 0.6	0.6 ± 0.3	—	—	—	8.8 ± 0.7
19	2009.07	4844-4873	29	16	5	2	0.0035	0.9	5193	4493	8.2 ± 0.4	1.2 ± 0.3	—	—	—	9.4 ± 0.5
20	2009.60	5039-5066	27	18	5	1	0.0033	0.3	4918	4522	7.8 ± 1.2	2.9 ± 0.4	—	—	—	10.7 ± 1.3
21	2009.67	5039-5083	44	17	6	2	0.0035	0.7	4825	4500	8.1 ± 1.0	3.3 ± 0.4	—	—	—	11.3 ± 1.1
22	2009.86	5135-5161	26	17	4	1	0.0039	0.9	5061	4495	8.3 ± 1.1	4.7 ± 0.5	—	—	—	13.0 ± 1.1
23	2009.93	5154-5173	19	16	11	3	0.0036	0.4	5001	4511	7.4 ± 1.1	4.8 ± 0.3	—	—	—	12.2 ± 1.1
24	2010.06	5207-5224	17	17	7	0	0.0035	0.6	5146	4506	6.8 ± 0.7	4.9 ± 0.6	—	—	—	11.6 ± 1.0
25	2010.59	5401-5447	46	12	6	4	0.0029	0.6	4935	4535	4.5 ± 0.7	3.3 ± 0.3	0.9 ± 0.6	—	—	8.7 ± 0.9
26	2010.67	5429-5452	23	19	2	0	0.0031	0.4	5088	4538	4.0 ± 0.7	3.1 ± 0.4	1.1 ± 0.6	—	—	8.1 ± 0.9
27	2010.74	5439-5496	57	13	7	3	0.0029	0.9	4967	4532	3.2 ± 0.4	2.4 ± 0.6	1.5 ± 0.7	—	—	7.2 ± 0.9
28	2010.84	5467-5512	45	17	7	2	0.0030	0.9	4943	4522	2.6 ± 0.4	1.5 ± 0.6	2.4 ± 0.6	—	—	6.5 ± 0.7
29	2011.12	5595-5614	19	11	5	0	0.0021	0.5	4620	4513	—	—	—	5.1 ± 0.5	2.3 ± 0.4	7.4 ± 0.5
30	2011.61	5774-5797	23	18	3	0	0.0033	0.3	4758	4493	4.7 ± 0.6	2.9 ± 0.4	1.2 ± 0.6	—	—	8.8 ± 0.7
31	2011.68	5799-5822	23	24	1	0	0.0032	0.4	4756	4501	4.5 ± 0.7	2.5 ± 0.8	1.7 ± 0.6	—	—	8.8 ± 0.8
32	2011.81	5830-5879	49	17	7	2	0.0029	0.8	4649	4509	3.7 ± 0.7	1.4 ± 0.7	3.1 ± 0.4	—	—	8.2 ± 1.0
33	2011.88	5871-5894	23	16	4	0	0.0025	0.9	4722	4501	3.0 ± 0.5	2.7 ± 0.8	3.4 ± 0.3	—	—	9.1 ± 0.8
34	2012.01	5919-5940	21	20	3	0	0.0027	0.4	4664	4486	3.6 ± 0.7	3.4 ± 0.9	2.6 ± 0.4	—	—	9.6 ± 1.0
35	2012.08	5944-5967	23	18	3	0	0.0026	0.7	4620	4506	3.3 ± 0.7	4.2 ± 0.9	1.7 ± 0.4	—	—	9.2 ± 1.1
36	2012.19	5983-6006	23	17	3	0	0.0031	0.3	4767	4477	3.6 ± 0.7	5.8 ± 0.6	0.6 ± 0.4	—	—	10.0 ± 0.8

Notes. [a] Number of phases/observations borrowed from the following and/or preceding stellar rotation. [b] RMS-error between observed and calculated profiles. [c] Deviation of spot area between spot-models and Doppler image in terms of the standard deviation of the total spotted area. [d] In units of Solar Hemispheres (1 SH = 3.05 $\rm Gm^2$). [e] Including phases/observations from two stellar rotations earlier and/or later.

Season 2006/07

For the observing season 2006/07, we reconstruct seven consecutive Doppler images, covering around nine rotations. All maps are shown in Fig. 3.14. They show a large polar spot with an absolute temperature of ≈ 3500 K. During the season, the polar spot drifted apart and changed its morphology from almost circular to an elongated spot form. This drift could be a sign of differential rotation, see Chapter 4.4. Furthermore, a smaller high-latitude spot with a temperature of around 3800 K is reconstructed. It is seen that the larger spot approaches the smaller spot. We note again that due to the inherent technical limitations of Doppler imaging the surface resolution near the rotational pole is poor and thus spot separations are not well constrained. Therefore, one can not say whether the large spot is a monolithic structure or a conglomerate of several smaller spots. Beside the polar spot, scattered small cool and/or hot spots are visible at latitudes between 0-60° with absolute temperatures between 4200 to 5000 K.

In Fig. 3.15 the best spot-model fits for observing season 2006/07 are shown. Three artificial spots were sufficient to reach a high correlation for all Doppler maps in this season. Two spots were utilized to represent the large polar spot and to model its drift during almost ten stellar rotations. The third spot represents the smaller high-latitude spot on the opposite hemisphere. All other cool and/or hot spots at lower latitudes with no or only very short continuous appearance are ignored and therefore not implemented in the spot-model analysis.

Season 2007/08

In Fig. 3.16 five consecutive Doppler images are shown, obtained for the observing season 2007/08, covering around eight rotations. During the first three rotations, we observe the merging of the two larger spots ($T_{\rm spot} \approx 3500$ K), located around the longitude of 180°, see surface maps at phases ϕ of 17.45, 18.45, and 20.45, respectively. While the larger one appears close to the pole, the smaller one is located at mid-latitudes. Differential rotation could be the cause of the spot merging. Again, we refer to Section 4.4, where we analyze the differential rotation for all maps. Beside these two spots several smaller cool and/or hot spots are located at latitudes between 0-60° and appear mostly irregular from map to map.

In Fig. 3.17 the corresponding spot-model fits of the Doppler images in Fig. 3.16 are shown. For the observing season 2007/08, we concentrate on the two larger spots interacting with each other, as they are regularly visible.

Season 2008/09

All obtained Doppler images for the observing season 2008/09 are shown in Fig. 3.18, covering around nine rotations. In the first map, two apparently merged large polar spots are recovered with absolute temperatures of ≈ 3500 K. During the first three rotations this conglomeration fragments, while the smaller spot component shrinks in area size, and the larger spot increases. This spot evolution lasts for the next few rotations. As in the previous seasons, several scattered cool and/or hot spots are recovered irregularly. They appear at latitudes between 0-60° with absolute temperatures between 4200 to 5000 K.

In Fig. 3.19 the spot-model fits of the Doppler images for the observing season 2008/09 are shown. As for the previous season, we concentrate on the two larger spots interacting with each other, because they are regularly visible.

Season 2009/10

Fig. 3.20 shows five consecutive Doppler images, obtained for the observing season 2009/10, covering around eight rotations. Two large polar spots are reconstructed with absolute temperatures of ≈ 3500 K. They are located at opposite hemispheres with a longitudinal shift of around 180°. Both large spots show variations in area size during the observed timespan of eight rotations. Again, several scattered cool and/or hot spots are recovered irregularly, appearing at latitudes between 0-60° with absolute temperatures between 4200 to 5000 K.

In Fig. 3.21 the spot-model fits of the Doppler images in Fig. 3.20 are shown. Both large spots near the pole are modeled. Again, small cool and/or hot spots with irregular appearance are ignored.

Season 2010/11

For the observing season 2010/11, we reconstruct five consecutive Doppler images, which are shown in Fig. 3.22, covering around nine rotations. Three spots are visible close to the pole with absolute temperatures around 3500 K. The two larger spots seem to lose in area size, whereas the smaller spot increases. In the last map only two large spots are visible, located at opposite hemispheres with a longitudinal shift of around 180°. Because of a preceding observational gap of around four rotation periods, the evolution from three to two spot components is not resolved. Beside the large spots several smaller cool and/or hot spots appear mostly irregular from map to map, located at latitudes between 0-60° with absolute temperatures between 4200 to 5000 K.

In Fig. 3.23 the corresponding spot-model fits are shown. Whereas for the first four maps three spots are used to model the spotted surface, only two spots are sufficient in the last map. All small cool and/or hot spots with irregular appearance are ignored.

Season 2011/12

In Fig. 3.24 seven almost consecutive Doppler images for the observing season 2011/12 are shown, which cover around ten rotations. The first map looks very similar to the last one of the previous season, showing two large polar spots on opposite hemispheres with a longitudinal shift of around 180° and absolute temperatures of ≈ 3500 K. In contrary to the observational season 2009/10, both spots show an interaction and a longitudinal drift. During this season, some smaller cool and/or hot spots appear irregular from map to map, located at latitudes between 0-60° with absolute temperatures between 4200 to 5000 K.

In order to illustrate the interaction between both polar spots, three spots are needed to model the spot evolution. Fig. 3.25 shows the spot-model fits of the Doppler images for the observing season 2011/12. Again, weak spots with irregular appearance are ignored.

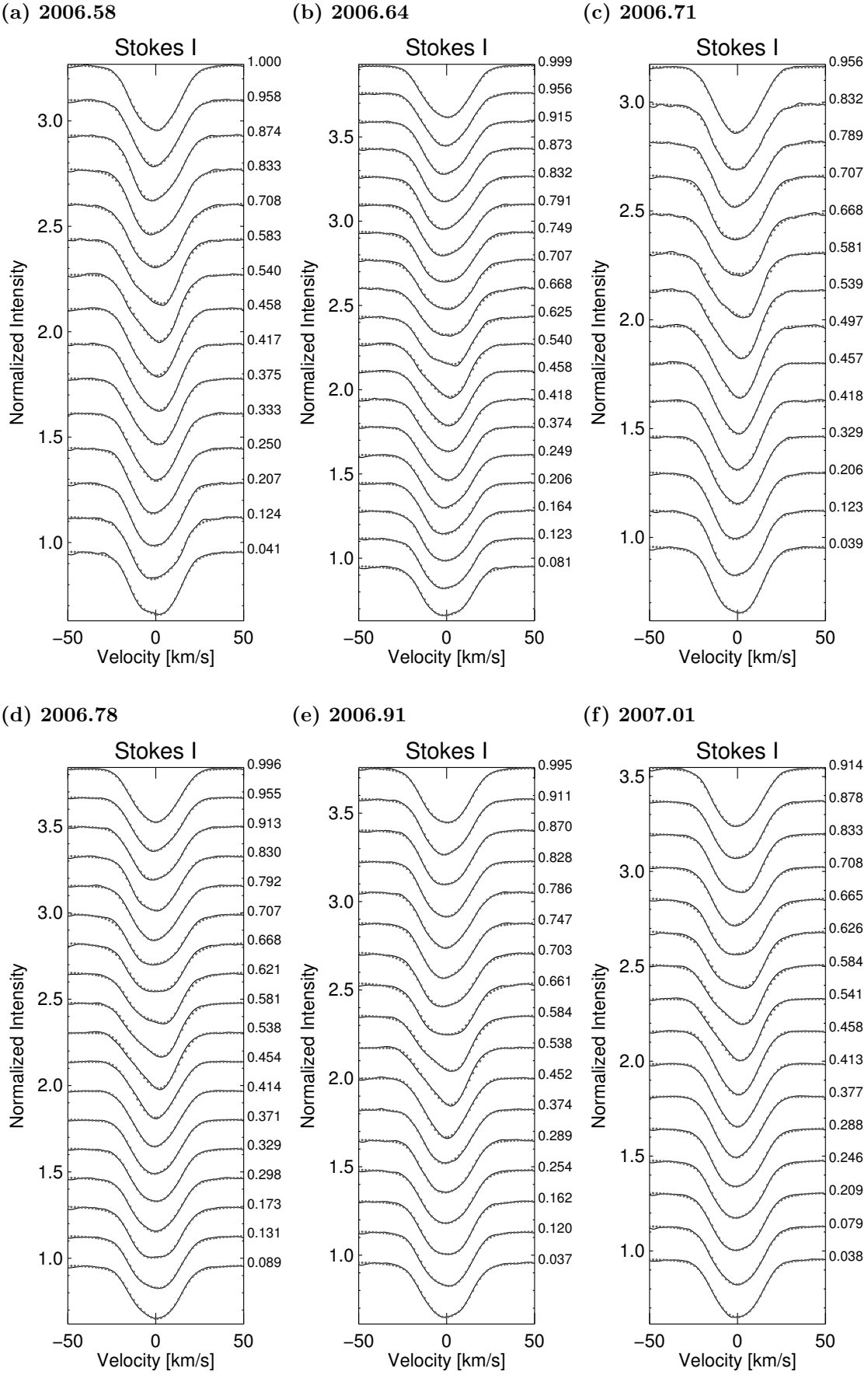

Figure 3.8: Line profiles of DI #1-6. Each figure shows the observed (solid lines) and inverted (dotted lines) line profiles for one DI stating their mid times and the respective phases. Rotation advances from bottom to the top.

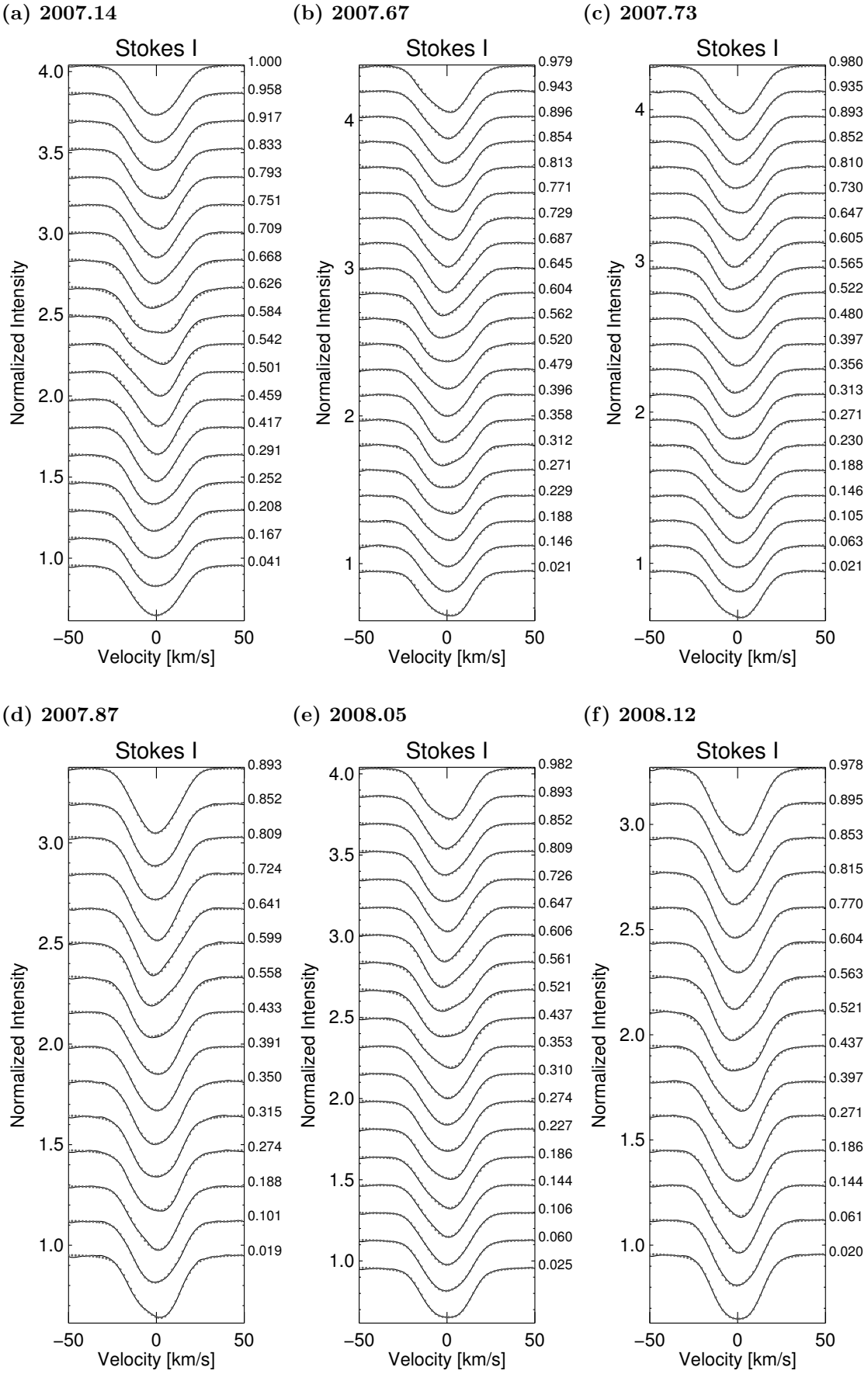

Figure 3.9: Line profiles of Doppler images #7-12. Otherwise as in Fig. 3.8.

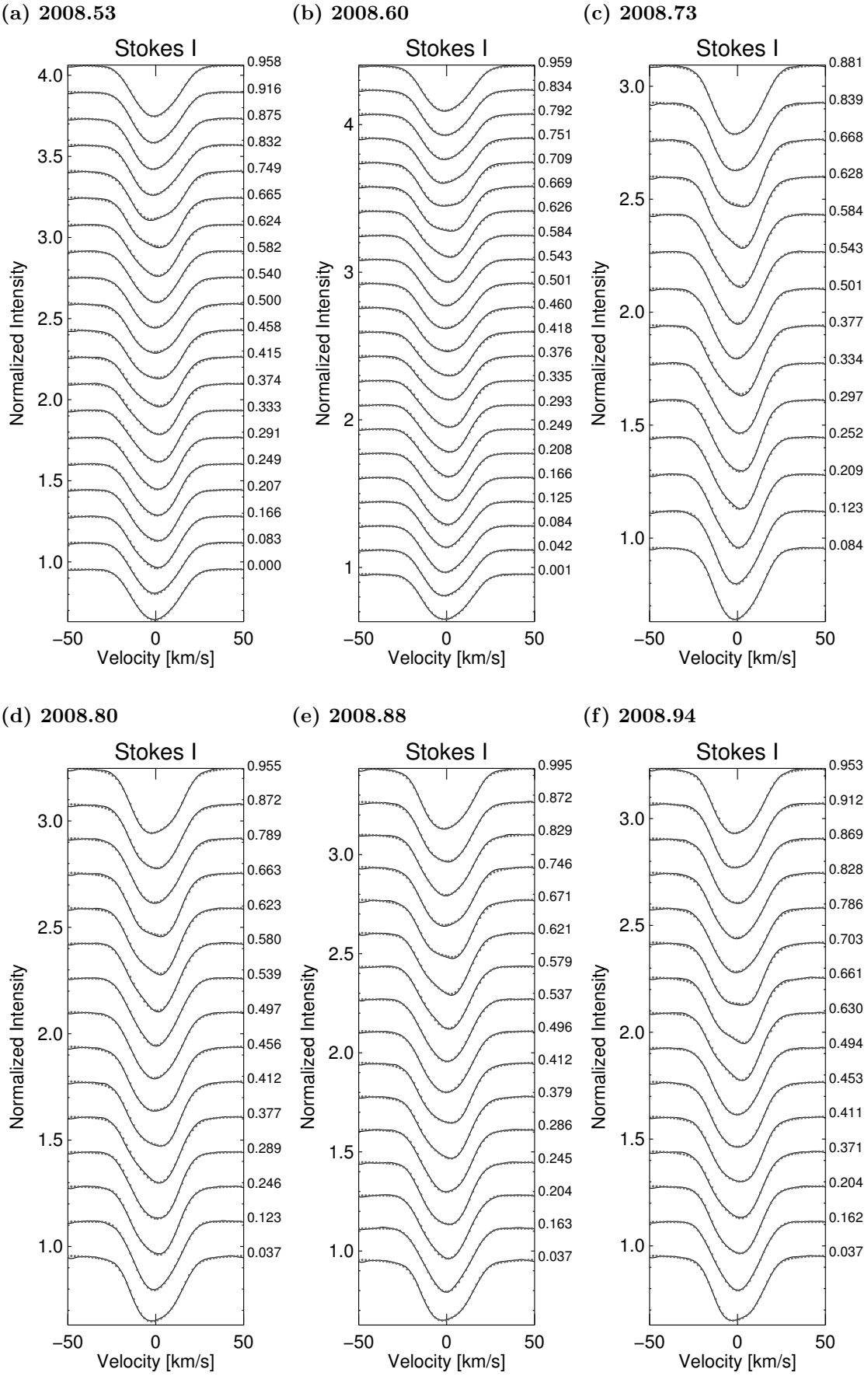

Figure 3.10: Line profiles of Doppler images #13-18. Otherwise as in Fig. 3.8.

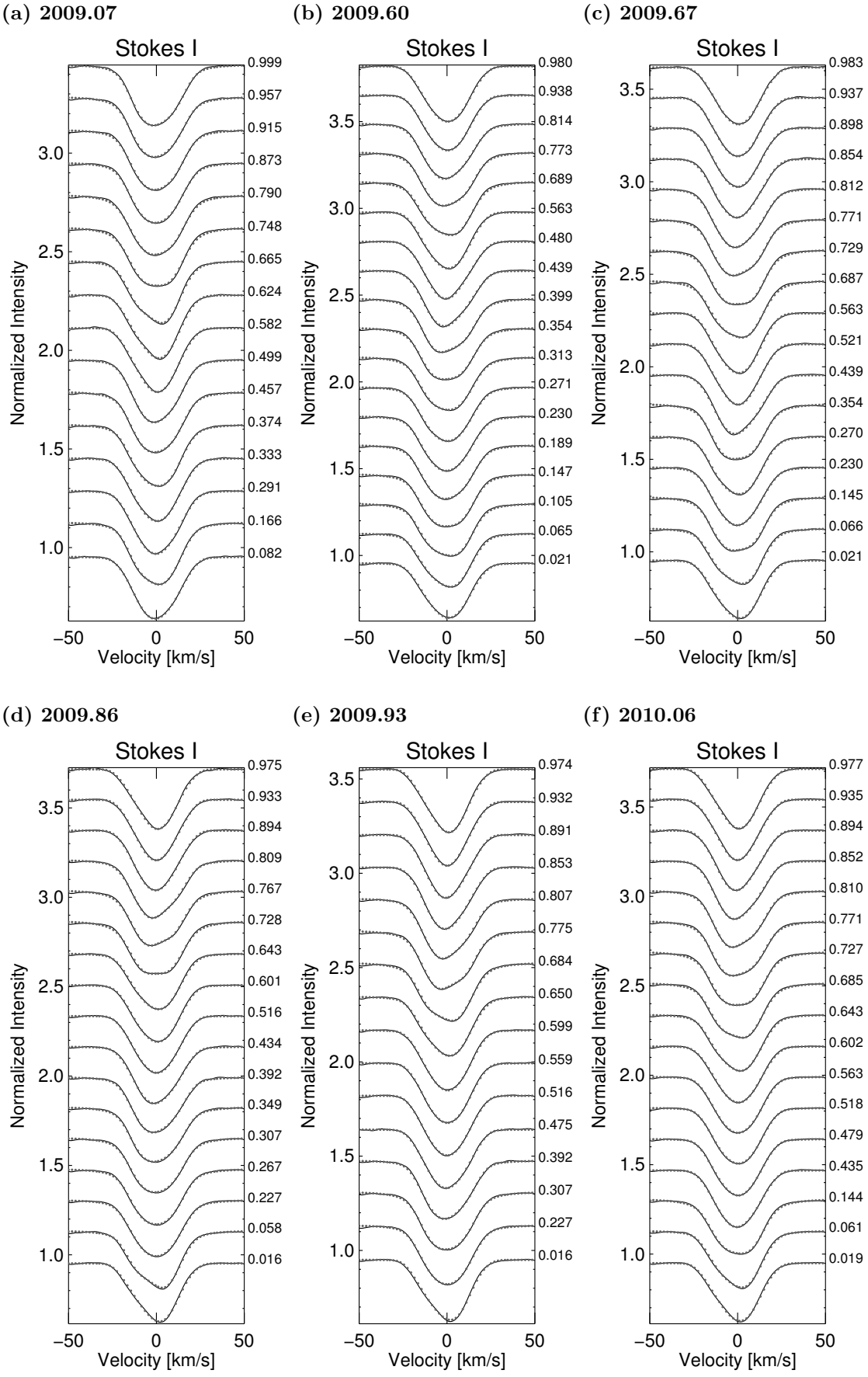

Figure 3.11: Line profiles of Doppler images #19-24. Otherwise as in Fig. 3.8.

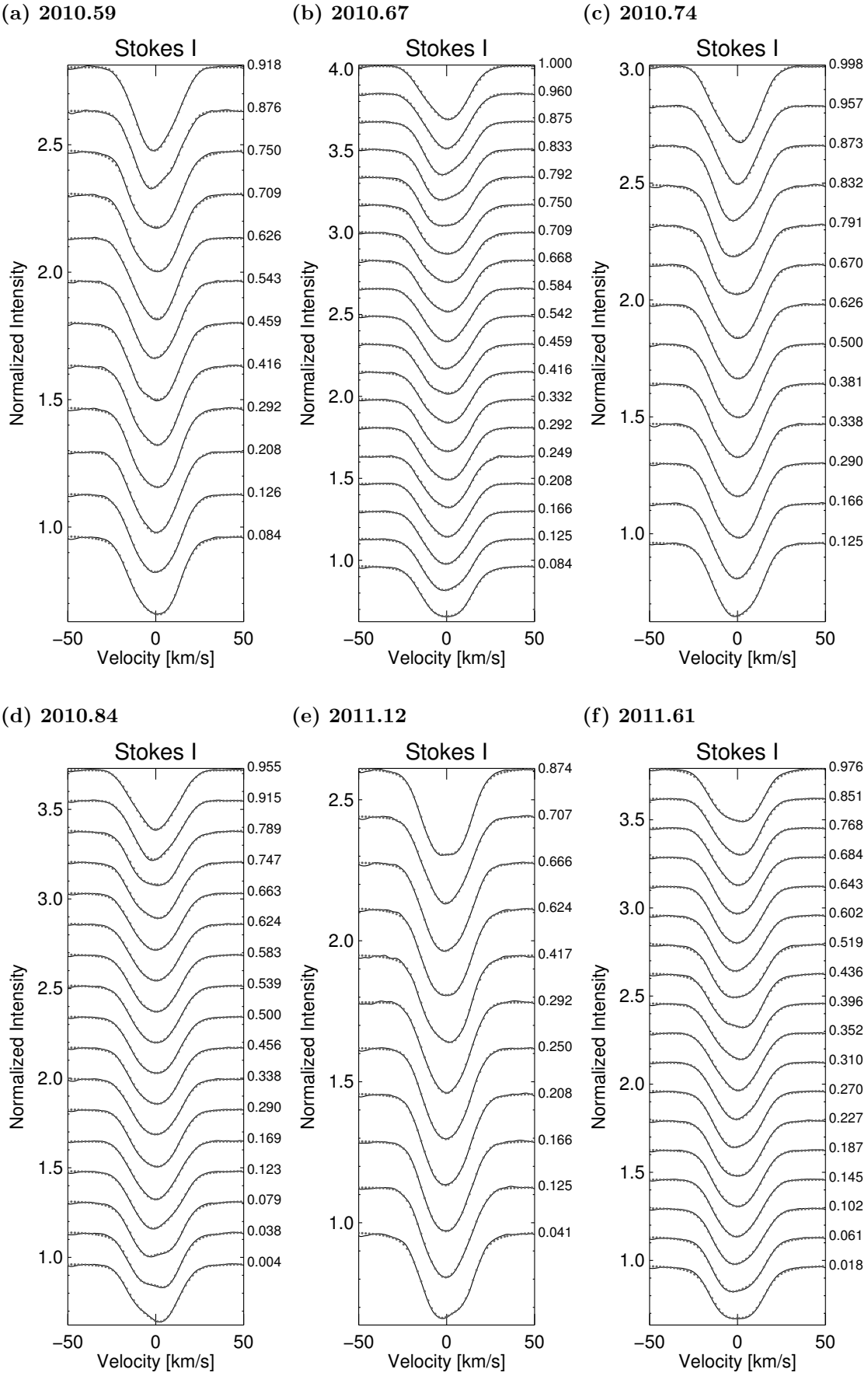

Figure 3.12: Line profiles of Doppler images #25-30. Otherwise as in Fig. 3.8.

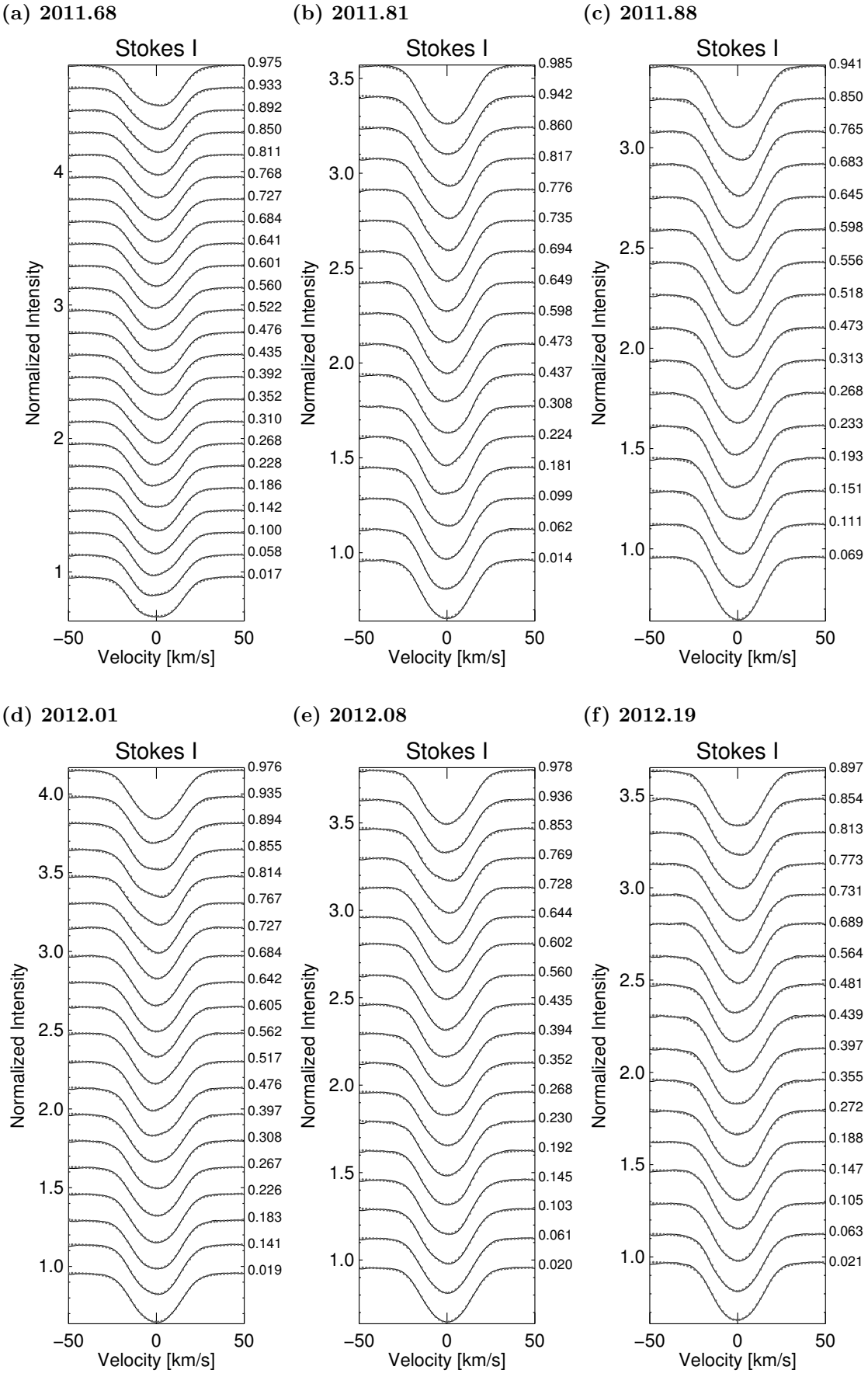

Figure 3.13: Line profiles of Doppler images #31-36. Otherwise as in Fig. 3.8.

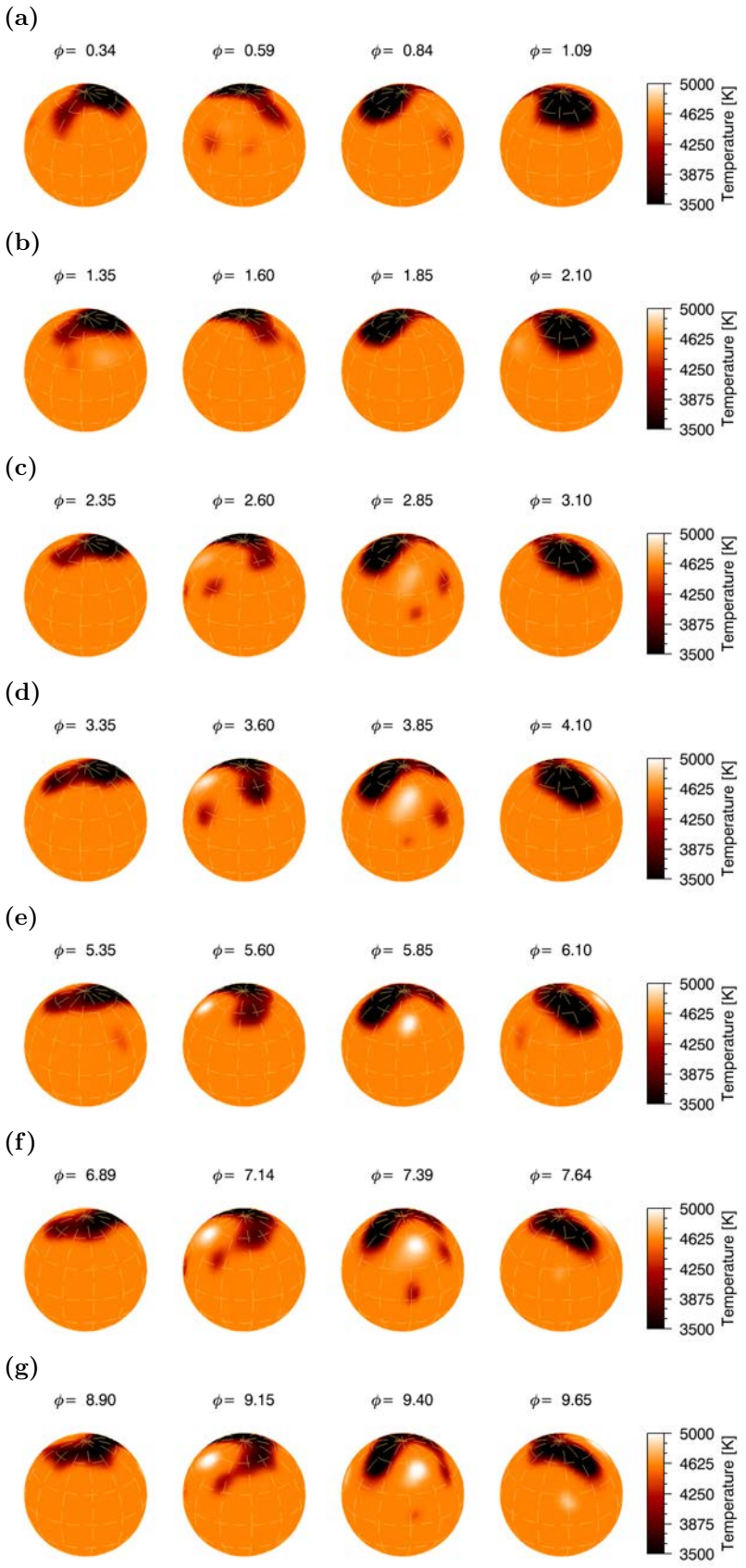

Figure 3.14: Doppler images of XX Tri for the observing season 2006/07. Each map is shown in four spherical projections, every 90°. The rotational shift between each image is corrected, i.e. the stellar orientation remains the same from map to map and from season to season. The time-difference between each image is given in units of rotational phase ϕ.

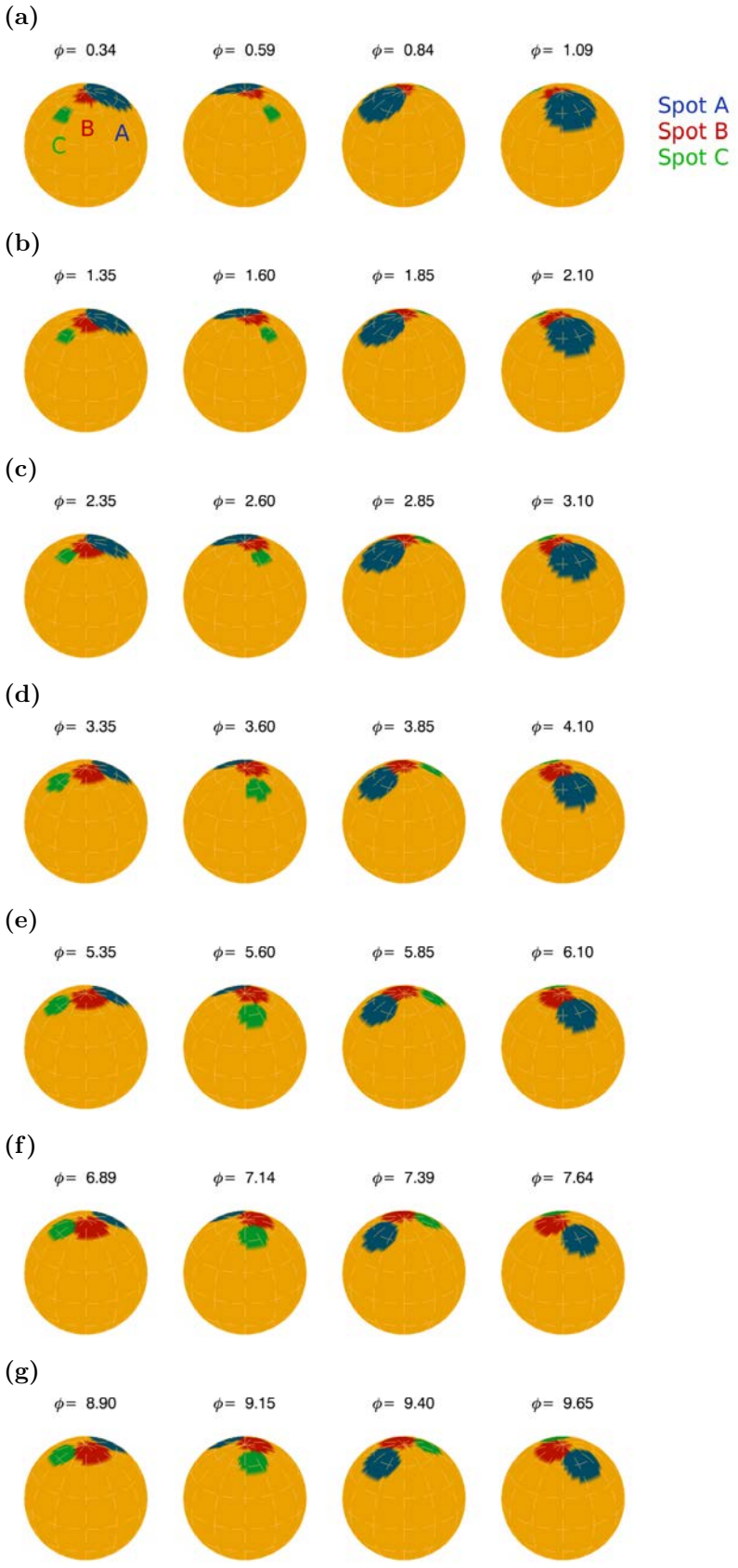

Figure 3.15: Spot-model fits of the Doppler images in Fig. 3.14. Each spot is shown with different color for better visualization.

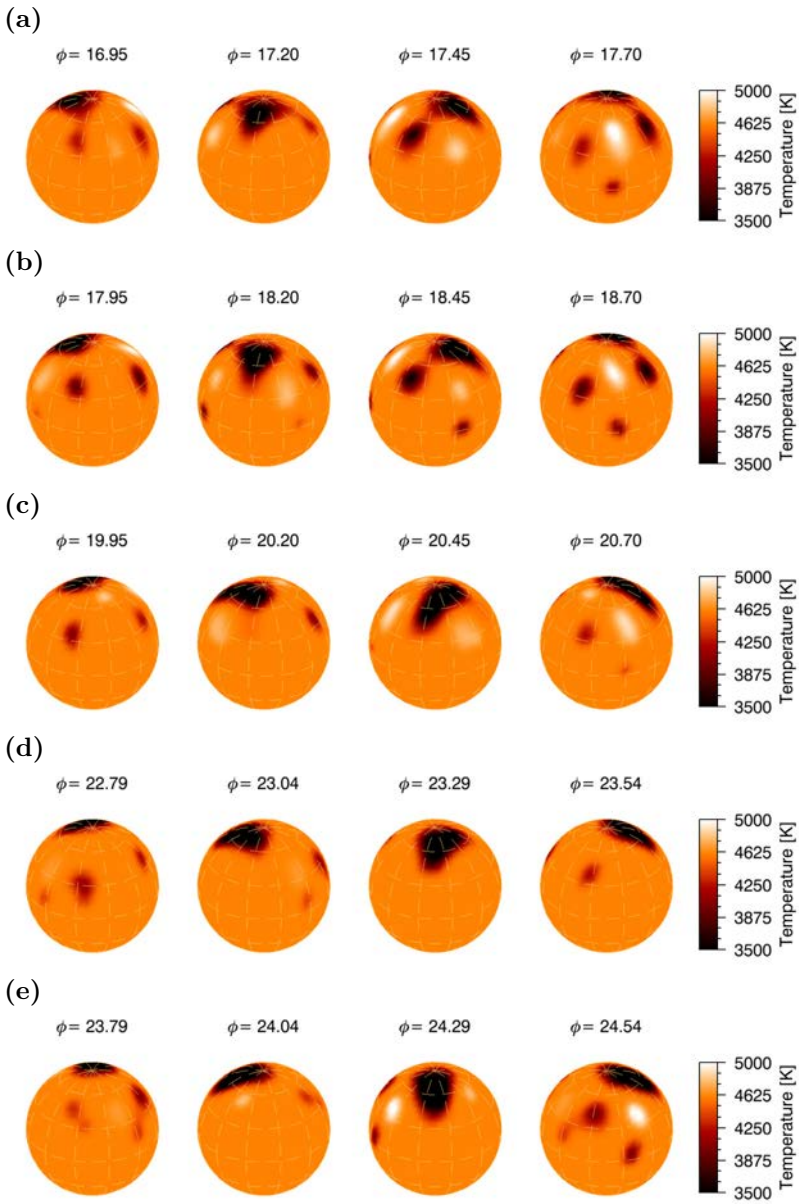

Figure 3.16: Doppler images of XX Tri for the observing season 2007/08. Otherwise as in Fig. 3.14.

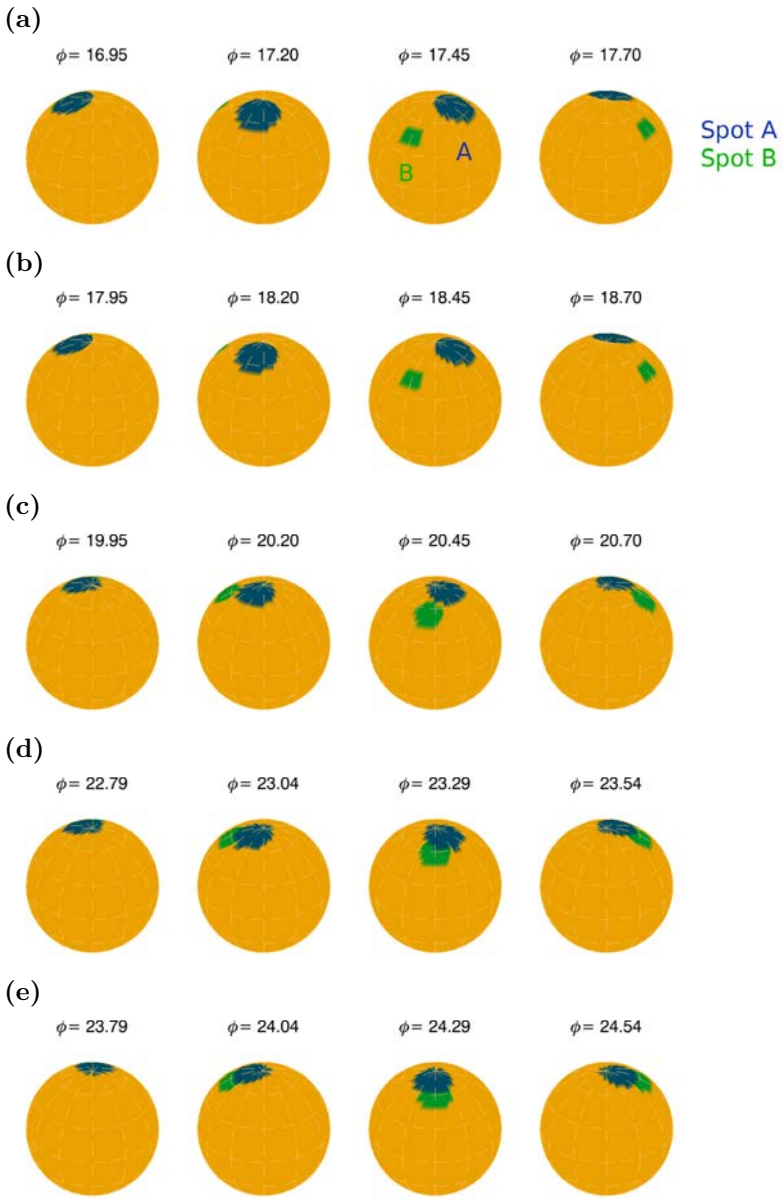

Figure 3.17: Spot-model fits of the Doppler images in Fig. 3.16. Otherwise as in Fig. 3.15.

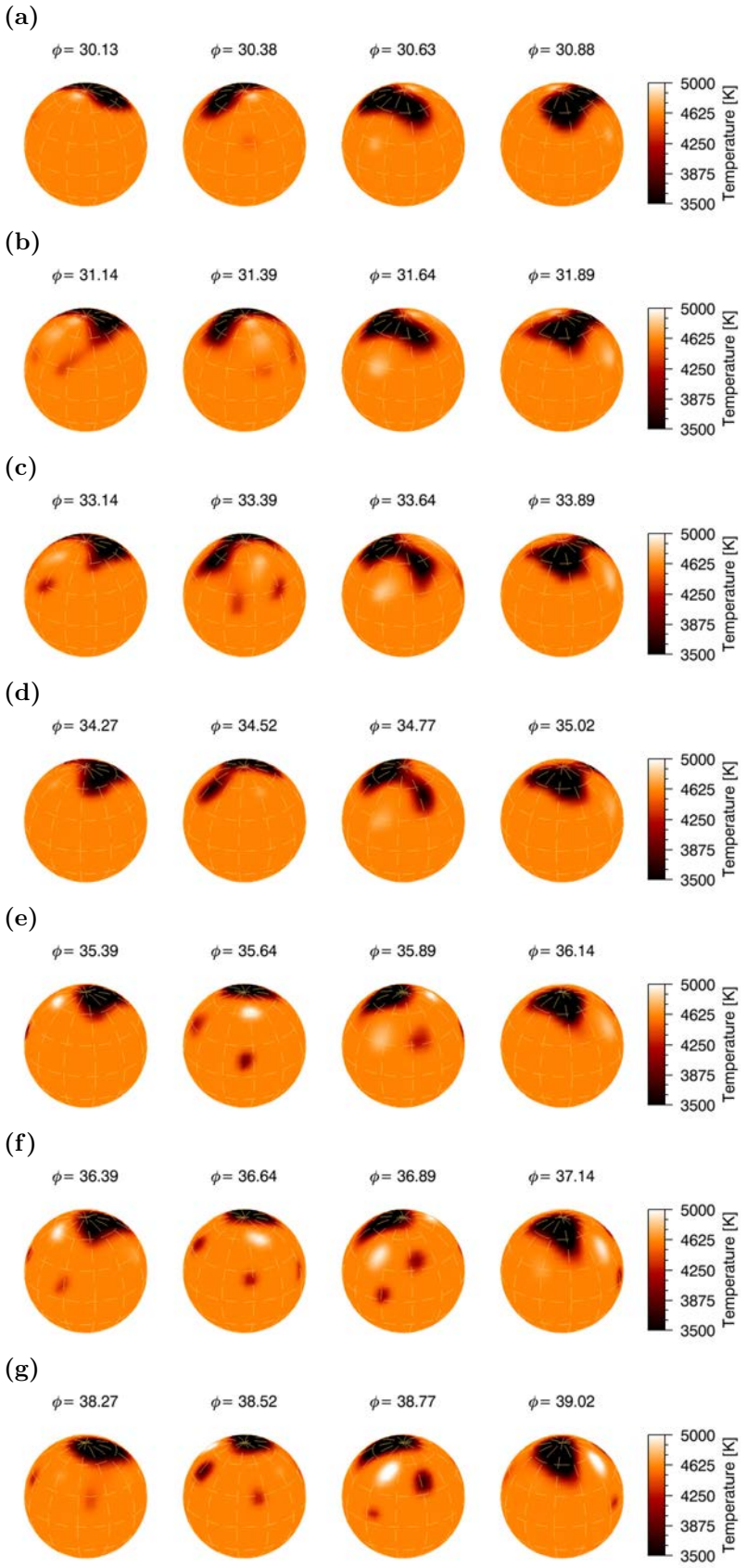

Figure 3.18: Doppler images of XX Tri for the observing season 2008/09. Otherwise as in Fig. 3.14.

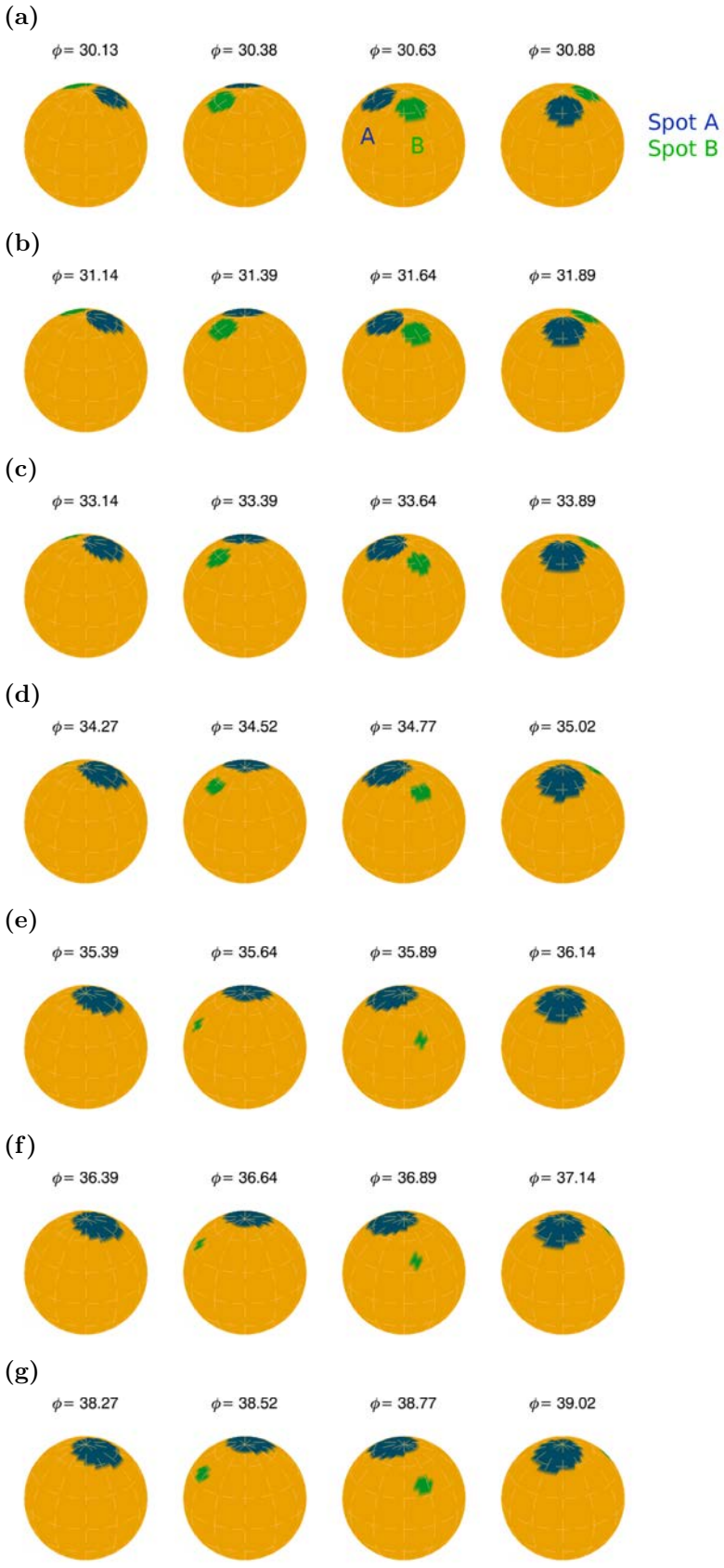

Figure 3.19: Spot-model fits of the Doppler images in Fig. 3.18. Otherwise as in Fig. 3.15.

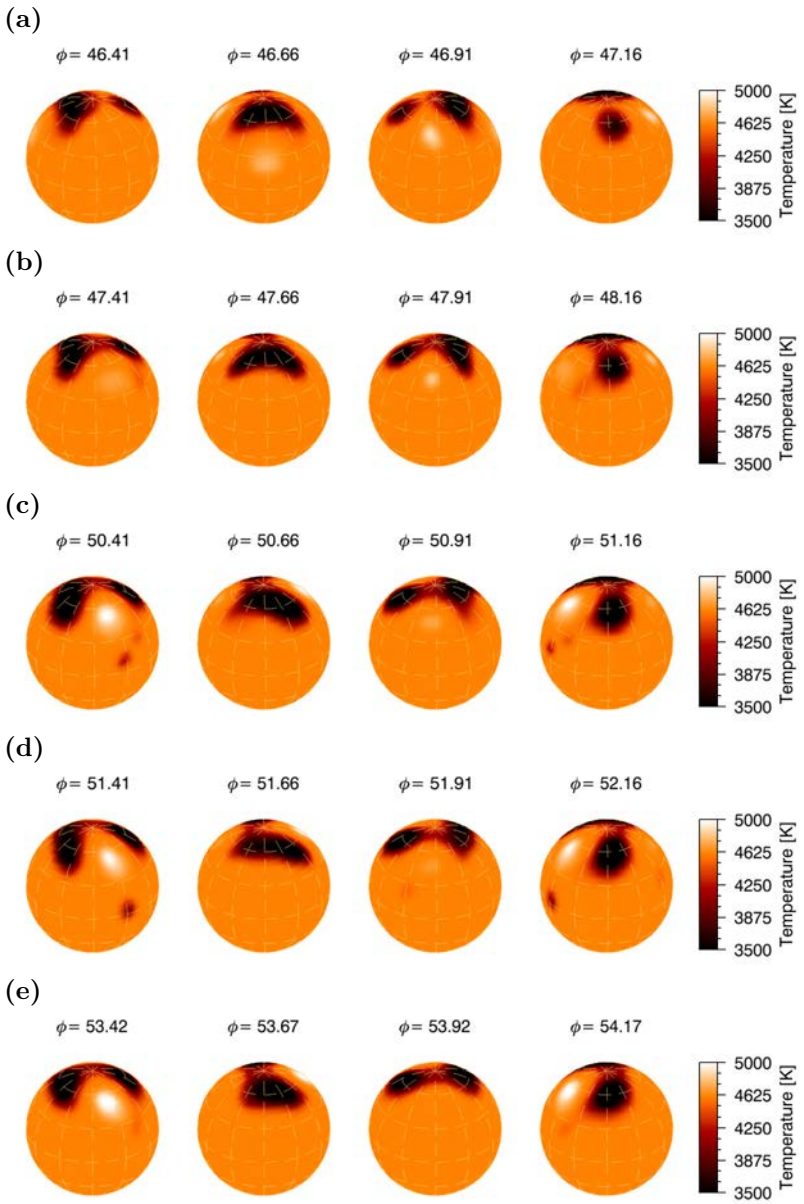

Figure 3.20: Doppler images of XX Tri for the observing season 2009/10. Otherwise as in Fig. 3.14.

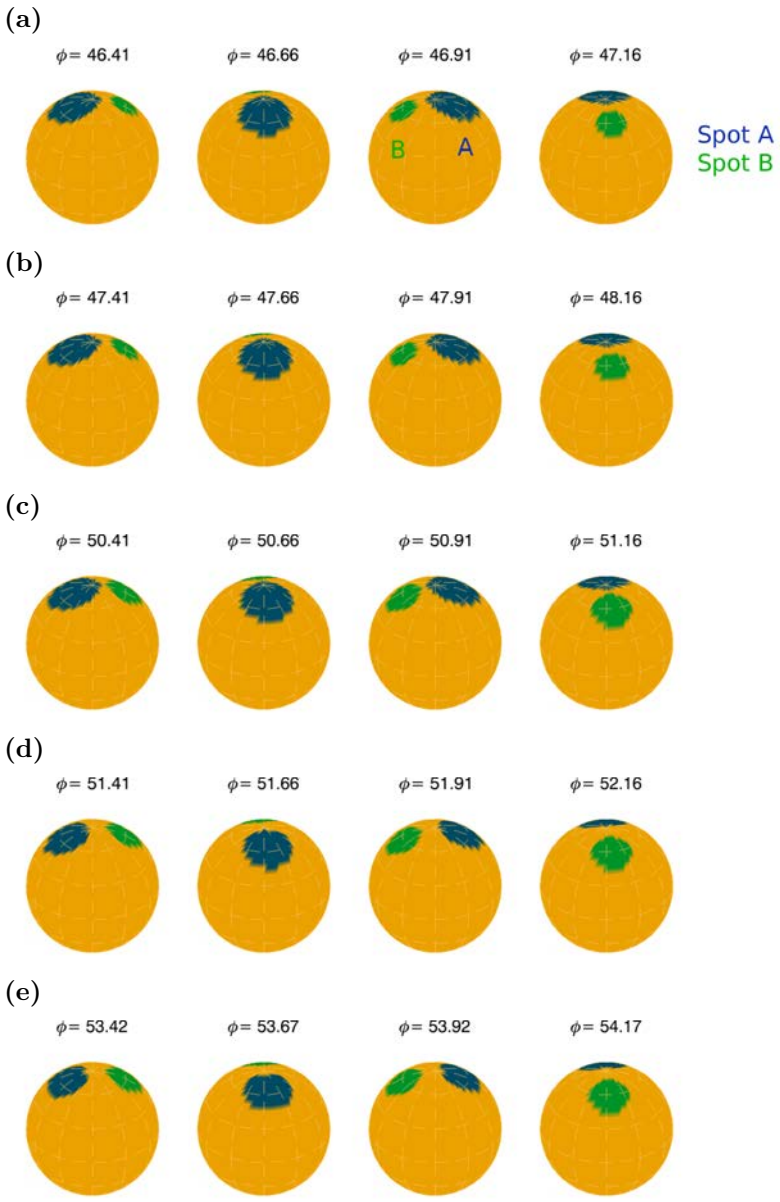

Figure 3.21: Spot-model fits of the Doppler images in Fig. 3.20. Otherwise as in Fig. 3.15.

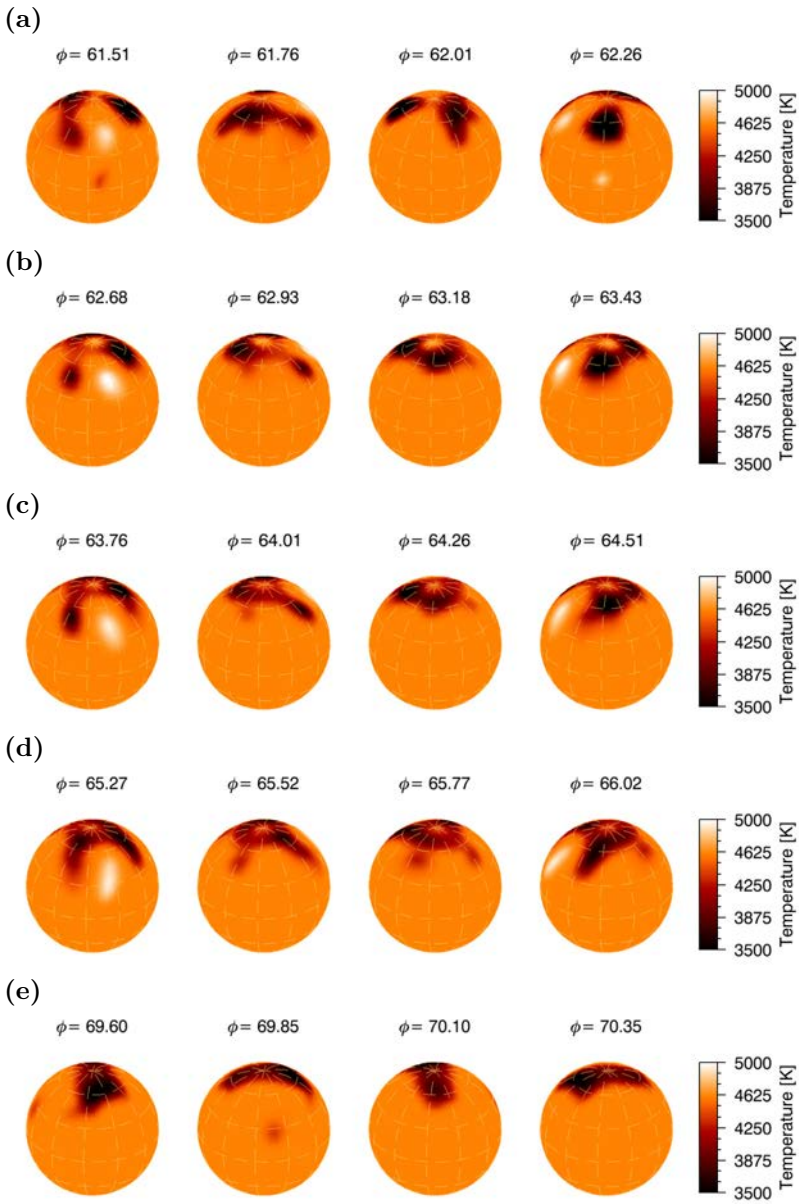

Figure 3.22: Doppler images of XX Tri for the observing season 2010/11. Otherwise as in Fig. 3.14.

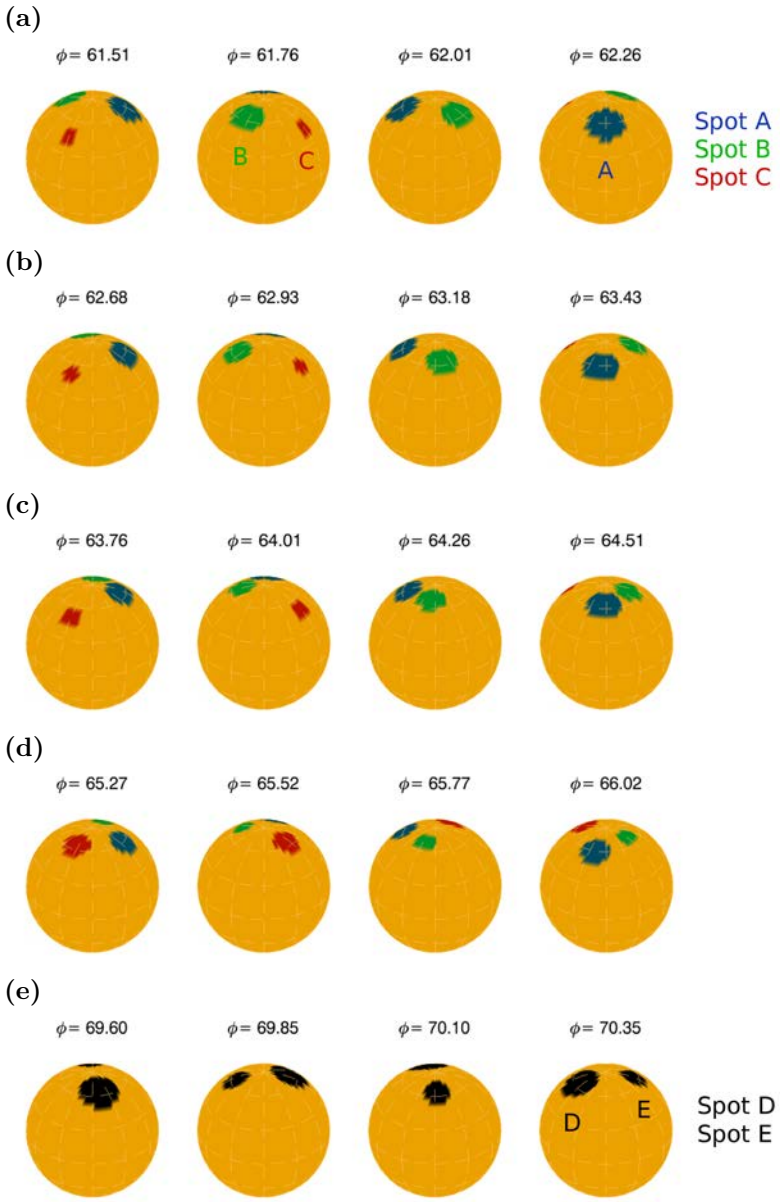

Figure 3.23: Spot-model fits of the Doppler images in Fig. 3.22. Otherwise as in Fig. 3.15.

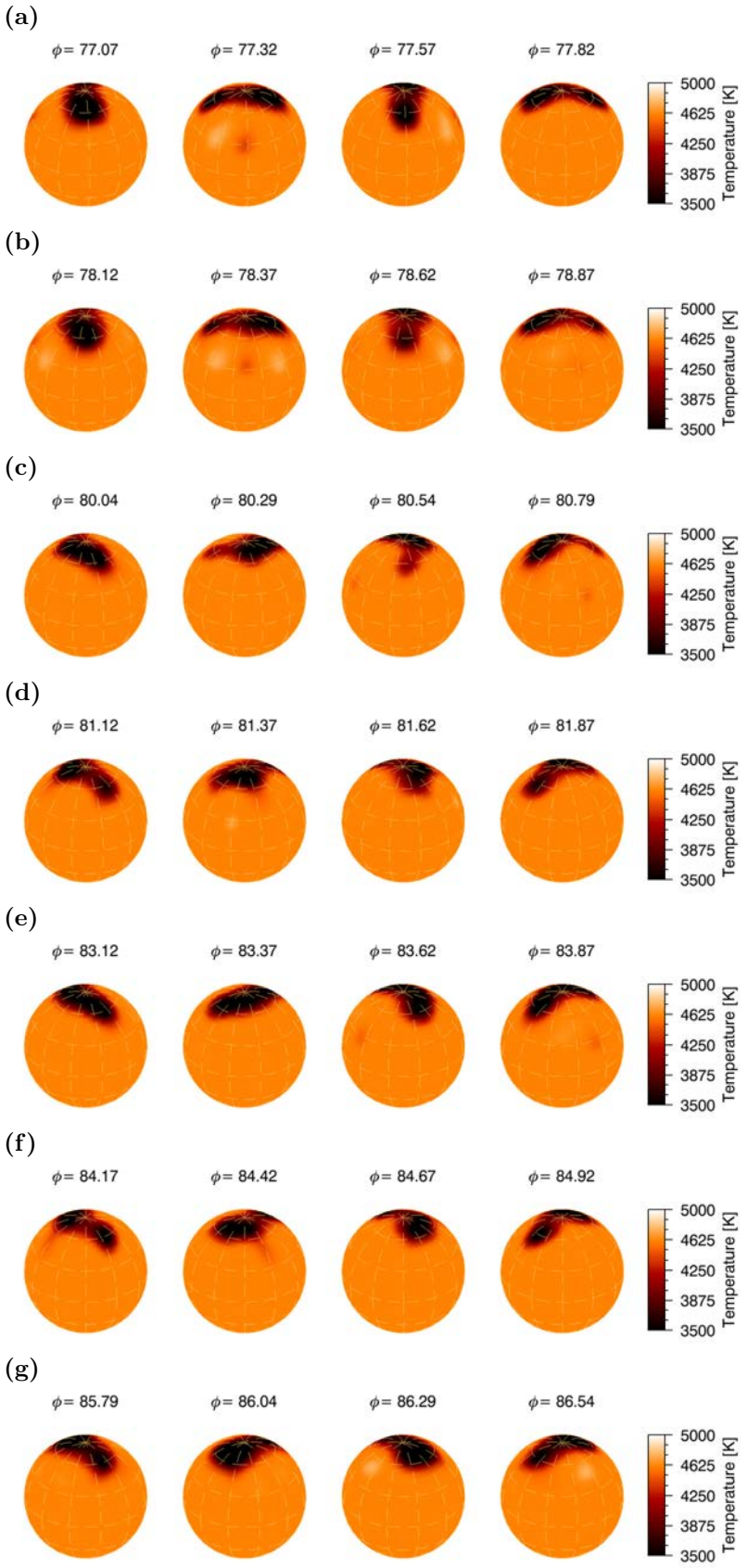

Figure 3.24: Doppler images of XX Tri for the observing season 2011/12. Otherwise as in Fig. 3.14.

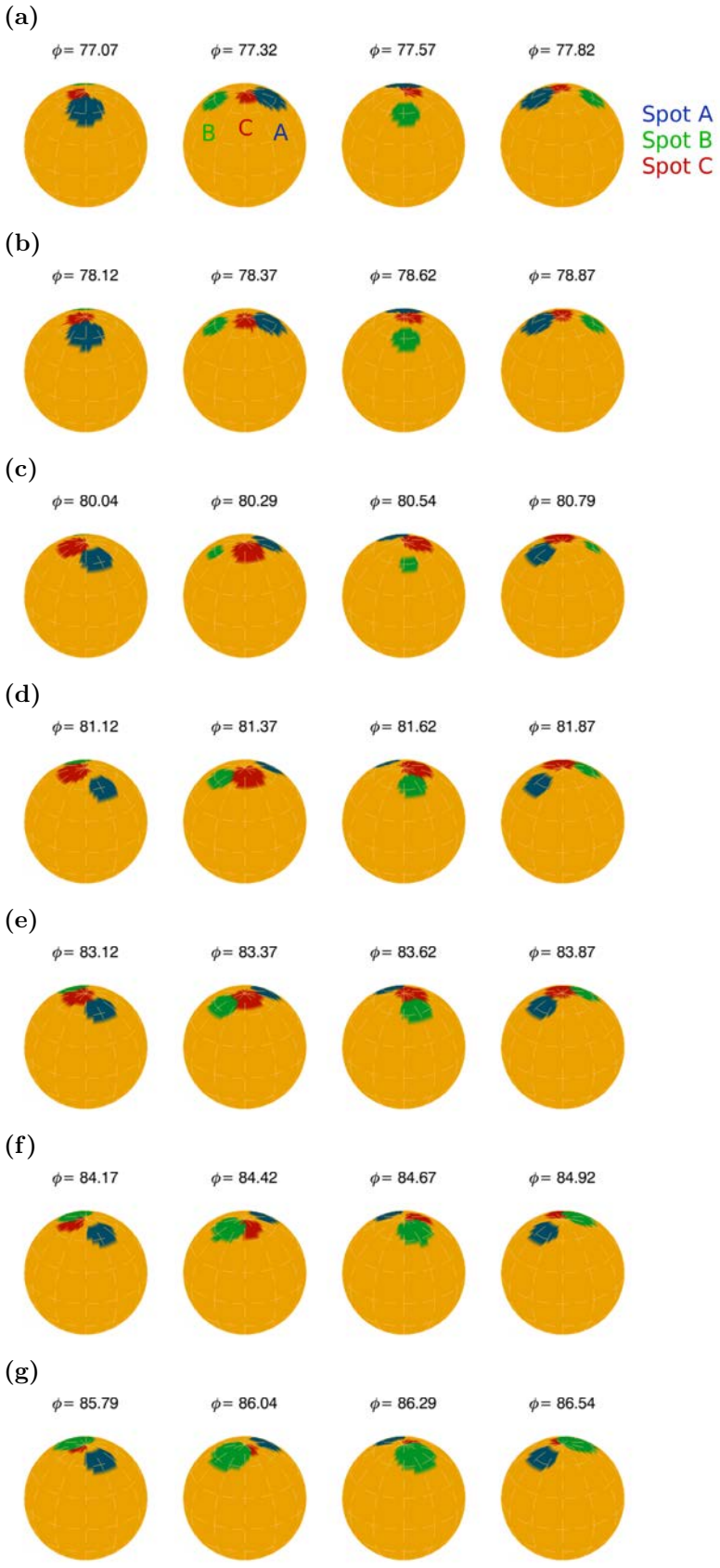

Figure 3.25: Spot-model fits of the Doppler images in Fig. 3.24. Otherwise as in Fig. 3.15.

4 Spot evolution analysis and results

A total of 36 Doppler images are reconstructed over a timespan of six years. For each observing season we obtained between 5 to 7 consecutive temperature maps, showing systematically changing spot distribution and morphology such as spot fragmentation and spot merging as well as spot decay and formation. This time-series of Doppler images is currently the best-sampled spatial and temporal stellar surface resolution.

In this chapter we investigate and determine several phenomena of stellar activity. At first, we calculate "lightcurves" of each temperature map and compare their rotational modulation and temporal behavior with the results from our spectroscopic and photometric analysis, see Chapter 2.5 and 2.6, respectively. Furthermore, we analyze spot decay and formation rates from the spot-model fits, resulting in the determination of a starspot decay law. This allow us to determine a magnetic diffusivity and thus to infer an activity cycle. In addition, we analyze our Doppler imagery in terms of differential rotation and active longitudes.

4.1 Temperature modulation

In order to compare our Doppler maps with photometric lightcurve variations we have to reduce the two-dimensional temperature maps into one-dimensional "lightcurves". In analogy to a measured intensity, we calculate an area-integrated "temperature-flux", where each segment of the visible stellar hemisphere contributes its temperature according to the angle between its projection and the line-of-sight. Furthermore, we corrected for limb-darkening. In order to get a temporal curve, we calculate the temperature-flux for each Doppler map in 20 steps, each with an rotational shift of $\Delta\phi = 0.05$. The resulting one-dimensional temperature-flux lightcurves for each map and observational season are shown in Fig. 4.1.

The overall rotational modulation of the temperature-flux for each observing season is in good agreement with the results from lightcurve variations (Fig. 2.12 - 2.17) as well as with the temperature variations obtained from spectroscopic analysis (Fig. 2.8). The longitudinal position (or rotational phase) of large spots is clearly detectable and thus confirm our suggestions of spot-modulated variations in our photometric and spectroscopic analysis.

This consistency in rotational spot-modulation is a very successful result, as two completely different datasets are used, even if this agreement should be obvious from the theoretical point of view. On the one hand, we study differential photometry using broad-band filters. On the other hand, we analyze spectroscopic observations with two different approaches. As one method based on surface temperature determination by fitting each observed spectrum to model-spectra using several spectral orders simultaneously, the other method calculates temperature-flux lightcurves from reconstructed Doppler images using several absorption line profiles.

In Fig. 4.2 the temperature-flux variations over six years and its corresponding periodogram are shown. The periodogram reveals the same accumulation of peaks between ≈ 23-25 days, as well as a peak around 12 days, caused by spots on opposite hemispheres.

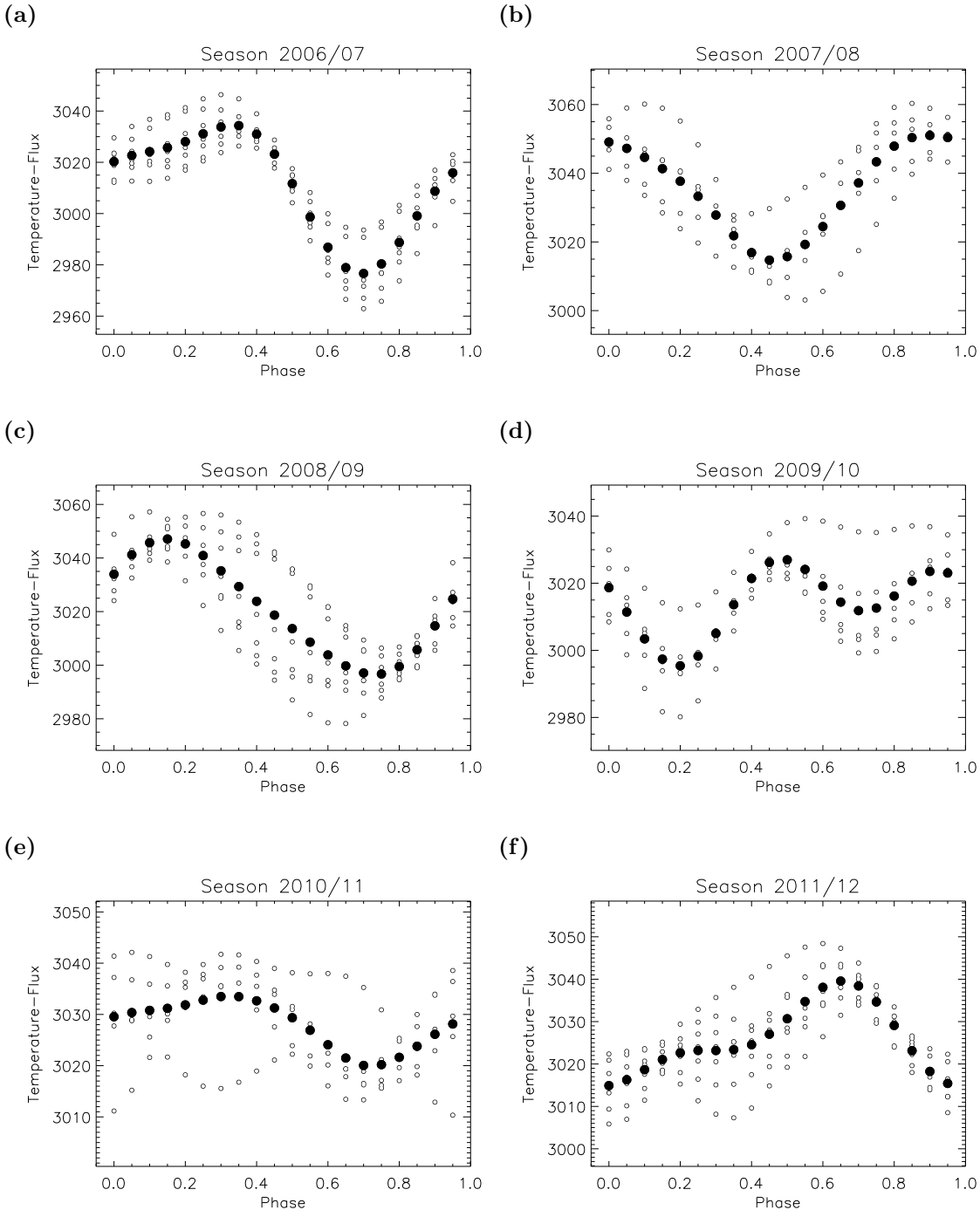

Figure 4.1: Temperature-flux variations #1 on XX Tri from 2006 to 2012. Shown are the rotational modulation of the temperature maps for each observing season. The filled circles represent the seasonal mean variation, whereas the unfilled circles represents each single temperature map.

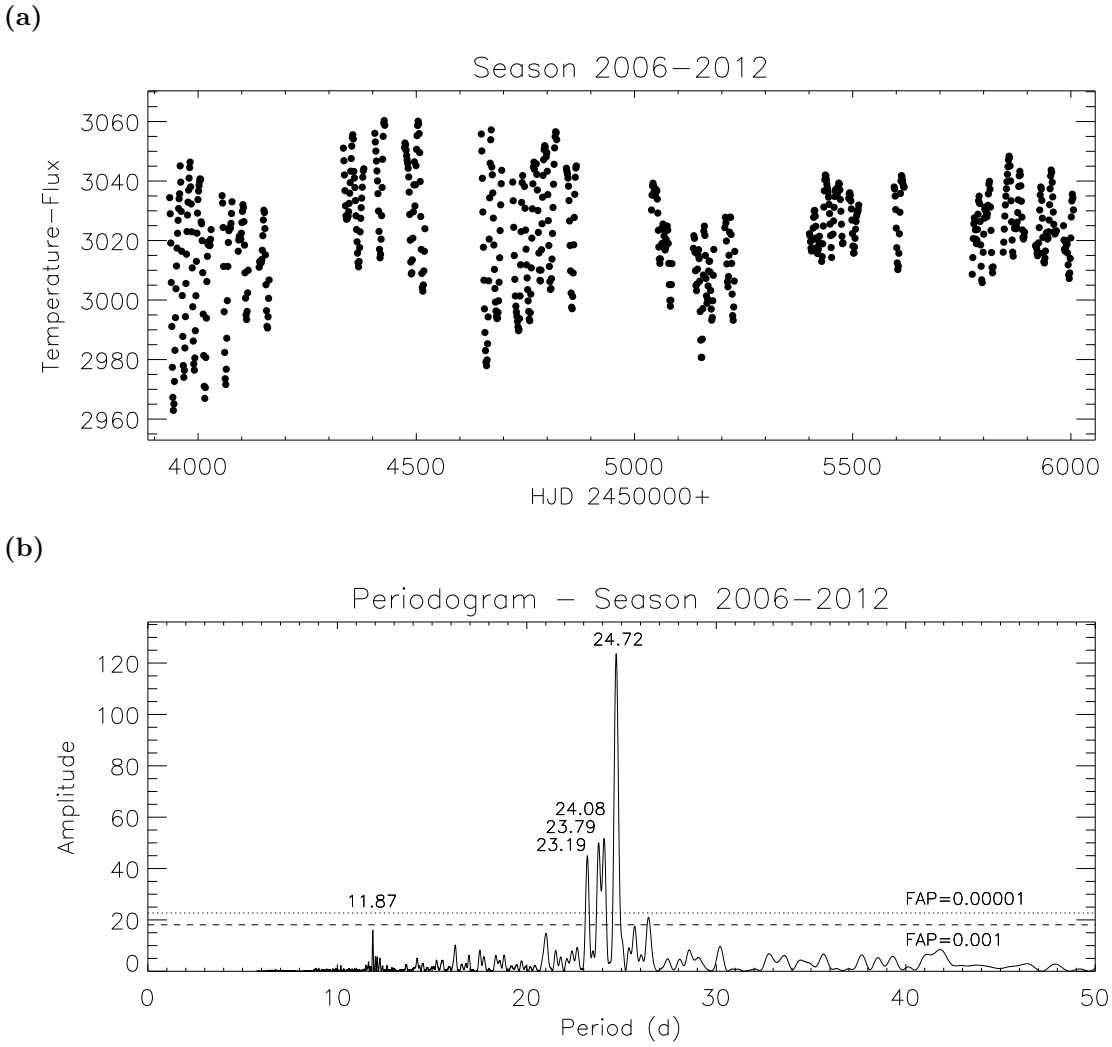

Figure 4.2: Temperature-flux variations #2 on XX Tri from 2006 to 2012. a) Shown is the temperature-flux variation over the total timespan of six years. b) Shown is the corresponding periodogram.

4.2 Spot area evolution

In the following, spot area always refers to the spot area deduced from the spot-model analysis. In each observing season, we see both decay and growth of individual spots. From these spots we infer a grand average linear area decay/formation law of

$$dA(t)/dt = D = -0.022 \pm 0.002 \text{ SH/day} . \tag{4.1}$$

As known from sunspot-decay studies (e.g. Martínez Pillet 2002), the application of a linear law is the most appropriate way to describe sunspot decay as well as sunspot growth rates. Fig. 4.3 shows the area evolution of the total spotted area of XX Tri as well as of the individual spots from the spot models for each season. The numerical values of D for each spot together with the overall mean are summarized in Table 4.1.

Table 4.1: Results for spot decay and growth rates. Derived values of D using a linear area decay law of form $dA(t)/dt = D$ for each individual spot. D is given in Solar Hemispheres per day (1 SH = 3.05 Gm^2).

Season	Spot	DI #	D (SH/day)	type
2006/07	A (blue)	1-6	-0.025 ± 0.003	decay
	B (red)	1-6	$+0.017 \pm 0.004$	growth
	C (green)	2-5	$+0.020 \pm 0.012$	growth
2007/08	A (blue)	8-10	-0.021 ± 0.012	decay
	B (green)	8-10	$+0.014 \pm 0.007$	growth
2008/09	A (blue)	13-17	$+0.026 \pm 0.004$	growth
	B (green)	13-17	-0.020 ± 0.003	decay
	B (green)	18-19	$+0.013 \pm 0.009$	growth
2009/10	A (blue)	22-24	-0.019 ± 0.016	decay
	B (green)	20-22	$+0.019 \pm 0.007$	growth
2010/11	A (blue)	25-28	-0.021 ± 0.008	decay
	B (green)	25-28	-0.020 ± 0.007	decay
	C (red)	25-28	$+0.017 \pm 0.009$	growth
2011/12	A (blue)	31-33	-0.021 ± 0.012	decay
	B (green)	30-32	-0.021 ± 0.011	decay
	B (green)	32-36	$+0.030 \pm 0.006$	growth
	C (red)	30-33	$+0.023 \pm 0.006$	growth
	C (red)	33-36	-0.024 ± 0.005	decay
2006-12			$<-0.022 \pm 0.002>$	decay
			$<+0.021 \pm 0.002>$	growth

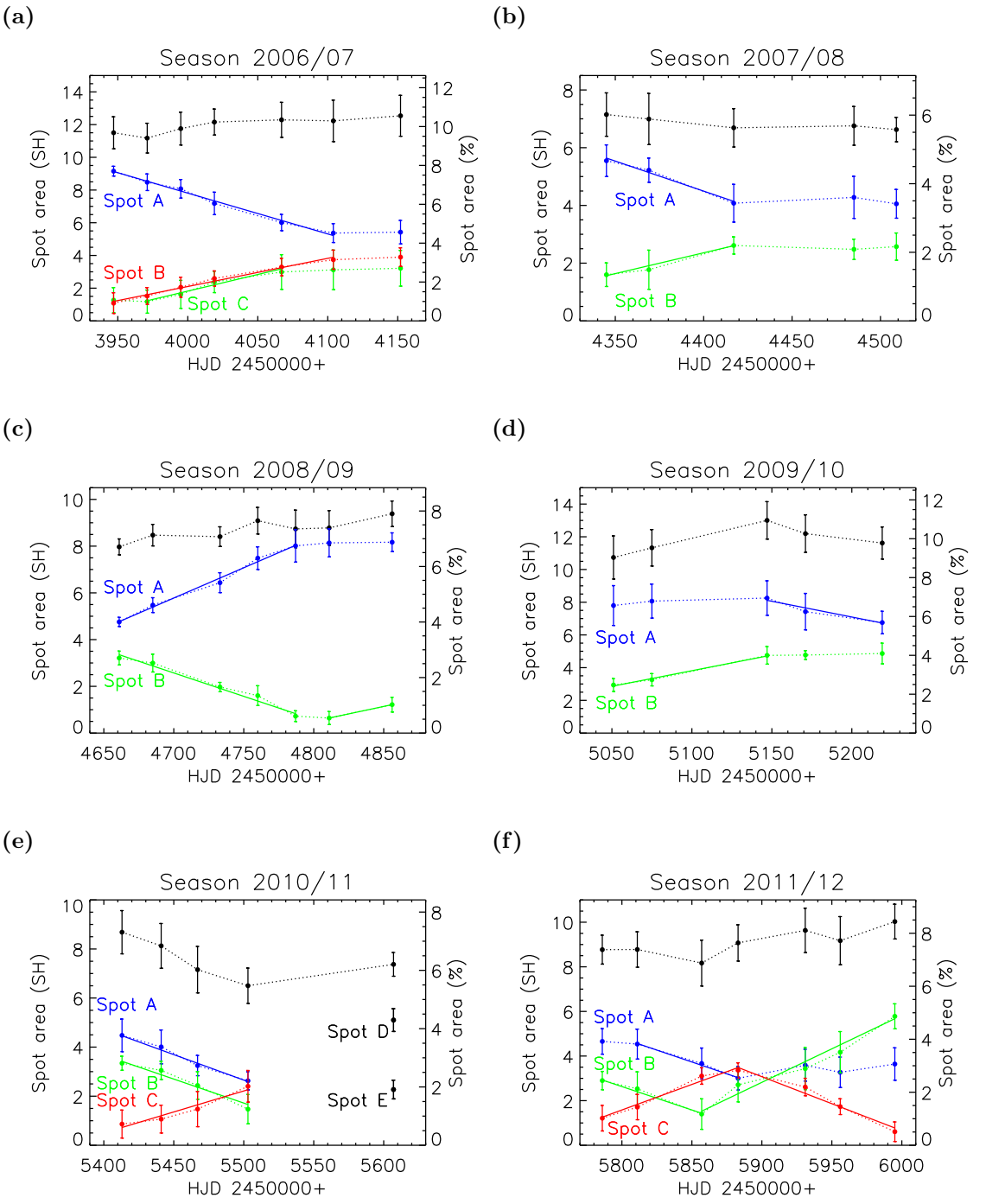

Figure 4.3: Spot area evolution on XX Tri from 2006 to 2012. Shown are the seasonal evolution of the individual spots (dotted colored lines) for each observing season. The solid (colored) lines represent linear fits to the decay or growth of a spot. The black dotted line represents the total spotted area. The spot area is given in Solar Hemispheres (1 SH = 3.05 Gm^2) on the left axis as well as relative to the total area of the stellar hemisphere of XX Tri on the right axis.

Season 2006/07

Three artificial spots are sufficient to match the observed spot distribution in this season. The three spots appear partly merged and make up for the elongated polar-spot appendage in the Doppler images. In the case of overlapping spots, the overlapped area refers to the larger spot. The two overlapping spots A and B fragment while the larger spot A shrinks and the smaller spot B waxes. Between DI #1-6 ($\Delta t \approx 6.5\ P_{\mathrm{rot}}$) spot A loses around 40 % of its area from 9.2 to 5.4 SH ($D = -0.025 \pm 0.003$ SH/day), while the smaller spot B increases up to more than 3 times its area from 1.1 to 3.7 SH ($D = +0.017 \pm 0.004$ SH/day). It seems that spot A "feeds" spot B, suggesting flux transport between these two spots. Between DI #6-7 both spots A and B remain almost constant in area. Spot C is located on the opposite hemisphere with a longitudinal shift of around 180°. Between DI #2-5 ($\Delta t \approx 5.5\ P_{\mathrm{rot}}$) it waxes to almost 3 times its area from 1.2 to 3.0 SH ($D = +0.020 \pm 0.012$ SH/day). Afterwards, spot C remains almost constant in area. If we would exclude DI #5 (see Chapter 3.5) the determined values of D would be -0.024 ± 0.004 SH/day for spot A, $+0.017 \pm 0.005$ SH/day for spot B, and $+0.016 \pm 0.010$ SH/day for spot C, respectively.

Season 2007/08

We concentrate on the two larger spots (at phases around 17ᵖ25 and 17ᵖ55) for a meaningful analysis of spot area evolution. Both spots A and B are separated by around a quarter of rotation in DI #8. During the observing season they merge, as the larger spot A rotates much slower near the pole than the smaller spot B which is located at mid-latitudes. This indicates that differential rotation is detectable as shown in Chapter 4.4. Between DI #8-10 ($\Delta t = 3\ P_{\mathrm{rot}}$) spot A loses around 25 % of its area from 5.5 to 4.1 SH ($D = -0.021 \pm 0.012$ SH/day), while spot B increases to almost 2 times its area from 1.6 to 2.6 SH ($D = +0.014 \pm 0.007$ SH/day). This phenomenon of two spots interacting with each other, while one spot is decaying and the other one is growing, has also been detected in the previous season. If we would exclude DI #10 (see Chapter 3.5) a reliable determination of D for this season would not have been possible due to the time sampling of the Doppler images. However, removing it from the entire time series has no impact on the mean decay rate.

Season 2008/09

Two spots are sufficient to characterize the spot evolution during this season. The two spots A and B are very close and appear connected to each other as seen in DI #13. The large spot A increases from 4.8 to 8.0 SH ($D = +0.026 \pm 0.004$ SH/day) between DI #13-17 ($\Delta t \approx 5\ P_{\mathrm{rot}}$) and afterwards remains almost constant in area. Within the same timespan, the smaller spot B loses in area from 3.2 to 0.7 SH ($D = -0.020 \pm 0.003$ SH/day). After an almost complete decay, it starts to increase to 2 times its area from 0.6 to 1.2 SH ($D = +0.013 \pm 0.009$ SH/day) between DI #18-19 ($\Delta t \approx 2\ P_{\mathrm{rot}}$). As in the previous season, indications of differential rotation are seen. Spot A is located nearer to the pole than spot B and therefore both spots get separated from each other.

Season 2009/10

Again, two spots are adequate to match the observed spot distribution throughout this season. Both spots A and B are located at opposite hemispheres with a longitudinal shift of around 180°. Between DI #20-22 ($\Delta t = 4\ P_{\rm rot}$) the smaller spot B waxes to around 160 % its area from 2.9 to 4.7 SH ($D = +0.019 \pm 0.007$ SH/day), whereas the larger spot A remains almost constant in area. Between DI #22-24 ($\Delta t = 3\ P_{\rm rot}$) the larger spot A loses in area from 8.3 to 6.8 SH ($D = -0.019 \pm 0.016$ SH/day), whereas the smaller spot B remains almost constant in area.

Season 2010/11

During this season three spots are required to characterize the spot evolution. The two large polar spots A and B are located at opposite hemispheres with a longitudinal shift of around 150° and are moving towards each other. Between DI #25-28 ($\Delta t \approx 4\ P_{\rm rot}$) both spots A and B lose in area from 4.5 to 2.6 SH ($D = -0.021 \pm 0.008$ SH/day) and 3.3 to 1.5 SH ($D = -0.020 \pm 0.007$ SH/day), respectively. During the same timespan the smaller spot C increases from 0.9 to 2.4 SH ($D = +0.017 \pm 0.009$ SH/day) and move towards higher latitudes. There is a large time gap of around four rotations between DI #28-29. During this timespan the spot configuration changes obviously to a 2-spot-model. As it is not clear to assign these spots with spots from DI #25-28, we decide to regard them separately. These two polar spots D and E are located at opposite hemispheres with a longitudinal shift of around 180°. This spot configuration is almost identical with the first DI (#30) of the following observational season.

Season 2011/12

Again, three spots are sufficient to match the observed large-scale spot distribution during this season. As in the first season, the three spots appear partly merged and make up for the elongated polar-spot appendage in the Doppler images. The two spots A and B are located at opposite hemispheres with a longitudinal shift of around 180°. This spot distribution is very similar to the one at the end of the previous season. The larger spot A fragments in two smaller spots A and C between DI #30-32. Spot C is located very close to the pole and rotates much slower than the other two spots A and B. Between the time of DI #33-36 spot C merges with spot B. Therefore, it again suggests flux transport between spot A and B. Spot A loses in area from 4.5 to 3.0 SH ($D = -0.021 \pm 0.012$ SH/day) between DI #31-33 ($\Delta t \approx 3\ P_{\rm rot}$) and remains almost constant in size afterwards. Spot B loses in area from 2.9 to 1.4 SH ($D = -0.021 \pm 0.011$ SH/day) between DI #30-32 ($\Delta t = 3\ P_{\rm rot}$) and waxes between DI #32-36 ($\Delta t \approx 6\ P_{\rm rot}$) up to 5.8 SH ($D = +0.030 \pm 0.006$ SH/day). Spot C increases in area up to 3.4 SH ($D = +0.023 \pm 0.006$ SH/day) between DI #30-33 and decays between DI #33-36 ($\Delta t \approx 4.5\ P_{\rm rot}$) almost completely ($D = -0.024 \pm 0.005$ SH/day).

Summary: spot area evolution

Finally, we note that if we exclude Doppler images #5 and #10, our spot area evolution analysis would lead to an identical mean value for spot decay ($<D> = -0.022 \pm 0.002$ SH/day) and only a marginally increased mean value for spot formation ($<D> = +0.022 \pm 0.002$ SH/day). Therefore, we include them in our analysis. Furthermore, we repeated the entire analysis also for the scattered small cool and/or hot spots at low latitudes. Their respective values of D scatter within the range of the large-scale spots (for small cool spots ± 0.02 for growth and decay, respectively; hot spots ± 0.03), but the time sampling is such that we can not determine a true beginning nor ending of the evolution.

4.3 Active longitudes

Active longitudes are longitudes on which spots occur preferentially. The analysis of long-term photometry as well as time-series Doppler imaging revealed such active longitudes on several stars. Berdyugina & Tuominen (1998) found permanent active longitudes on four RS CVn stars. If two active longitudes, which are typically separated by 180°, change their spot activity, a so-called "flip-flop" occurred. Such a phenomenon was first noticed on the late-type giant FK Com (Jetsu et al. 1991). The average time between such phenomena is referred to as flip-flop cycle and has been observed to be in the range of a few years up to a decade. An observational overview is given in Berdyugina (2007) and Korhonen & Järvinen (2007). In binary stars a longitudinal dependence due to tidal effects is suggested (Holzwarth & Schüssler 2002). Observations show that in binaries preferred longitudes exist on giant components mostly at the substellar points (e.g. Oláh et al. 2002).

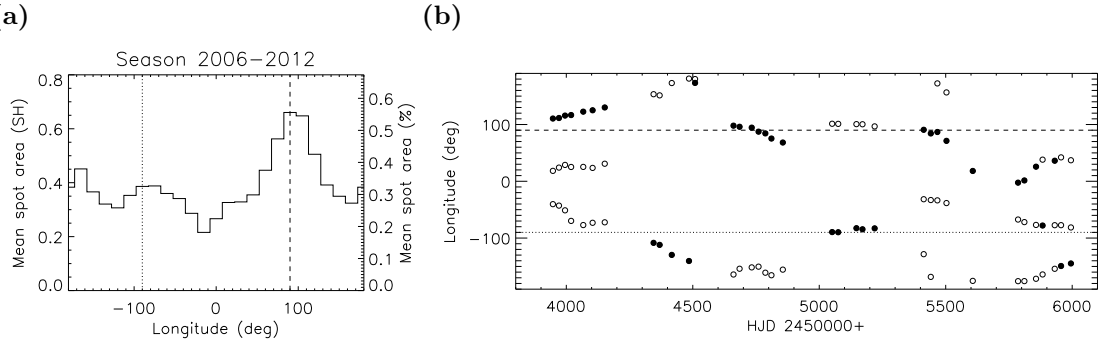

Figure 4.4: Active longitudes on XX Tri from 2006 to 2012. a) Shown is the overall mean distribution of the spot area (histogram in bins of 15°). The spot area is given in Solar Hemispheres (1 SH = 3.05 Gm^2) on the left axis as well as relative to the total area of the stellar hemisphere of XX Tri on the right axis. The dashed line represents the phase towards the companion star, whereas the dotted line represents the phase in the opposite direction. b) Shown are all longitudinal spot centers of the individual spots for all observing seasons. The filled dots represents the larger spot at a certain time. The dashed and dotted lines represent again the phases towards the companion star and in the opposite direction.

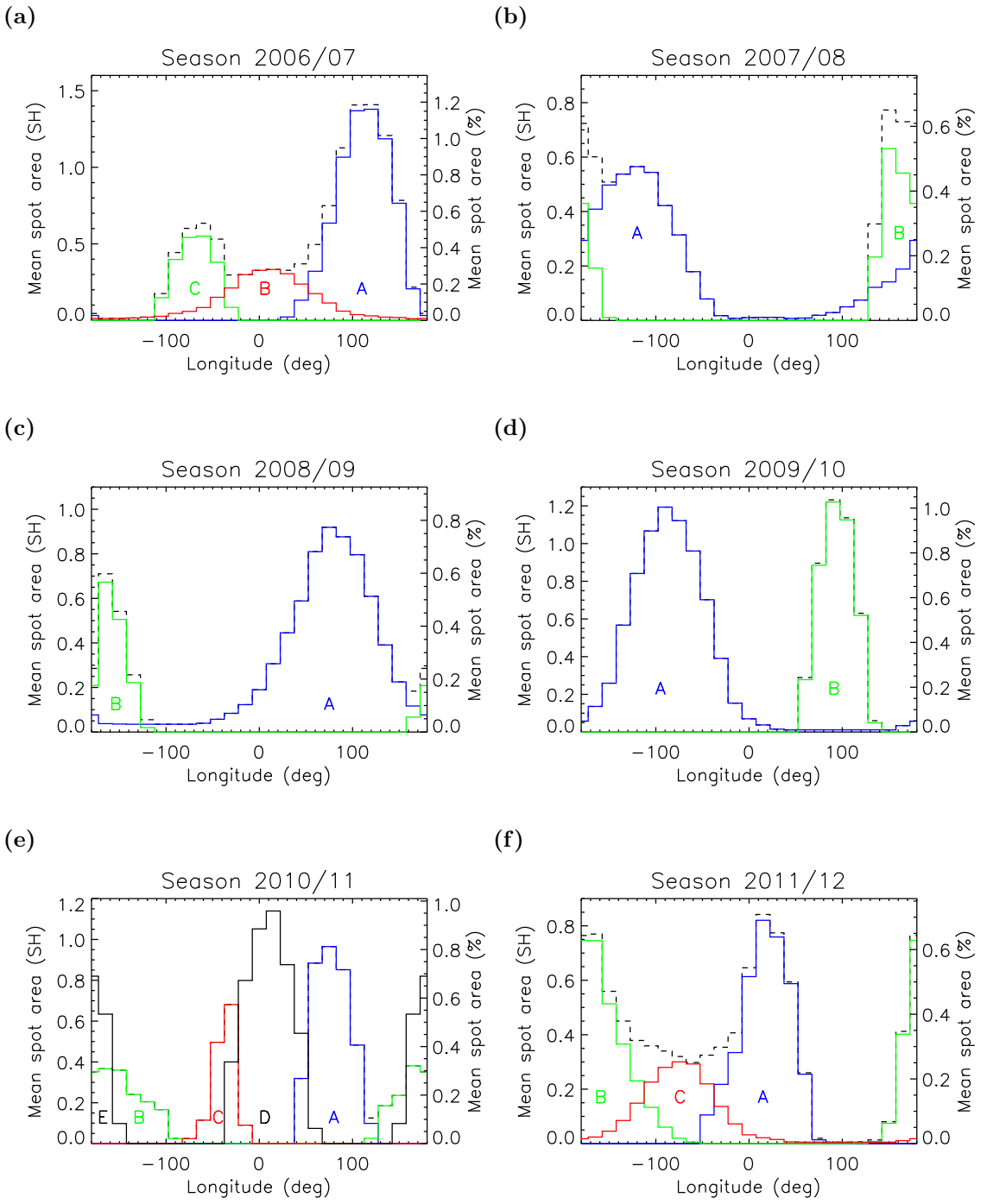

Figure 4.5: Longitudinal spot area distribution on XX Tri from 2006 to 2012. Shown are the seasonal mean distributions of the individual spots (solid colored lines) from our spot-model fits for each observing season (histogram in bins of 15°). The black dashed line represents the total spotted area. The spot area is given in Solar Hemispheres (1 SH = 3.05 Gm^2) on the left axis as well as relative to the total area of the stellar hemisphere of XX Tri on the right axis.

Fig. 4.5 shows the mean longitudinal distributions of all individual spots from our spot-models for each season. There is clear evidence for preferred longitudes

during each season but significantly spread-out in location due to individual spot evolution. A particularly well defined pair of active longitudes separated by 180° is seen in season 2009/10. Averaging the longitudinal spot distribution from all 36 Doppler images, we find the most spotted longitude to appear on average in phase towards the unseen companion star (±90°; Fig. 4.4a). The overall temperature modulation (Fig. 4.2b) already suggested this behavior.

Fig. 4.4b plots the spot centers from the spot-model fits (spots A-E) as a function of time. The larger spot always appears in alternating hemispheres at locations either close to the phase towards the companion star or shifted by around 180°. Only maybe between DI #29-32 the larger spot appears in-between these phases near quadrature. Nevertheless, we interpret this behavior as a flip-flop and estimate a tentative period of around two years.

4.4 Differential rotation

Tracking sunspots is a classic technique to measure solar differential rotation and other surface velocity fields like meridional flows (e.g., Wöhl 2002; Brajša et al. 2002; Wöhl et al. 2010). In case of XX Tri a large number of temperature surface maps with unprecedented good sampling is available, and therefore may enable us to reveal a similarly accurate differential rotation law by tracking individual starspots. Differential rotation has been detected on a number of stars by cross-correlating consecutive Doppler images in longitudinal direction (e.g., Donati & Collier Cameron 1997; Oláh et al. 2002; Barnes et al. 2005; Kővári et al. 2007b). Applying this method to XX Tri, we reconstruct between three and six cross-correlation-function (ccf) maps per observing season, which we average to increase their validity. We did not use the ccf map with DI #29, the last map in season 2010/11, because the time span to the previous map (#28) is comparable large, approximately four rotational periods. Within such a time span, we expect significant local spot evolution. Fig. 4.7 shows the average ccf maps for each observational season. The resulting grand average ccf map, which consists of 29 ccf maps in total, is given in Fig. 4.6a.

We determined the correlation peak for each longitudinal stripe of 5° width with a Gaussian profile and fitted a standard differential rotation law of the form

$$\Omega(b) = \Omega_{\rm eq} - \Delta\Omega \sin^2(b) \ , \tag{4.2}$$

which is usually used for differential rotation measurements on stars. $\Omega(b)$ represents the angular velocity at latitude b, while $\Delta\Omega = \Omega_{\rm eq} - \Omega_{\rm pole}$ represents the difference between the angular velocities at the equator and at the pole, respectively. The surface shear parameter α is defined as $\Delta\Omega/\Omega_{\rm eq}$, and the lap-time as the reciprocal of the rotational shear, i.e. the time it takes for the equator to do a full lap more than the pole. Alternatively, we fitted a differential rotation law of the form

$$\Omega(b) = \Omega_{\rm eq} + \Omega_1 \sin^2(b) + \Omega_2 \sin^4(b) \ , \tag{4.3}$$

which is usually used for differential rotation measurements on the Sun. In this case the angular velocity at the pole is defined as $\Omega_{\rm pole} = \Omega_{\rm eq} + \Omega_1 + \Omega_2$. Fig. 4.8 and Fig. 4.6b show the observed differential rotation pattern determined from the ccf maps together with the best fit of the differential rotation following Eq. 4.2 and Eq. 4.3. In Table 4.2 and Table 4.3 all seasonal fits for differential rotation are listed.

Table 4.2: Results #1 for differential rotation. Parameters for best fits using Eq. 4.2. $\Omega_{\rm eq}$ is fixed for $P_{\rm rot} = 24.0$ d.

Season	N ccf maps	$\Delta\Omega$ (°/d)	α	lap-time (d)
2006/07	6	0.05 ± 0.03	0.003 ± 0.002	≈ 6870
2007/08	4	0.30 ± 0.08	0.020 ± 0.005	≈ 1190
2008/09	6	0.29 ± 0.06	0.019 ± 0.004	≈ 1240
2009/10	4	0.11 ± 0.04	0.007 ± 0.003	≈ 3290
2010/11	3	0.19 ± 0.06	0.013 ± 0.004	≈ 1870
2011/12	6	0.00 ± 0.04	0.000 ± 0.003	—
2006-12	29	0.13 ± 0.04	0.009 ± 0.003	≈ 2740

Table 4.3: Results #2 for differential rotation. Parameters for best fits using Eq. 4.3. $\Omega_{\rm eq}$ is fixed for $P_{\rm rot} = 24.0$ d.

Season	N ccf maps	Ω_1 (°/d)	Ω_2 (°/d)	α	lap-time (d)
2006/07	6	0.53 ± 0.04	-0.68 ± 0.04	0.010 ± 0.001	≈ 2430
2007/08	4	0.83 ± 0.20	-1.35 ± 0.23	0.035 ± 0.010	≈ 690
2008/09	6	0.51 ± 0.16	-0.95 ± 0.18	0.030 ± 0.011	≈ 810
2009/10	4	0.22 ± 0.21	-0.39 ± 0.24	0.011 ± 0.012	≈ 2130
2010/11	3	-0.20 ± 0.25	0.01 ± 0.33	0.013 ± 0.058	≈ 1890
2011/12	6	0.64 ± 0.14	-0.74 ± 0.17	0.007 ± 0.002	≈ 3460
2006-12	29	0.45 ± 0.07	-0.69 ± 0.09	0.016 ± 0.003	≈ 1530

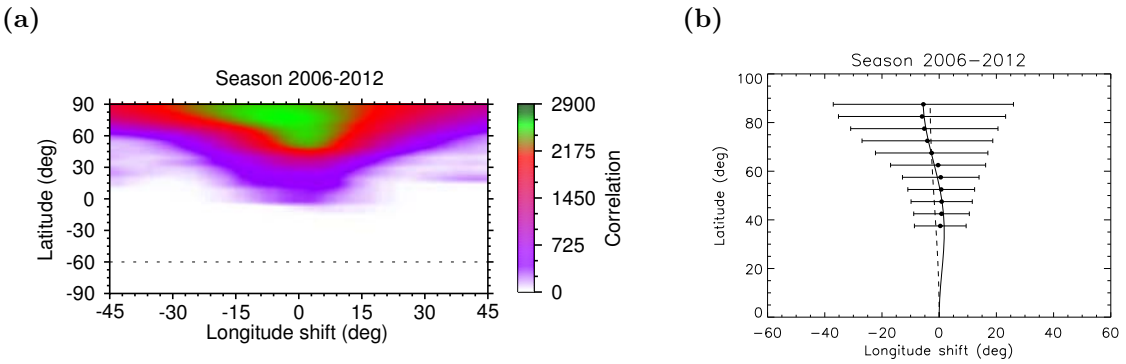

Figure 4.6: a) Overall cross-correlation-function map from 2006 to 2012. The map represents the average ccf map of all ccf maps shown in Fig. 4.7, thus consisting of 29 ccf maps in total.
b) Overall differential rotation signature. Analyzing the ccf map reveals a weak solar-like differential rotation. The dots are the correlation peaks per 5°-latitude bin and their error bars are defined as the FWHMs of the corresponding Gaussians. The dashed line represents a fit using Eq. 4.2, whereas the solid line represents a fit using Eq. 4.3, which yields a much better fit. All fit parameters are summarized in Table 4.2 and Table 4.3.

Because most spots on XX Tri appear at high latitudes, Eq. 4.3 with its $\sin^4(b)$ term leads to a much better fit to the observed shear than Eq. 4.2. Therefore, we favor Eq. 4.3 over Eq. 4.2. All observing seasons show a solar-like differential rotation law with an overall shear parameter of $\alpha = 0.016 \pm 0.003$ and a lap-time of ≈ 1500 days. The surface shear on XX Tri is therefore only around a tenth of the solar value.

Fig. 4.7 shows the ccf maps of each observational season. In Fig. 4.8 the observed differential rotation pattern determined from the ccf maps, together with the best fit of the differential rotation following Eq. 4.2 and Eq. 4.3 are shown.

4.5 Stellar cycle prediction

Because turbulent diffusion is believed to be the dominating effect of spot decay, the decay rate of spot area is directly proportional to the turbulent diffusivity (Meyer et al. 1974; Krause & Rüdiger 1975)

$$dA/dt = -4\pi\eta_T \ . \tag{4.4}$$

Using the weighted mean decay rate of $D = -0.022 \pm 0.002$ SH/day from our analysis in Table 4.1 leads to a turbulent diffusivity of $\eta_T = (6.3 \pm 0.5) \times 10^{14}$ cm^2/s. This value is at minimum one order of magnitude higher than what is predicted for solar values which vary from 10^{10} cm^2/s (Dikpati & Charbonneau 1999) to 10^{13} cm^2/s (Rüdiger & Kitchatinov 2000). The diffusion timescale for the magnetic field inside the convection zone (CZ) is given by

$$\tau = \frac{L_{CZ}^2}{\eta_T} \ , \tag{4.5}$$

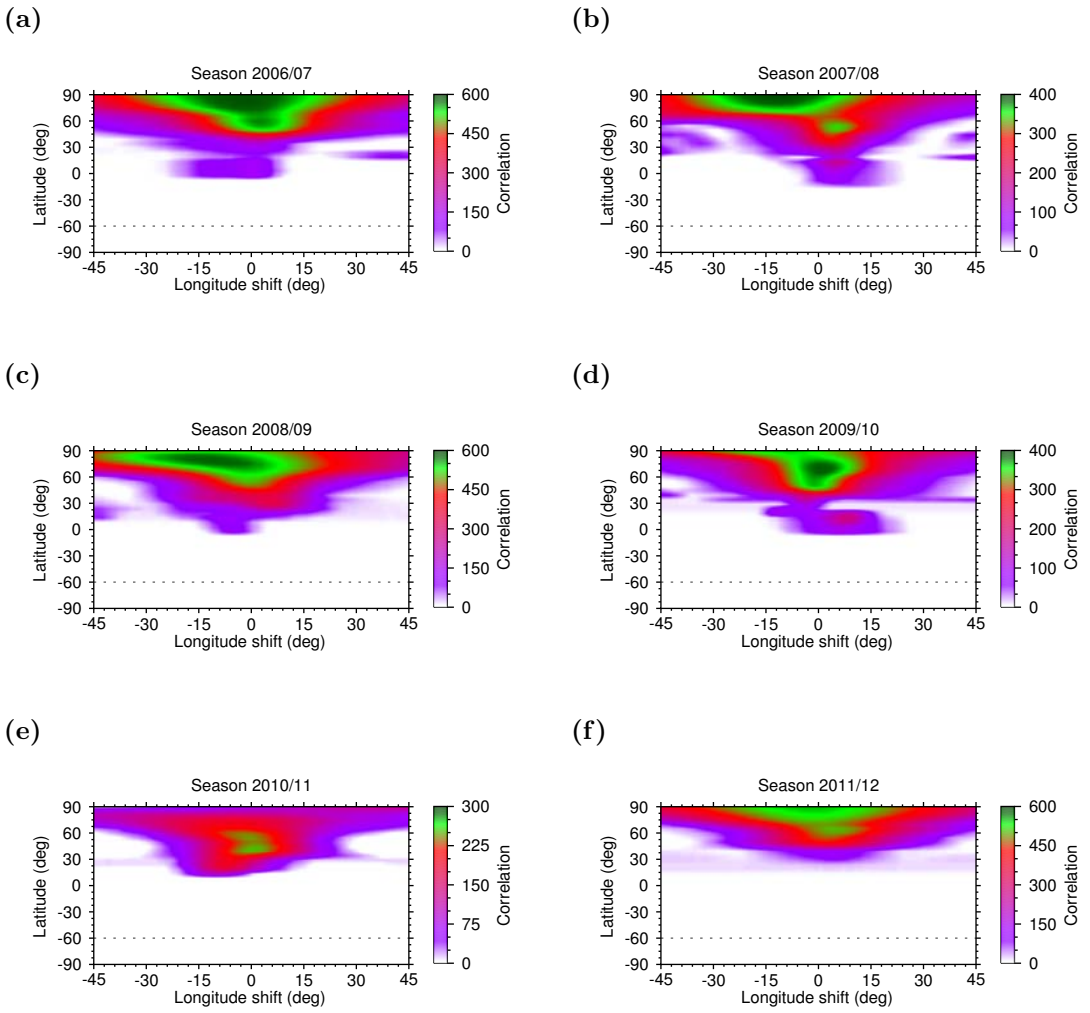

Figure 4.7: Cross-correlation function maps from 2006 to 2012. Each map represents the average ccf map for one observing season.

where L_{CZ}^2 is the width of the stellar convection zone. Using stellar models calculated with the Yale Rotational stellar Evolution Code (YREC; see Spada et al. (2013) for more details) we estimate a depth of 0.94 $R_\star$ for the convection zone of XX Tri. Thus, the diffusion timescale leads to an activity cycle length of approximately 26 ± 6 years.

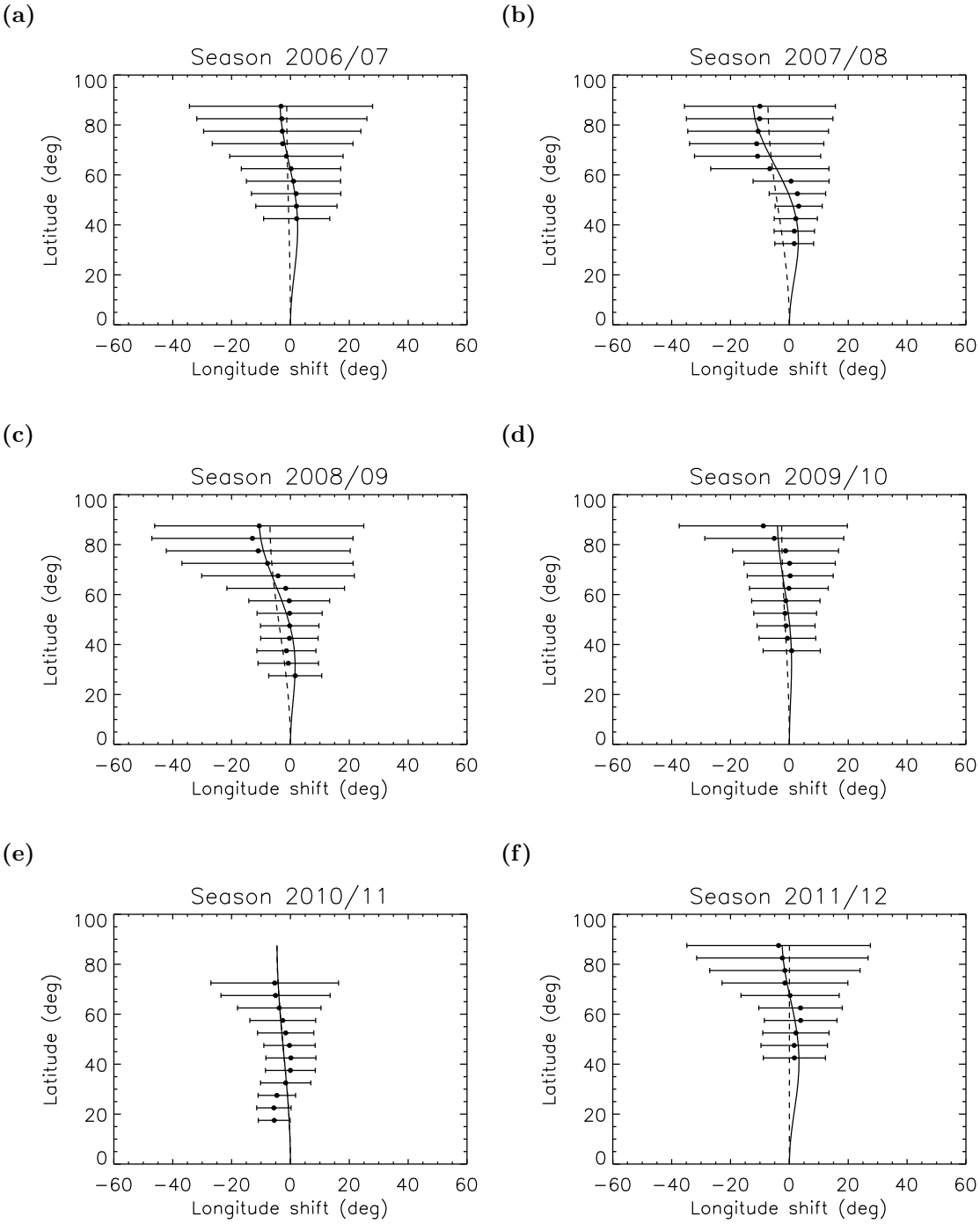

Figure 4.8: Differential rotation signatures from 2006 to 2012. Analyzing the ccf maps shown in Fig. 4.7 reveal a weak solar-like differential rotation. The dots are the correlation peaks per 5°-latitude bin and their error bars are defined as the FWHMs of the corresponding Gaussians. The dashed line represents a fit using Eq. 4.2, whereas the solid line represents a fit using Eq. 4.3. The parameters for each fit are summarized in Table 4.2 and Table 4.3.

5 Discussion and conclusions

Thanks to our robotic STELLA telescopes the present time-series of Doppler images resolves 36 single stellar rotations over a timespan of six years. The sample is long enough that it enables, for the first time, a direct determination of a starspot decay law. Our target is the K0 giant XX Tri with a rotation period (≈ 24 d) comparable to that of the Sun but being more massive by 26 % and significantly older with an age of ≈ 8 Gyrs. Such a combination of parameters is only possible because the star is a component of a close binary. A comparison with solar analogies is therefore only for general guidance.

The time-series of Doppler images enabled the cartography of a variety of surface activity phenomena such as active longitudes, flip-flops and differential rotation on XX Tri. However, our main result is a spot decay law leading to a prediction of a magnetic activity cycle solely based on an observationally constrained value of the turbulent magnetic diffusivity.

Beside our surface temperature maps, we redetermined stellar and orbital properties of XX Tri obtained from spectroscopic and photometric analyses. We investigated both datasets for rotationally spot-modulation and found a strong correlation as well as in comparison to the results with our reconstructed Doppler images.

Stellar properties

The redetermination of the stellar properties was necessary, as the previously determined parameters were achieved around 16 years ago (Strassmeier 1999). Since then, long-term photometric and spectroscopic observations were taken, and still continuing. In particular, the redetermined parallax (van Leeuwen 2007) and the increase of the maximum brightness (Oláh et al. 2014) of XX Tri, strongly influenced the obtained properties of the red giant star, as well as the determined values of surface gravity and metallicity for the first time.

Whereas the most stellar properties changed within 15 %, the mass and age of XX Tri changed dramatically due to changes in luminosity, temperature, and metallicity. The redetermined values imply that XX Tri is lighter by 30 % and older by more than 400 %.

Spot decay and stellar activity cycle

The individual spot decay rates, $dA/dt = D$, scattered between -0.019 and -0.025 SH/day over the six year observing period with a mean value of $D = -0.022 \pm 0.002$ SH/day. We note that the rates for spot growth scattered between $+0.013$ and $+0.030$ SH/day with a mean of $D = +0.021 \pm 0.002$ SH/day and thus of nearly the same amount as the decay. In above units, the spot decay on XX Tri would be of the order of 10^4 times faster than what Bumba (1963) suggested for sunspots. Bumba proposed a mean value for D of -4.2 MSH/day. However,

the areal size of starspots on XX Tri is also 10^3 to 10^4 times larger than the largest observed sunspots ($\approx 10^{-3}$ SH; Baumann & Solanki 2005). From this, we deduce a turbulent diffusivity for XX Tri of $\approx 6 \times 10^{14}$ cm^2/s, a value between 10 to 10,000 times larger than current model values for the solar convection zone (from the surface layers to the bottom of the convection zone). Because the (squared) absolute depth of the convection zone of XX Tri is about 1,200 times larger than that of the Sun (200 Mm), the diffusion timescale becomes comparable to that of the Sun. We obtain an average diffusion time of ≈ 26 yrs for XX Tri compared to ≈ 13 yrs for the Sun (the latter for an assumed diffusivity of 10^{12} cm^2/s).

So far, stellar activity cycles were inferred from long-term chromospheric Ca II H&K or photospheric V-band variations (e.g. Baliunas et al. 1995; Oláh et al. 2007) or from repeated detections of a "flip-flop" phenomenon (see Hackman et al. 2013; Korhonen & Järvinen 2007). Derived timescales for RS CVn stars range between 2-50 yrs. Just recently, Oláh et al. (2014) investigated 28 years of photometry of XX Tri along with two other over-active K giants and found a long-term sinusoidal brightness trend with a length comparable to the length of the dataset, i.e. ≈ 28 yrs. Our diffusivity-based cycle prediction of ≈ 26 yrs matches this observation surprisingly well despite the comparable shortness of the photometric coverage. XX Tri reached its maximum brightness in 2009 and is in a declining state since then. Removing this overall trend, Oláh et al. (2014) found a second shorter-period variation of order 6 yrs or an integer multiple of it. No readily explanation for this period, if real, could be given.

As already mentioned in Chapter 3.7, the reconstructed giant spots may be monolithic, but could also be a conglomerate of smaller, unresolved spots. This "classical" uncertainty could in principle impact on the interpretation of the observed decay rate, and thus the cycle length. Assuming that each unresolved spot only decays (and never grows), and does not interact with an other spot fragment, then we should observe on average the same decay rate as if the spot were monolithic. If decay and growth of individual fragments coexist, then our determined decay rate would be just a lower boundary. It then enables a maximum decay rate of ≈ -0.03 SH/day, resulting in a cycle length of ≈ 19 yrs. This cycle period would be close to our determined 1-σ uncertainty. On the contrary, no such cycle period was detected from broadband photometry. In addition, a possible cycle length of six years (from photometry) or two years (from flip-flop) would suggest a decay rate of -0.10 and -0.29 SH/day, respectively; neither of which is supported by our analysis. We conclude that our predicted cycle of ≈ 26 yrs, including an uncertainty of 6 yrs, appears to be the most credible.

Spot evolution timescales and rotational modulation

The resolved spottedness of each stellar surface element has a time gap of around 24 days, due to the stellar rotation period. Thus, we simply can not resolve spot evolution with shorter timescales. In order to infer parameters for spot evolution and therefore activity timescales we have to assume that spot evolution happen in timescales of a rotation period. But, is this assumption realistic and are there some kind of indices for confirmation?

As we know from detailed observations on the surface of the Sun, we have to differentiate between small- and large-scale structures. Solar granules with a typ-

ical diameter of around 1500 km (e.g., Hirzberger et al. 1997; Berrilli et al. 2002) usually lasts around 10 minutes before dissipating. The generation of a filamentary penumbra of a sunspot and the change of the magnetic field topology take place in less than 20-30 minutes (e.g., Leka & Skumanich 1998; Yang et al. 2003). On the other hand, leader sunspots have lifetimes of up to four months (Bumba 1963) and solar cycle estimations deduced from their related decay rate matches quite good with the observed one (Krause & Rüdiger 1975).

We investigated the rotational spot-modulation on XX Tri with three different approaches: photometric lightcurves, temperature variations from spectrum fitting, and temperature-flux modulation from our Doppler images. For each observational season, all of them show a relative stable configuration during several rotation periods. Assuming much shorter timescales we should observe discrepancies between the first two methods and the third one, as the photometric and spectroscopic observations are not correlated in time, whereas each Doppler image represents a "frozen image". Furthermore, we note that the timestamps of our photometric and spectroscopic observations are not concurrent. Thus, we suggest that the large cool spots on the surface of XX Tri evolve on timescales on the order of rotation periods, and therefore our inferred parameters for spot evolution and activity timescales are realistic.

Active longitudes and differential rotation

Active longitudes are a common feature in rapidly-rotating active stars and there is even some evidence for long-term active longitudes and a 7-year flip-flop period on the Sun (Berdyugina & Usoskin 2003). Our Doppler imagery provides evidence for a $\approx$ 2-year flip-flop period on XX Tri with a preferred longitude typically facing the (unseen) companion star. This is significantly shorter than the 6-year period from photometric data but could be the true flip-flop cycle length and thus would identify the 6-year period just as an alias. From a theoretical perspective, flip-flops possibly represent the non-axisymmetric component of a mixed-mode dynamo for weakly differentially rotating stars (Elstner & Korhonen 2005; Moss 2004). These authors explained flip-flops as an excited non-axisymmetric dynamo mode, giving rise to two permanent active longitudes in opposite stellar hemispheres, but still need in parallel an oscillating axisymmetric magnetic field. The stability of such a mixed mode is still a matter of discussion.

For XX Tri, our Doppler images indicate a weak solar-like differential rotation of $\alpha = 0.016 \pm 0.003$, which seems to be a typical value for such kind of rapidly rotating stars. Despite that large-scale mean-field dynamo models predict only a poor tracing quality for its large spots (Korhonen & Elstner 2011; but see also Czesla et al. 2013), numerous differential-rotation laws were deduced from cross correlations of cool features from consecutive Doppler images (at this point we refer to the many references cited in Korhonen & Elstner 2011). Recently, weak solar-like differential rotation was confirmed, e.g. on the K giants IL Hya (Kővári et al. 2014; Weber & Strassmeier 1998) or ζ And (Kővári et al. 2012, 2007a) while weak anti-solar differential rotation was confirmed on the K-giant σ Gem (Kővári et al. 2015, 2007b). Furthermore, weak anti-solar differential rotation was claimed for the K giants UZ Lib (Oláh et al. 2003), HD 31993 (Strassmeier et al. 2003) and HU Vir (Strassmeier 1994). All the latter are still in need of further independent

verification. For a previous summary on this topic we refer to Weber et al. (2005). We note that XX Tri fits into the differentially rotating giants with approximately ten times weaker surface latitudinal shear when compared to the Sun.

Outlook

The spectroscopic observations of XX Tri using the STELLA telescopes are still ongoing. So far, three more observational seasons are waiting for mapping and spot evolution analysis. This will increase our time-series by 50 % and certainly improve the significance of our results. In addition, continuously photometric observations of XX Tri will be able to clarify the cyclic behavior of the magnitude-range brightness variation. Last but not least, XX Tri was observed with the SOFIN spectrograph at the NOT telescope. A total of around 150 spectro-polarimetric observations were obtained during various observing runs in 2004 and 2011-2013. This dataset enables us to investigate magnetic signatures of XX Tri and further to reconstruct the magnetic field topology on the stellar surface using our ZDI-code.

In order to determine a stellar activity cycle, we presented a new method based on starspot decay analysis. The key advantage of this method is, that it enables us to investigate activity cycle lengths with (possibly) much shorter observational timespans. Within this thesis we estimate a stellar cycle length of around 26 years analyzing around 6 years of observations. Thus, we have to analyze more targets in terms of spot decay rates. On the one hand, we should apply this method on active stars with precisely known cycle length, which would verify our presented method. On the other hand, especially for stars with cycle lengths of decades, this method would accelerate their determination of activity cycles.

Bibliography

Allende Prieto, C. 2004, Astronomische Nachrichten, 325, 604 20

Appenzeller, I. & Dearborn, D. S. P. 1984, ApJ, 278, 689 10

Babcock, H. W. 1961, ApJ, 133, 572 1

Baliunas, S. L., Donahue, R. A., Soon, W. H., et al. 1995, ApJ, 438, 269 3, 10, 92

Barnes, J. R. 2005, MNRAS, 364, 137 6

Barnes, J. R., Collier Cameron, A., Donati, J.-F., et al. 2005, MNRAS, 357, L1 86

Barnes, J. R., Lister, T. A., Hilditch, R. W., & Collier Cameron, A. 2004, MNRAS, 348, 1321 11

Bastian, T. J. 1996, in Astronomical Society of the Pacific Conference Series, Vol. 93, Radio Emission from the Stars and the Sun, ed. A. R. Taylor & J. M. Paredes, 447 3

Baumann, I. & Solanki, S. K. 2005, A&A, 443, 1061 92

Berdyugina, S. V. 2005, Living Reviews in Solar Physics, 2, 8 3, 6, 10, 11

Berdyugina, S. V. 2007, Highlights of Astronomy, 14, 275 84

Berdyugina, S. V., Berdyugin, A. V., Ilyin, I., & Tuominen, I. 1998, A&A, 340, 437 53

Berdyugina, S. V., Berdyugin, A. V., Ilyin, I., & Tuominen, I. 1999, A&A, 350, 626 53

Berdyugina, S. V., Berdyugin, A. V., Ilyin, I., & Tuominen, I. 2000, A&A, 360, 272 53

Berdyugina, S. V. & Tuominen, I. 1998, A&A, 336, L25 3, 84

Berdyugina, S. V. & Usoskin, I. G. 2003, A&A, 405, 1121 3, 93

Berrilli, F., Consolini, G., Pietropaolo, E., et al. 2002, A&A, 381, 253 93

Bertelli, G., Girardi, L., Marigo, P., & Nasi, E. 2008, A&A, 484, 815 22, 24

Bidelman, W. P. 1985, International Amateur-Professional Photoelectric Photometry Communications, 21, 53 15

Biermann, L. 1938, Astronomische Nachrichten, 264, 361 3

Biermann, L. 1948, ZAp, 25, 135 3

Bopp, B. W., Fekel, F. C., Aufdenberg, J. P., Dempsey, R., & Dadonas, V. 1993, AJ, 106, 2502 16

Bopp, B. W. & Rucinski, S. M. 1981, in IAU Symposium, Vol. 93, Fundamental Problems in the Theory of Stellar Evolution, ed. D. Sugimoto, D. Q. Lamb, & D. N. Schramm, 177 11

Bopp, B. W. & Stencel, R. E. 1981, ApJ, 247, L131 11

Brajša, R., Wöhl, H., Vršnak, B., et al. 2002, Sol. Phys., 206, 229 2, 86

Brandenburg, A., Rädler, K.-H., & Kemel, K. 2012, A&A, 539, A35 8

Brown, S. F., Donati, J.-F., Rees, D. E., & Semel, M. 1991, A&A, 250, 463 1

Bumba, V. 1963, Bulletin of the Astronomical Institutes of Czechoslovakia, 14, 91 5, 91, 93

Carroll, T. A., Kopf, M., Ilyin, I., & Strassmeier, K. G. 2007, Astronomische Nachrichten, 328, 1043 44

Carroll, T. A., Kopf, M., & Strassmeier, K. G. 2008, A&A, 488, 781 44

Carroll, T. A., Kopf, M., Strassmeier, K. G., Ilyin, I., & Tuominen, I. 2009, in IAU Symposium, ed. K. G. Strassmeier, A. G. Kosovichev, & J. E. Beckman, Vol. 259, 437 44

Carroll, T. A., Strassmeier, K. G., Rice, J. B., & Künstler, A. 2012, A&A, 548, A95 39, 44

Castelli, F. & Kurucz, R. L. 2004, ArXiv:astro-ph/0405087 44

Charbonneau, P. 2010, Living Reviews in Solar Physics, 7, 3 4, 8

Czesla, S., Arlt, R., Bonanno, A., Strassmeier, K. G., & Huber, K. F. 2013, Astronomische Nachrichten, 334, 89 93

Deutsch, A. J. 1958, in IAU Symposium, Vol. 6, Electromagnetic Phenomena in Cosmical Physics, ed. B. Lehnert, 209 1, 12, 39

Dikpati, M. & Charbonneau, P. 1999, ApJ, 518, 508 88

Donati, J.-F. & Collier Cameron, A. 1997, MNRAS, 291, 1 86

Donati, J.-F., Semel, M., Carter, B. D., Rees, D. E., & Collier Cameron, A. 1997, MNRAS, 291, 658 1

Dorren, J. D. & Guinan, E. F. 1982, AJ, 87, 1546 10

Drake, J. J., Peres, G., Orlando, S., Laming, J. M., & Maggio, A. 2000, ApJ, 545, 1074 3

Dupree, A. K. 2003, in The Future of Cool-Star Astrophysics: 12th Cambridge Workshop on Cool Stars, Stellar Systems, and the Sun, ed. A. Brown, G. M. Harper, & T. R. Ayres, Vol. 12, 1–13 2

Eaton, J. A. & Hall, D. S. 1979, ApJ, 227, 907 10

Eberhard, G. & Schwarzschild, K. 1913, ApJ, 38, 292 3

Egger, H. & Neubauer, A. 2005, Numerische Mathematik, 101, 643 44

Eker, Z. 1995, ApJ, 445, 526 16, 52

Elstner, D. & Korhonen, H. 2005, Astronomische Nachrichten, 326, 278 93

Engl, H. W., Hanke, M., & Neubauer, A. 1996, Regularization of inverse problems, Vol. 375 (Springer) 44, 45

Engl, H. W. & Kügler, P. 2005, in Multidisciplinary methods for analysis optimization and control of complex systems (Springer), 3–47 44

ESA. 1997, VizieR Online Data Catalog, 1239, 0 17

Flower, P. J. 1996, ApJ, 469, 355 20

Frieden, B. R. 1972, JOSA, 62, 511 42

Fröhlich, H.-E., Küker, M., Hatzes, A. P., & Strassmeier, K. G. 2009, A&A, 506, 263 7

Gershberg, R. E. 1982, Astronomische Nachrichten, 303, 251 10

Gilliland, R. L. & Dupree, A. K. 1996, ApJ, 463, L29 1

Gokhale, M. H. & Zwaan, C. 1972, Sol. Phys., 26, 52 5

Goncharskii, A. V., Stepanov, V. V., Kokhlova, V. L., & Yagola, A. G. 1977, Soviet Astronomy Letters, 3, 147 1, 12, 39

Granzer, T., Schüssler, M., Caligari, P., & Strassmeier, K. G. 2000, A&A, 355, 1087 6

Granzer, T., Weber, M., & Strassmeier, K. G. 2010, Advances in Astronomy, 2010 19

Güdel, M. 1996, in Astronomical Society of the Pacific Conference Series, Vol. 93, Radio Emission from the Stars and the Sun, ed. A. R. Taylor & J. M. Paredes, 285 3

Guenther, E. W. & Ball, M. 1999, A&A, 347, 508 3, 10

Gustafsson, B., Edvardsson, B., Eriksson, K., et al. 2008, A&A, 486, 951 21

Hackman, T., Mantere, M. J., Lindborg, M., et al. 2012, A&A, 538, A126 52, 53

Hackman, T., Pelt, J., Mantere, M. J., et al. 2013, A&A, 553, A40 92

Hadamard, J. 1902, Princeton university bulletin, 13, 28 42

Hale, G. E. 1908, ApJ, 28, 315 1

Hall, D. S. 1972, PASP, 84, 323 3

Hall, D. S. 1976, in Astrophysics and Space Science Library, Vol. 60, IAU Colloq. 29: Multiple Periodic Variable Stars, ed. W. S. Fitch, 287 11

Hampton, M., Henry, G. W., Eaton, J. A., Nolthenius, R. A., & Hall, D. S. 1996, PASP, 108, 68 16, 52

Hanke, M. 1997, Inverse problems, 13, 79 44

Hanke, M., Neubauer, A., & Scherzer, O. 1995, Numerische Mathematik, 72, 21 45

Hartmann, L. 1990, in Astronomical Society of the Pacific Conference Series, Vol. 9, Cool Stars, Stellar Systems, and the Sun, ed. G. Wallerstein, 289–300 10

Hartmann, L. W. & Kenyon, S. J. 1990, ApJ, 349, 190 10

Hendry, P. D. & Mochnacki, S. W. 2000, ApJ, 531, 467 11

Hirzberger, J., Vázquez, M., Bonet, J. A., Hanslmeier, A., & Sobotka, M. 1997, ApJ, 480, 406 93

Holzwarth, V. & Schüssler, M. 2002, Astronomische Nachrichten, 323, 399 2, 84

Hooten, J. T. & Hall, D. S. 1990, ApJS, 74, 225 16

Hussain, G. A. J. 2002, Astronomische Nachrichten, 323, 349 7

Jabbari, S., Brandenburg, A., Kleeorin, N., Mitra, D., & Rogachevskii, I. 2015, ApJ, 805, 166 2

Jetsu, L., Pelt, J., Tuominen, I., & Nations, H. 1991, in Lecture Notes in Physics, Berlin Springer Verlag, Vol. 380, IAU Colloq. 130: The Sun and Cool Stars. Activity, Magnetism, Dynamos, ed. I. Tuominen, D. Moss, & G. Rüdiger, 381 3, 84

Jovanovic, M., Weber, M., & Allende Prieto, C. 2013, Publications de l'Observatoire Astronomique de Beograd, 92, 169 20

Joy, A. H. 1945, ApJ, 102, 168 10

Kaltenbacher, B., Neubauer, A., & Scherzer, O. 2008, Iterative regularization methods for nonlinear ill-posed problems, Vol. 6 (Walter de Gruyter) 44, 45

Käpylä, P. J., Mantere, M. J., & Brandenburg, A. 2012, ApJ, 755, L22 2

Käpylä, P. J., Mantere, M. J., & Hackman, T. 2011, ApJ, 742, 34 2

Khokhlova, V. L. 1976, Astronomische Nachrichten, 297, 217 39

Khokhlova, V. L. & Riabchikova, T. A. 1975, Ap&SS, 34, 403 1

Kővári, Z., Bartus, J., Strassmeier, K. G., et al. 2007a, A&A, 463, 1071 93

Kővári, Z., Bartus, J., Strassmeier, K. G., et al. 2007b, A&A, 474, 165 86, 93

Kővári, Z., Korhonen, H., Kriskovics, L., et al. 2012, A&A, 539, A50 93

Kővári, Z., Kriskovics, L., Künstler, A., et al. 2015, A&A, 573, A98 2, 93

Kővári, Z., Kriskovics, L., Oláh, K., et al. 2014, in IAU Symposium, ed. P. Petit, M. Jardine, & H. C. Spruit, Vol. 302, 379 93

Kloppenborg, B., Stencel, R., Monnier, J. D., et al. 2010, Nature, 464, 870 1

Kopf, M. 2008, Phd thesis, Leibniz-Institut für Astrophysik Potsdam 10, 11, 39

Korhonen, H., Berdyugina, S. V., Hackman, T., et al. 2007, A&A, 476, 881 53

Korhonen, H. & Elstner, D. 2011, A&A, 532, A106 93

Korhonen, H. & Järvinen, S. P. 2007, in IAU Symposium, ed. W. I. Hartkopf, P. Harmanec, & E. F. Guinan, Vol. 240, 453 84, 92

Krause, F. & Rädler, K.-H. 1980, Mean-field magnetohydrodynamics and dynamo theory 8

Krause, F. & Rüdiger, G. 1975, Sol. Phys., 42, 107 5, 6, 88, 93

Kron, G. E. 1950, Leaflet of the Astronomical Society of the Pacific, 6, 52 3, 12

Künstler, A. 2008, Diploma thesis, Landessternwarte Heidelberg 22

Künstler, A., Carroll, T. A., & Strassmeier, K. G. 2015, A&A, 578, A101 13

Kupka, F., Piskunov, N., Ryabchikova, T. A., Stempels, H. C., & Weiss, W. W. 1999, A&AS, 138, 119 44

Leka, K. D. & Skumanich, A. 1998, ApJ, 507, 454 93

Lindborg, M., Korpi, M. J., Hackman, T., et al. 2011, A&A, 526, A44 53

Maceroni, C., Vilhu, O., van't Veer, F., & van Hamme, W. 1994, A&A, 288, 529 11

Marsden, S. C., Berdyugina, S. V., Donati, J.-F., Eaton, J. A., & Williamson, M. H. 2007, Astronomische Nachrichten, 328, 1047 53

Martínez Pillet, V. 2002, Astronomische Nachrichten, 323, 342 5, 79

Martinez Pillet, V., Moreno-Insertis, F., & Vazquez, M. 1993, A&A, 274, 521 5

Meyer, F., Schmidt, H. U., Wilson, P. R., & Weiss, N. O. 1974, MNRAS, 169, 35 5, 88

Moffatt, H. K. 1978, Magnetic field generation in electrically conducting fluids 8

Monin, A. S. & I'Aglom, A. M. 1971, Statistical fluid mechanics: Mechanics of turbulence 8

Moss, D. 2004, MNRAS, 352, L17 93

Narayan, R. & Nityananda, R. 1986, ARA&A, 24, 127 43

Nolthenius, R. 1991, Information Bulletin on Variable Stars, 3589, 1 16

Noyes, R. W., Hartmann, L. W., Baliunas, S. L., Duncan, D. K., & Vaughan, A. H. 1984, ApJ, 279, 763 10

Oláh, K., Jurcsik, J., & Strassmeier, K. G. 2003, A&A, 410, 685 93

Oláh, K., Moór, A., Kővári, Z., et al. 2014, A&A, 572, A94 17, 18, 19, 20, 21, 22, 91, 92

Oláh, K., Strassmeier, K. G., Granzer, T., Soon, W., & Baliunas, S. L. 2007, Astronomische Nachrichten, 328, 1072 92

Oláh, K., Strassmeier, K. G., & Weber, M. 2002, A&A, 389, 202 84, 86

O'Neal, D., Neff, J. E., Saar, S. H., & Cuntz, M. 2004, AJ, 128, 1802 18

Parker, E. N. 1955, ApJ, 122, 293 1

Parker, E. N. 1979, Cosmical magnetic fields: Their origin and their activity 8

Petrovay, K. & van Driel-Gesztelyi, L. 1997, Sol. Phys., 176, 249 5

Pipin, V. V. 2013, in IAU Symposium, Vol. 294, IAU Symposium, ed. A. G. Kosovichev, E. de Gouveia Dal Pino, & Y. Yan, 375–386 8

Piskunov, N. E. & Rice, J. B. 1993, PASP, 105, 1415 1, 12

Piskunov, N. E., Tuominen, I., & Vilhu, O. 1990, A&A, 230, 363 43

Press, W. H., Teukolsky, S. A., Vetterling, W. T., & Flannery, B. P. 1992, Numerical recipes in FORTRAN. The art of scientific computing 42, 44

Prugniel, P. & Soubiran, C. 2001, A&A, 369, 1048 21

Rädler, K. H. 1969, Monats. Dt. Akad. Wiss., Berlin, Volume 11, p. 194-201, 11, 194 8

Reffert, S., Bergmann, C., Quirrenbach, A., Trifonov, T., & Künstler, A. 2015, A&A, 574, A116 22

Ribárik, G., Oláh, K., & Strassmeier, K. G. 2003, Astronomische Nachrichten, 324, 202 52

Rice, J. B. & Strassmeier, K. G. 2000, A&AS, 147, 151 12, 48

Rice, J. B., Wehlau, W. H., & Khokhlova, V. L. 1989, A&A, 208, 179 12

Roettenbacher, R. M., Monnier, J. D., Harmon, R. O., Barclay, T., & Still, M. 2013, ApJ, 767, 60 52

Rüdiger, G. & Kitchatinov, L. L. 2000, Astronomische Nachrichten, 321, 75 5, 6, 88

Rutten, R. J. 2003, Radiative Transfer in Stellar Atmospheres 43

Scargle, J. D. 1982, ApJ, 263, 835 25

Scharlemann, E. T. 1981, ApJ, 246, 292 2

Scharlemann, E. T. 1982, ApJ, 253, 298 2

Schmitt, J. H. M. M. 1994, ApJS, 90, 735 3

Schrijver, C. J. & Title, A. M. 2001, ApJ, 551, 1099 6

Schrijver, C. J. & Zwaan, C. 1991, A&A, 251, 183 2

Schüssler, M. 2002, Astronomische Nachrichten, 323, 377 6

Schwabe, M. 1844, Astronomische Nachrichten, 21, 233 1

Selam, S. O. 2004, A&A, 416, 1097 11

Semel, M. 1989, A&A, 225, 456 1, 12

Skumanich, A. 1972, ApJ, 171, 565 10

Spada, F., Demarque, P., Kim, Y.-C., & Sills, A. 2013, ApJ, 776, 87 89

Starck, J.-L., Murtagh, F. D., & Bijaoui, A. 1998, Image Processing and Data Analysis (Cambridge University Press) 46

Starck, J.-L., Siebenmorgen, R., & Gredel, R. 1997, ApJ, 482, 1011 46

Strassmeier, K. G. 1990, ApJ, 348, 682 12

Strassmeier, K. G. 1994, A&A, 281, 395 93

Strassmeier, K. G. 1996, in IAU Symposium, Vol. 176, Stellar Surface Structure, ed. K. G. Strassmeier & J. L. Linsky, 289 6

Strassmeier, K. G. 1999, A&A, 347, 225 6, 15, 16, 17, 20, 22, 23, 52, 53, 91

Strassmeier, K. G. 2004, in IAU Symposium, Vol. 219, Stars as Suns : Activity, Evolution and Planets, ed. A. K. Dupree & A. O. Benz, 11 2

Strassmeier, K. G. 2009, A&A Rev., 17, 251 6, 7, 12

Strassmeier, K. G. & Bartus, J. 2000, A&A, 354, 537 53

Strassmeier, K. G., Bartus, J., Cutispoto, G., & Rodono, M. 1997a, A&AS, 125, 11 16, 18, 19

Strassmeier, K. G., Boyd, L. J., Epand, D. H., & Granzer, T. 1997b, PASP, 109, 697 15, 17, 19

Strassmeier, K. G., Fekel, F. C., Bopp, B. W., Dempsey, R. C., & Henry, G. W. 1990, ApJS, 72, 191 3, 16

Strassmeier, K. G., Granzer, T., Kopf, M., et al. 2010a, A&A, 520, A52 21

Strassmeier, K. G., Granzer, T., Weber, M., et al. 2004, Astronomische Nachrichten, 325, 527 19

Strassmeier, K. G., Granzer, T., Weber, M., et al. 2010b, Advances in Astronomy, 2010 15, 19

Strassmeier, K. G., Hall, D. S., Fekel, F. C., & Scheck, M. 1993, A&AS, 100, 173 11

Strassmeier, K. G., Kratzwald, L., & Weber, M. 2003, A&A, 408, 1103 93

Strassmeier, K. G. & Olah, K. 1992, A&A, 259, 595 16, 52

Strassmeier, K. G., Weber, M., Granzer, T., & Järvinen, S. 2012, Astronomische Nachrichten, 333, 663 21

Tikhonov, A. 1963, in Soviet Math. Dokl., Vol. 5, 1035 42

van Leeuwen, F., ed. 2007, Astrophysics and Space Science Library, Vol. 350, Hipparcos, the New Reduction of the Raw Data 20, 22, 91

Vogt, S. S., Hatzes, A. P., Misch, A. A., & Kürster, M. 1999, ApJS, 121, 547 12

Vogt, S. S. & Penrod, G. D. 1983, PASP, 95, 565 1, 12

Weber, M., Granzer, T., & Strassmeier, K. G. 2012, in Society of Photo-Optical Instrumentation Engineers (SPIE) Conference Series, Vol. 8451 19

Weber, M., Granzer, T., Strassmeier, K. G., & Woche, M. 2008, in Society of Photo-Optical Instrumentation Engineers (SPIE) Conference Series, Vol. 7019 20

Weber, M. & Strassmeier, K. G. 1998, A&A, 330, 1029 93

Weber, M., Strassmeier, K. G., & Washuettl, A. 2005, Astronomische Nachrichten, 326, 287 94

Wilson, O. C. 1978, ApJ, 226, 379 10

Wöhl, H. 2002, Astronomische Nachrichten, 323, 329 2, 86

Wöhl, H., Brajša, R., Hanslmeier, A., & Gissot, S. F. 2010, A&A, 520, A29 86

Wolter, U., Schmitt, J. H. M. M., & van Wyk, F. 2005, A&A, 435, 261 6

Xuefu, L., He, H., & Wenbai, Z. 1996, Ap&SS, 246, 39 3

Yadav, R. K., Gastine, T., Christensen, U. R., & Reiners, A. 2015, A&A, 573, A68 2, 6

Yang, G., Xu, Y., Wang, H., & Denker, C. 2003, ApJ, 597, 1190 93

Acknowledgements

First of all, I want to thank Klaus Strassmeier for giving me the opportunity to work in his research group on stellar activity. He gave me enough freedom and encouraged me to develop my own thoughts. I am grateful for all the helpful discussions and generous advices, but also the financial support and the possibility to attend on schools, workshops, and conferences.

I am also grateful for the support, advice and helpful discussions of all our group members with special thanks to Thorsten Carroll for all the discussions about Doppler imaging and his technical support, Michael Weber and his support with STELLA spectra, and Thomas Granzer and his support with APT photometry.

I am deeply grateful to my colleague and friend Matthias Mallonn. Our time together of being PhD students with all joys and sorrows was some kind of a big adventure. I am looking forward to recall this time in several years having a barbecue together.

I also want to thank all my colleagues outside AIP, who worked with me on several interesting projects. Special thanks goes to Lisa Lehmann, who further becomes a good friend, but also to Zsolt Kővári and the Hungarian group.

Finally, my deepest thanks goes to my family for all their support over so many years. And last but not least, I am immensely grateful to my girlfriend, who always supported me in various ways.